TECHNISCHE UNIVERSITÄT WIEN

AUSTRIAN INSTITUT OF TECHNOLOGY
TOMORROW TODAY

DISSERTATION

Light Management in Organic Photovoltaic Solar Cells

eingereicht von

Imran Khan

Matrikelnumber:1328709

Ausgeführt unter der Anleitung von
Prof. Dr. Gottfried Strasser
Fakultät für Elektrotechnik und Informationstechnik
Technische Universität Wien

Dr. Jakub Dostálek
BioSensor Technologies
AIT Austrian Institute of Technology

Dr. Theodoros Dimopoulos
Center of Energy, Photovoltaic System
AIT Austrian Institute of Technology

Diese Dissertation haben begutachtet:

---------- ----------

WIEN, AM 20. NOVEMBER 2017

Dedication

to my parents and my host father Thomas Warnken

Declaration

I hereby declare that except where specific reference is made to the work of others, the contents of this dissertation are original and have not been submitted in whole or in part for consideration for any other degree or qualification in this, or any other University. This dissertation is the result of my own work and includes nothing which is the outcome of work done in collaboration, except where specifically indicated in the text.

Imran Khan

2017

Acknowledgements

The successful completion of this dissertation was made possible through the invaluable contribution of a number of people. I especially want to thank and to express my deepest gratitude to my supervisors, Dr. Jakub Dostalek from AIT-Austrian Institute of Technology, Biosensor Technologies and Dr. Theodoros Dimopoulos from AIT- Austrian Institute of Technology, Centre for Energy, Photovoltaic Systems for providing me with the opportunity to conduct this research work, for the generous guidance and continuous encouragement over the years.

I am tremendously grateful to my university supervisor Prof. Dr. Gottfried Strasser from Faculty of Electrical Engineering and Information Technology, Vienna University of Technology (TU-Wien). Thank you dear professor for accepting me as PhD student in your group and for all the support you gave me.

I acknowledge the financial support from the Austrian Science Fund (FWF) through the project TRP 304-N20 PLASMOSOL. Thank you FWF, I am very much grateful.

Special thanks go to Manuela Glogowatz from Office Management BioSensor Technologies at AIT and to Dietlinde Egger from Faculty of Electrical Engineering and Information Technology at TU-Wien. Thank you Manuela and Dietlinde for all the help, without your support and guidance the official administrative paper work wouldn't have been possible.

I would like to acknowledge our research collaborators Prof. Dr. Emil J. W. List-Kratochvil from Humboldt-Universität zu Berlin, Prof. Dr. Yi Wang from Wenzhou Institute of Biomaterials and Engineering, Florian Kolb from Joanneum Research Forschungsgesellschaft mbH.

I would like to thank all of my colleagues from Biosensor Technologies Group. Thank you Stefan, Ciril, Bea, Ola, David, Nitya, Fede♡, Chris, Vanessa♡, Priya, Agnes, Hamid, Andreas, Drago, Mario, Magdalena, Sarah, Nestor, Michaela, Isabel, Irene, Verena, Marie, and Fahim.

I would like to thank all of my colleagues from Centre for Energy and Photovoltaic System at AIT, for being supportive and helpful. Thank you Jakob Kalt, Nina Winkler, Dr. Rachmat Wibowo, Dr. Stefan Edinger and Dr. Neha Bansal.

I would like to thank all of my colleagues from AIT- Health & Environment Department, thank you Dr. Thomas Maier, Dr. Heer Rudolf, Dr. Nadezhda Kataeva, Dr. Jörg Schotter, Jeannette Ackermann and Dr. Stefan Schrittwieser.

A very special thanks goes out to my special friends Jatinder, Martin, Hulan and Mimone, you are all angels sent to me from heaven. Thanks for helping me get through the difficult times, and for all the emotional support, entertainment, love and caring you provided.

Last but not the least; a special gratitude and love goes to all the members of my family, who have supported during my whole life and have motivated and inspired me through their hard work and quest for science and knowledge.

Abstract

Sunlight is arguably the most abundant resource of renewable energy. Photovoltaic technology offers a sustainable and environmentally friendly way for the conversion of sunlight energy into electricity. Organic photovoltaic (OPV) solar cells represent next-generation photovoltaic technology that utilizes materials that can be synthesized at low cost and are compatible with mass production via large-area roll-to-roll type processing techniques on flexible substrates. To achieve high-efficiency OPV solar cells, one of the key issues is to reduce their optical losses. In particular, the incomplete absorption of light in the photoactive layer (which is inherently very thin due to the low charge-carrier mobility and small exciton diffusion length) and optical reflectance due to the abrupt change in the refractive index across the layer structure are the major contributors. This work mainly concerns the optical engineering at the OPV solar cell interface in order to circumvent these problems.

Firstly, improved light trapping in a thin photoactive layer is pursued by using a novel absorber that is based on a phenomenon called surface plasmon resonance. This strategy enables the utilization of photoactive materials with short carrier diffusion length such as those that are used in common OPV solar cells architectures. This thesis presents a novel approach to plasmonic absorber, which offers the advantage of light harvesting over broad range of wavelengths and angles of incidence. It takes advantage of a corrugated multi-diffractive metallic grating that can simultaneously serve as metallic electrode. The structure comprises multiple superimposed periodical modulations that can be prepared by facile means such as nanoimprint lithography. The developed multi-periodic grating enhances the light absorption in the investigated active layer P3HT: PCBM by a factor of 2.9 in the spectral window 600–750 nm where this material is inherently weakly absorbing. Over the whole visible/NIR part of the spectrum (400–750 nm) the number of absorbed photons in P3HT: PCBM photoactive layer is increased by 28 %.

Secondly, reduction of the optical reflectance at OPV layer interfaces is investigated by using tailored antireflection (AR) periodic nanostructures. In this work AR nanostructures were deployed at transparent indium tin oxide (ITO) electrode by a combination of laser interference lithography, soft lithography and DC magnetron sputtering process. The structure was tailored to provide broadband AR characteristics in the visible and near-infrared region by suppressing the Fresnel reflection with densely arranged nanostructures. The light transmission in the 450–850 nm range was enhanced by 8% (absolute) compared to flat ITO films, which is one of the largest performance improvements reported in the literature for nanostructured transparent electrodes.

Thirdly, alternative structures to ITO transparent electrodes with additional light harvesting features were explored based on multi-diffractive arrays of plasmonic nano-wires. Contrary to the majority of state-of-the-art approaches that employ complex fabrication methods such as focused ion beam milling or electron-beam lithography techniques, the presented work utilizes UV laser interference lithography with dry etching step that allows for facile structuring of large areas. Detailed investigation of competing light trapping and transparency is carried out and arrays of gold nanowires with comparable transparency and resistance to regular ITO films were prepared.

Finally, the prepared nanostructures were also exploited outside the OPV domain through other collaborative projects relating to biosensing. For example gold and aluminium nanostructures prepared through the course of this thesis were used in a smartphone label-free biosensor for the detection of lipopolysaccharides, for surface enhanced Raman spectroscopy studies, and for UV surface plasmon spectroscopy sensing.

Contents

List of Figures

Nomenclature

A

Antireflection……..……..AR
Atomic force microscopy……AFM

I

Indium tin oxide……..……ITO

L

Laser interference lithography……LIL
Localized surface plasmon resonance……..…LSPR

M

Moth eye nanostructures……MEN

N

Nanoimprint lithography……NIL

O

One-dimensional……..…..1-D
Organic photovoltaics……..…..OPV
Organic photovoltaics devices……..….OPVs

P

Period……Λ
Photovoltaic……..….PV
Polydimethylsiloxane……..……PDMS
Propagating surface plasmons……..……PSPs
Power conversion efficiency……..…….PCE
Poly (3-hexylthiophen-2,5-diyl) ....…….…..…P3HT
Phenyl-C61-butyric acid methyl ester……..…….PCBM

R

Refractive index……..……n

S

Scanning electron microscopy……..……SEM
Surface plasmons resonance……..……SPR

T

Two-dimension……2-D

W

Wavelength……..……..……..λ

Publications

Author's publications:

(1): I. Khan, H. Keshmiri, F. Kolb, T. Dimopoulos, E. J. List-Kratochvil, and J. Dostalek, "*Multidiffractive broadband plasmonic absorber,*" Advanced Optical Materials **4**, 435-443 (2016).

(2): I. Khan, M. Bauch, T. Dimopoulos, and J. Dostalek, "*Nanostructured as-deposited indium tin oxide thin films for broadband antireflection and light trapping,*" Nanotechnology (2017).

(3): I. Khan, M. Bauch, T. Dimopoulos, and J. Dostalek "*Transparent plasmonic electrode based on metal multi-periodic nanowires*" Manuscript in preparation.

Author's publications in collaborative work:

(1): J. Zhang, **I. Khan**, Q. Zhang, X. Liu, J. Dostalek, B. Liedberg, and Y. Wang, "*Lipopolysaccharides detection on a grating-coupled surface plasmon resonance smartphone biosensor*," Biosensors and Bioelectronics 99, 312-317 (2018).

(2): F. Geiss, S. Fossati, **I. Khan**, N. G. Quilis, W. Knoll, and J. Dostálek, "*UV-SPR biosensor for biomolecular interaction studies,*" in SPIE Optics+ Optoelectronics (International Society for Optics and Photonics, 2017), pp. 1023107-1023107-1023108.

(3): N. G. Quilis, M. Lequeux, **I. Khan**, M. Lamy, D. L. Chapelle, and J. Dostalek, "*Plasmonic nanoparticle arrays tailored by laser interference lithography for SERS*" Manuscript in preparation.

Conference contribution

(1): Nano and Photonics Mauterndorf/Salzburg, Austria, (19th –21th March 2015). Poster presentation: "*Multi-diffractive Plasmonic Absorber for Thin Film Solar Cells*".

(2): International Conference on Hybrid and Organic Photovoltaics, Swansea, United Kingdom (29th – 31^{lst} June 2016). Poster presentation: "*Plasmonic Light Trapping in Thin Film Solar Cells*".

Chapter 1 Introduction

1.1 Photovoltaics

Energy is a basic need for humanity. Photovoltaic (PV) technology represents a sustainable and environmentally friendly way for the conversion of sunlight into electricity and could provide competitively priced energy on a large scale to the world. PV technology has been growing at a rapid pace in the last decade and it has achieved considerable attention as one of the most promising renewable energy alternatives [1-3].

The conversion of solar energy into electrical energy can be utilized by using a physical phenomenon referred as the photovoltaic effect. The photovoltaic effect occurs when light strikes onto a layer (or set of layers) of specially prepared light sensitive material of the PV device or solar cell device, which produce electricity in the form of direct current (DC). The first report of a photovoltaic effect can be traced back to Becquerel's 1839 pioneering studies in liquid electrolytes [4]. In 1954 at Bell Laboratories, Chapin reported a silicon based PV device for the direct conversion of sunlight into electricity [5]. This was the tipping point that transformed photovoltaics into a technology to convert sun light into energy. The energy produced can be stored in batteries to be used outside of the daylight hours, or can be injected into the electrical grid. As a result, these terms have been coined Solar Electricity, Solar Electric Technology and Solar Photovoltaics (Solar PV). Nowadays, mostly the terms "Photovoltaics" or "PV" are used to denote "Solar Photovoltaics". Furthermore, the term "Solar" or "Solar Energy" is also used to denote "Solar Photovoltaics"; however, it is important to note here, that the concept of solar energy is much broader than photovoltaics as there are other ways of getting useable energy from the sun's radiation. For example sunlight may also be converted into electricity using conventional principles in solar-thermal power plant technology, which uses concentrated sunlight to produce heat for subsequent energy production process (turbine drive by steam to generate electricity etc.) [6, 7].

PV technologies are currently dominated by traditional silicon-based and chalcogenide-based solar cells that are available on the market these days such as; amorphous silicon and cadmium telluride and copper indium selenide [8]. The manufacturing costs of energy produced by silicon-based PV technology are higher (due to processes at high temperatures 400–1400 °C and high vacuum conditions etc.) than those for the energy supplied by conventional fossil fuels [9]. Due to this reason, the silicon-based PV technology has strongly relied on government support and many nations offer subsidies. In this regard, concepts for organic PV technology based on organic semiconductors were established by Alan J. Heeger, Alan MacDiarmid and Hideki Shirakawa [10]. These efforts take advantage of organic semiconductors to facilitate the transition of PV technology from inorganic to other materials that can be processed using low-cost and scalable techniques. The focus of this work is on the optical engineering for organic photovoltaics (OPV). In the following section a brief introduction to OPV solar cells and a detailed treatment of the light manipulation concepts is presented.

1.1.1 Organic photovoltaics

Organic photovoltaics (OPV) is pursued for next-generation PV technology, due to the cheaper manufacturing cost and the potential for mass production compatible with large-area roll-to-roll manufacturing on flexible substrates [11-13]. Furthermore, OPV technology is expected to deliver a clean and sustainable source of energy and to play a key role in meeting the global energy challenges. Therefore, OPV has been the subject of active research over the past two decades and has received increasing interest in recent years by the industrial sector [12, 14]. The main types of organic photovoltaic devices (OPVs) include molecular OPVs based on small molecules [15, 16], polymers [17] and hybrid (solar cells which combine both organic and inorganic materials) [18]. OPVs are distinguished based on the choice of the materials used in the structure of the device and by the fabrication techniques used to make thin films from these materials. In OPV technology, there are two common techniques for thin film production. One is based on thermal evaporation and the second is based on solution processing. In the thermal evaporation technique, the crucial requirement is the stability of the materials (e.g. OPV based on small molecules), while for solution processing technique the materials need to be soluble in an appropriate solvent (e.g. OPV based on semiconducting polymers) [19].

1.1.1.1 Structure of OPV solar cells

The basic and simple structure of OPV solar cell typically consists of a thin film of organic material for absorbing light sandwiched between two electrodes. One electrode needs to be transparent, so light can reach the organic thin film and become absorbed. In OPV solar cells, the thin film of the organic material is known as photoactive layer or simply active layer. The first studied OPV solar cell architecture reported in 1959 by Kallmann and Pope was a homo-junction, i.e. a single organic material layers, sandwiched between two electrodes [20]. This was the first generation of OPV solar cells, which were further investigated and improved, but the power conversion efficiency (*PCE*) remained poor and reached 0.7% [21, 22]. The next major breakthrough was achieved in 1986, when C.W. Tang introduced the bilayer heterojunction concept to the OPVs. In Tang's bilayer heterojunction solar cell concept, two different organic material layers were deposited on top of each other and sandwiched between two electrodes. The reported OPV solar cells had a *PCE* of about 1% [23]. Later a new architecture was introduced to the field of OPV solar cells that are based on organic polymer blend system known as bulk heterojunction (BHJ). The first proof-of-principle BHJ concept was successfully demonstrated by the group of Alan Heeger in 1995 [24]. During the last years the performance of bulk heterojunction solar cells has been improved significantly (e.g. reported *PCE* in 2001 was 2.5 % [25] and in 2011 further improved to over 10 % [26]).The structure of the state-of-the-art bulk heterojunction OPV solar cell is shown schematically in Figure 1.1(a). The structure of the OPVs starts with an indium tin oxide (ITO) coated glass substrate which acts as the transparent top electrode. The thickness of the ITO film is typically d_{ITO} ~150 nm. Then a photoactive layer for absorbing light is deposited on top of the ITO electrode. The photoactive layer is a mixture of light-sensitive polymers or small molecules and fullerene-like compounds. The ideal photoactive layer exhibits a low bandgap to broaden the absorption range of light and crystalline characteristics to ensure good charge mobility. For this purpose, a number of organic photoactive materials has been designed, synthesized, and applied in the field of OPV. A profound knowledge of the photoactive layer materials for OPV solar cells is given in [27]. The most widely studied photoactive layer consists of a polymer blend

system, which is based on the solution processed p-type electron donor poly (3-hexylthiophene) (P3HT) or [N-9'–heptadecanyl-2,7-carbazole-alt-5,5-(4',7'-di-2-thienyl-2',1',3′benzothiadiazole)] (PCDT -BT) and an n-type electron acceptor 1-(3-methoxycarbonyl) propyl-1-phenyl [6, 6] C61 (PCMB) [28-30]. The optimal thickness for the photoactive active layer of the OPV bulk heterojunction solar cells based on polymer and fullerene derivative, is found to be ~100 nm [31, 32]. Finally, the device is completed by depositing a back or rear electrode (usually a metal) onto the photoactive layer [11, 22, 33-35]. The thickness of the metallic electrode (usually silver or aluminium) is in the range of 100–200 nm.

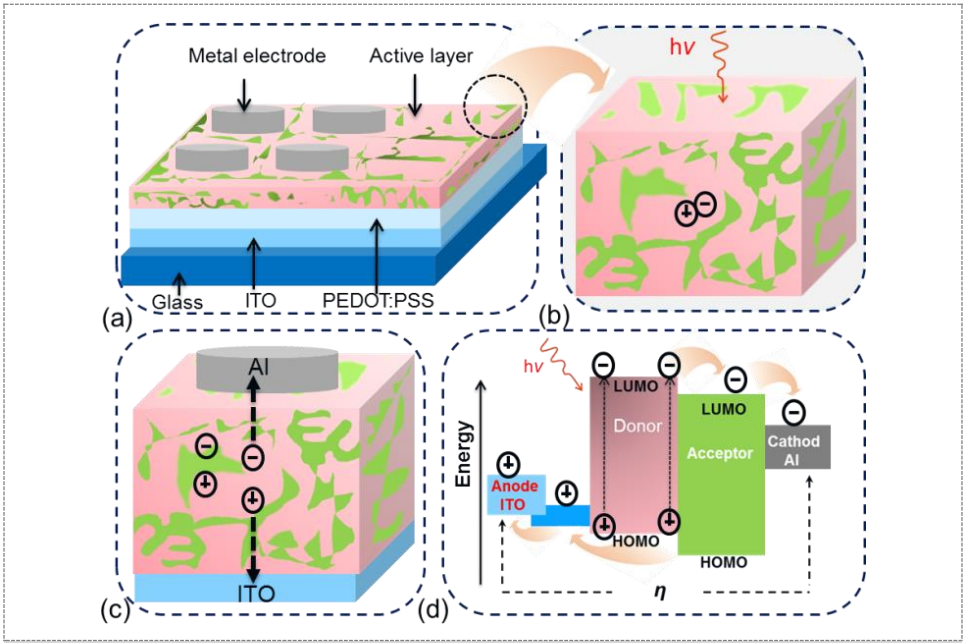

Fig. 1.1: An example of an OPV solar cell: (a) Device structure, the active layer is sandwiched between two electrodes: ITO coated with a hole transport layer PEDOT: PSS and aluminium. (b) Light absorption produces excitation. (c) Dissociation of excitation at interface. (d) Charge transport, electron and hole move to their respective electrode as explained by the energy level diagram of a donor acceptor system.

1.1.1.2 Working principal of OPV solar cells

The basic operation and physics behind a solar cell device is comprehensively described in many academic text books [36, 37] and research articles [38, 39] and thus only a brief introduction is presented here. The external behaviour of an OPV solar cell is the same as that of conventional solar cells (comprising of an inorganic semiconductor i.e. mono and multi crystalline silicon) [40], but the mechanism by which the conversion of sunlight into electricity occurs is different. The photoactive layer is not crystalline, there is no conduction and valance band system, instead it has highest occupied molecular orbital (HOMO) and lowest unoccupied molecular orbital (LUMO) system for the electrons [33]. The working principle of the OPV solar cell for energy conversion mechanism involves the following fundamental processes [34, 41].

(i) Light absorption

Light is an electromagnetic radiation which can be described as a flux of photons with specific amounts of energy. The energy E_λ of a photon is related by its wavelength λ as:

$$E_\lambda = \frac{hc}{\lambda} = hv, \tag{1.1}$$

where h is the Planck's constant, v is the frequency and c is the speed of light. Light impinging at an OPV solar cell passes through the transparent electrode ITO reaching the photoactive layer. Photon with energy E_λ greater than the bandgap is absorbed by the active layer. Unlike inorganic solar cells, the absorption of photons does not translate directly into free electron-hole pairs in a photoactive layer. Instead it generates excitons, which are electron-hole pair system bound to each other by Coulomb forces [33, 42]. The binding energy of exciton produced in organic materials is large e.g. typically on the order of or larger than 500 meV, compared with a few meV in the case of inorganic semiconductors [33]. That is why the optical absorption in active layer does not lead directly to free electron and hole carriers. The exciton is created when an electron in the donor part of photoactive layer undergoes photo-induced excitation from HOMO to LUMO, shown schematically in Figure 1.1(d). The ratio of the number of produced excitons to the incident photons is known as the absorption efficiency.

(ii) Exciton diffusion

Upon reaching an interface between donor and acceptor, the exciton must diffuse and split into free carriers within the diffusion length before recombination happens. The diffusion length value is typically 10 nm [16, 41], which implies that only those excitons formed within a distance of typically 10 nm from the interface can contribute to the electric power of the solar cell device. The ratio of the number of excitons that reach to the interface to the total number of excitons generated is known as the exciton diffusion efficiency.

(iii) Charge transport and collection

The transport of charges is affected by recombination during the journey to the electrodes. Positive charges hop via nano-sized polymer domains to one electrode, and negative charges migrate through the fullerene to the other, thereby generating electric current. In OPVs properly ordered donor and acceptor domains are needed for excellent charge transport [43]. The transport of free carriers to the respective electrode occurs within a period of time ranging from nano to microseconds. The electric current that a photovoltaic solar cell delivers corresponds to the number of created charges that are collected at the electrodes. The collected carriers define the important photovoltaic parameter known as power conversion efficiency. This depends on the fraction of photons absorbed, the fraction of electron-hole pairs that are dissociated, and finally the fraction of (separated) charges that reach the electrodes determining the overall photocurrent efficiency.

1.2 Losses in organic photovoltaic solar cells

The power conversion efficiency of an OPV solar cell is reduced by different loss mechanisms [44]. Below, each individual loss mechanism is briefly described.

(i) Exciton losses: in the photoactive layer of an OPV solar cell, the excitons must be formed and disassociated to generate a current. The exciton losses happen, when the transport of excitons is hindered from the place where the exciton is generated to the donor-acceptor interface or due to inefficient exciton dissociation at the interface [44]. Therefore, OPV

solar cells require donor-acceptor interfaces to efficiently dissociate tightly bound excitons.

(ii) Recombination losses: it is commonly deemed that in OPV devices, the transport of charges is affected by recombination during the journey to the electrodes. Only a small part of the carriers recombine radiatively and most non-radiatively at the interfaces of acceptor-donor or due to defects in the active layer [44]. One of the particular reasons for recombination losses lies in the utilization of same material (active layer) as transport medium for both, electrons and holes [45].

(iii) Collection losses: mean that due to insufficient mobilities, only parts of the free carriers reach the electrodes [44].

(iv) Transmission losses: occur when the photon energy is smaller than the bandgap energy. In this case, the photons cannot be absorbed and cannot generate a current. Majority of semiconductor polymers have bandgaps higher than 2.0 eV which limits the absorption [44].

(v) Optical losses: mean that light may be parasitically absorbed in the device layers that are not active in charge carrier collection or generation [44]. The optical losses also include reflection losses from the device interfaces and the use of thin active layers (because their low carrier mobility limits the active film thickness).

All of the above loss mechanisms have direct effect on the photovoltaic parameters of the OPV device. In order to understand this, the following section explains the key PV parameters [46].

Figure 1.2 shows the simplified equivalent circuit of an ideal solar cell device. This consists of a photocurrent source in parallel with a diode. In dark condition, the device does not generate any current and behaves like a diode. Under illuminated condition, when the intensity of the incident light increases, current is produced by the solar cell device. The current voltage equation of the simplified equivalent circuit can be derived from Kirchhoff's law. In an ideal solar cell, the total current output I is equal to the difference between current I_{ph} generated by the photoelectric effect and the diode current I_D, as can be seen in the following equation

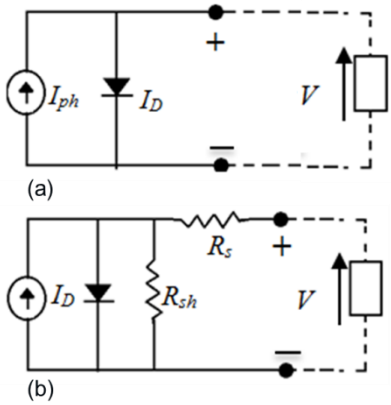

Fig. 1.2: Equivalent circuit of an (a) ideal and (b) real PV device, including series and shunt resistances.

$$I = I_{ph} - I_D = I_{ph} - I_o\left(exp^{\frac{qv}{nk_BT}} - 1\right), \tag{1.2}$$

where I_o is the diode reverse saturation current and it depends on the recombination in the solar cell device, q is the elementary charge, k_B is the Boltzmann constant, T is the absolute temperature and n is the ideality factor. The ideality factor (which contains important information on the charge carriers transport and recombination processes in OPVs) varies from 1 to 2 depending on the fabrication process of the device and the semiconductor material. The simplified circuit model explained above does not give full

representation of the electrical behaviour of a real solar cell device, because it neglects the contribution of parasitic resistances. Therefore shunt resistances can be included as a parallel shunt resistance R_{sh} and a series resistance R_s (see Figure 1.2) in a solar cell circuit. In this case the total current output I can be expressed as

$$I = I_{ph} - I_D = I_{ph} - I_o\left(exp^{\frac{q(vIR_s)}{nKT}} - 1\right) - \frac{V + IR_s}{R_{sh}}. \quad (1.3)$$

The series resistance R_s is the resistance between the different layers of the solar cell device (mainly the sum of contact resistance on the front and back surfaces), while R_{sh} represents the power dissipation caused by leakage currents due to alternative paths of the current flow. Figure 1.3 shows an example of typical current–voltage characteristics in the dark and under illuminated condition and defines key photovoltaic parameters of a photovoltaic solar cell device.

The current–voltage plots permit an evaluation of the photovoltaic performance and electric behaviour of the solar cell device [41, 47]. From the plots we define: short circuit current I_{SC}, corresponding to the short circuit condition when the voltage is zero. For an ideal PV device (R_s =0, R_{sh} →∞), this maximum current value is equal to the total current produced by photon excitation (I_{SC}= I_{ph}). Open circuit voltage V_{oc}, is the voltage at which no current flows through the external circuit. It is the maximum voltage that a solar cell can deliver. Mathematically V_{oc} is define by the following equation

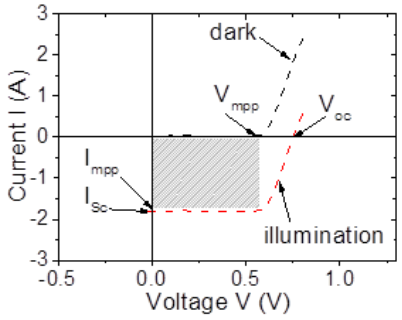

Fig. 1.3: An example of a typical I-V curve in dark and under illumination condition. The PV parameters open circuit voltage V_{oc}, short circuit current I_{SC}, current at maximum power output I_{mpp} and voltage at maximum power output V_{mpp} are defined.

$$V_{oc} = I(V = 0) = \frac{nKT}{q}\ln\left(\frac{I_{ph}}{I_o} + 1\right). \quad (1.4)$$

Equation 1.4 shows that open circuit voltage depends on the saturation current I_o of the solar cell device and the photo-generated current I_{ph}. Another PV parameter utilized to characterize the maximum power point is the fill factor FF, mathematically defined by equation (1.5). It is the ratio between the maximum power generated (I_{mpp} V_{mmp}) by the device and the product of open circuit voltage with short circuit current

$$FF = \frac{I_{mpp}\, V_{mmp}}{I_{SC} V_{oc}}. \quad (1.5)$$

Finally, the most important parameter to evaluate the electrical performance of a solar cell device is the PCE. It is defined as the ratio of the maximum electrical power output P_m, to the solar power input P_{in}

$$PCE = \frac{P_m}{P_{in}} = \frac{I_{sc}\, V_{oc}\, FF}{P_{in}}. \quad (1.6)$$

Solar power input P_{in} is the product of the irradiance of the incident light, measured in W/m^2, with the surface area of the solar cell device. The electric behaviour test of the device must be done under standard conditions that specify a temperature of 25 °C and an

irradiance of 1000 W/m^2. The light intensity standardized at 1000 W/m^2 with a spectral intensity distribution matching that of the sun on Earth's surface at an incident angle of 48.2 degree is called AM 1.5 spectrum [11, 48].

In solar cell device the parasitic resistances, also known as electrical losses, affect the power conversion efficiency of the device. Therefore, a careful design of the device to maximize R_{sh} and minimize R_s is crucial for achieving high PCE. In addition, the exciton diffusion length and the charge mobility has to be engineered in order to optimize the open circuit voltage V_{OC}.

Besides these electronic characteristics, also optical properties play a key role. In general, the short circuit current I_{SC} stated in equation (1.6) can be obtained as the following function of incident photon flux Φ:

$$I_{sc} \sim e \int \Phi(\lambda) \eta_{EQE}(\lambda)\, d\lambda, \tag{1.7}$$

where η_{EQE} is external quantum efficiency. The η_{EQE} of a solar cell device is defined as the ratio of the number of charge carriers collected at the electrodes to the number of incident photons. This parameter can be obtained as efficiency product of multiple physical effects in OPV device i.e. absorption of photons leading to exciton generation, exciton diffusion to the donor-acceptor interfaces, dissociation of exciton pairs into electron and hole, and collection of charge carriers at their respective electrodes [49]:

$$\eta_{EQE} = \eta_A \eta_{diff} \eta_{diss} \eta_C \ldots. \tag{1.8}$$

In this equation η_A states for an absorption yield, which is the probability of photon absorption inside the active layer where it can contribute to the generation of excitons. This parameter can be expressed as:

$$\eta_A = \frac{\int E^2\, Re\{n\} Im\{n\} dV_{active\ layer}}{\int E^2\, Re\{n\} Im\{n\} dV_{all\ layer}}, \tag{1.9}$$

where the integration for absorption rate is done over the volume of the stack of solar cell layers, *n* states for the complex refractive index, and E for the electric field amplitude generated by the incident light in the solar cell device. From this equation it is clearly apparent that strategies for light harvesting inside the active layer that leads to enhancement of electric field amplitude *E*, can improve the power conversion efficiency of a solar cell device.

1.2.1 Optical losses in organic photovoltaic devices

Many studies have been conducted to enhance the power conversion efficiency of OPV solar cells that is limited by the incomplete absorption of light energy in the photoactive layer. The power conversion efficiency of polymer solar cells has been increased through improvements in the control over active layer blend (donor-acceptor polymers) phase separation, through advances in the electronic properties of the active layer [50] and through advances in the bandgap engineering (broader absorption spectrum for increasing open circuit voltage) [51, 52]. Despite of these and many other types of efforts made in the field of OPV technology, the PCE of OPV solar cells is limited by the ability of the active layer to completely absorb the incident light. The active layer is inherently very thin due to the low charge-carrier mobility and small exciton diffusion length of most

small molecular and polymeric materials [53, 54]. Therefore, the optimized thickness of the photoactive layer is always a result of the trade-off between light absorption and charge carrier extraction. As mentioned earlier the optimal thickness for the active layer of OPV solar cells based on polymer and fullerene derivatives is about d_a~100 nm, the optical losses (optical interference and recombination losses) are already taken into account. Despite the fact that the absorption coefficient of organic materials is generally high (usually $\geq 10^5$ cm^{-1}), light with energy in the absorption band of the photoactive layer is not completely absorbed with a state-of-the-art 100 nm layer [11, 34]. Due to this reason optical manipulation of light is of paramount importance to enhance the absorption of the incident light in the photoactive layer. There are many different strategies that include proper designs of the OPV device architecture [55], geometry [56-58] and electrode materials composition and thickness [59-64]. This work focuses on the enhancement of the light absorption efficiency of photoactive layer by using plasmonic nanostructures tailored to serve for light harvesting.

In addition to the incomplete absorption of light in the active layer, another source of optical loss is the reflection of incident light from the solar cell device. Reflection of incident light is an optical phenomenon which comes from different refractive indices at the interface of two materials. As discussed in the above section 1.1, incident light traverses the glass substrate and the transparent electrode and photons are absorbed by the thin photoactive layer of the OPV device. The reflectance from the top surface [light incidence surface of the solar cell (air/substrate)] and from the interfaces (substrate/transparent electrode/active layer) of the device contributes to the optical losses. When light passes the interface between two media, the reflectance R occurs due to the sudden change in the refractive indices of the two materials. If n_1 and n_2 are refractive indices of the two media, then R for the normal incidence can be assessed by Fresnel equation [5, 65]

$$R = \left|\frac{n_2 - n_1}{n_2 + n_1}\right|^2. \tag{1.10}$$

For absorbing material, the R is given by replacing the n term in equation (1.7) by ñ, known as the complex refractive index

$$\tilde{n} = n + ik, \tag{1.11}$$

where k is the imaginary part of the complex refractive index, it is often referred as to the extinction coefficient. The equation (1.7) for two media can be written as follows

$$R = \frac{(n_2 - n_1)^2 + (k_2 + k_1)^2}{(n_2 + n_1)^2 + (k_2 + k_1)^2}. \tag{1.12}$$

The equation shows that the larger the difference between the refractive indices of the two materials, the greater the reflectance at the interface between them. In organic photovoltaic solar cells, this implies the reduction of the short circuit current due to reflectance of the incident light. In this regard the antireflection schemes become of great importance, and incident photon absorption can be effectively enhanced by introducing anti-reflection (AR) structures on the light incidence front surface or inside the OPV device [66-68]. The focus of this thesis will lie on minimizing the reflectance of OPV solar cells by integrating antireflective nanostructures to state-of-the-art transparent electrode (ITO).

1.3 Optical manipulation of light by nanoscale architectures

The optical manipulation of light by nanoscale architectures has gained increasing popularity for improving the performance characteristics of a variety of optoelectronic devices including light emitting diodes, thin film solar cells, flat panel displays, and photodetectors. There exists a variety of light manipulation architectures based on plasmonic and dielectric nanostructures. The following sections describe individual approaches of plasmonic and dielectric light management with regard to the specific situation in OPV solar cells. To achieve high efficiency OPV solar cells, one key issue (as learned from the above sections) is to overcome the insufficient photon absorption in organic photoactive layers since their low carrier mobility limits the film thickness for minimized charge recombination loss. One solution that addresses this problem is plasmonic nanostructure-based light harvesting [69-71]. Plasmonic nanomaterials or nanostructures are incorporated in the OPV device, which can induce surface plasmon resonance (SPR) effects at the corresponding metal-organic photoactive layer interface [70, 71]. It is possible to tune the SPR effects by proper engineering of plasmonic structures to enable a strong scattering or absorption of light [72] at desired spectral windows. Another approach for light manipulation is mainly focused on the enhancement of light absorption efficiency in the active layer by supressing the reflection of incident light from the solar cells [66]. In order to suppress the light reflection, an anti-reflection layer or a light in-coupling texture at the front surface of the device is incorporated. Such a buffer layer can reduce the reflection loss of the incident light and thus increase the light coupling into the solar cell device [66-68, 73]. The following section provides the basic theory behind the optical manipulation of light, with a focus on two approaches, plasmonic and AR nanostructures.

1.3.1 Plasmonic nanostructures

The study of optical phenomena related to the electromagnetic response of metallic nanostructure led to the development of an emerging and fast growing research field called plasmonics. It concerns confinement of light energy on such structures which finds its applications in the fields of nano-optics, bio-optics, photonics, thin film photovoltaics, and quantum information processing [74-81]. Surface plasmons are collective oscillations of conduction electrons originating from metallic surfaces. By altering the structure of a metal surface, the properties of surface plasmons, in particular their interaction with light can be tailored. Therefore incorporation of plasmonic nanostructures is a promising approach for light management in OPV solar cells.

Plasmonic light harvesting method uses metallic nanostructure geometries to increase the optical absorption without increasing the thickness of the light harvesting photoactive layer(s) of the thin film solar cells [56, 82]. These nanostructure geometries support surface plasmons and offer three mechanisms for the light management (enhancement of light absorption in device) without reducing the state-of-the-art thickness of the photoactive layer(s) of OPVs [78, 83].

(i) Light scattering by localized surface plasmons

In this approach metal nanoparticles (NPs) are used as subwavelength scattering elements to couple light into the photoactive layer of the solar cell device [84, 85]. The NPs enhance the effective optical path length of the incident light due to multiple and high angle scattering events in the device, thereby increasing the photon absorption efficiency

[72, 86]. The light scattering by plasmons is depicted schematically in Figure 1.4. The light scattering properties of metal NPs are a function of their size and for spherical NPs can be described by the Mie theory [87, 88].

The scattering efficiency can be tailored by the shape, environment, density distribution, and size of the metal NPs [72, 89]. A perfect position for NPs in the structure of an OPV device is the one, where NPs enables more light to pass through the organic active layer. A 24% enhancement in short-circuit current density and 18% in power conversion efficiency have been reported by Jung et al [90], attributed to the plasmonic scattering of NPs embedded at the interface of active layer and ITO of the OPV device. Similar approaches were made to enhance the power conversion efficiency of the OPV devices via plasmonic scattering effect by incorporating NPs into the structure of the device [91, 92].

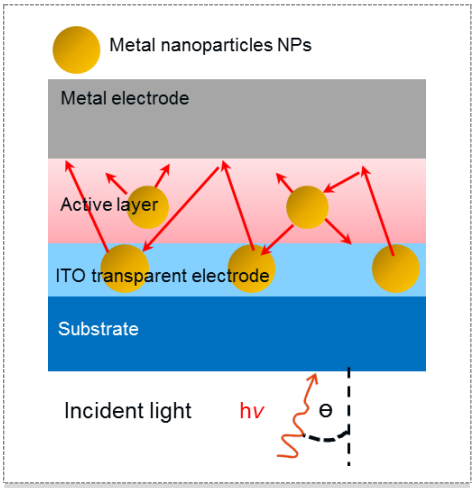

Fig. 1.4: Schematic representation of plasmonic light harvesting approach based on scattering by localized surface plasmons. The NPs work as scattering elements that increase the optical path length of incident light in the structure of an OPV device.

(ii) Light concentration by localized surface plasmons

In this approach metal NPs are used as subwavelength "antennas", in which energy of light is confined to surface plasmon near-field that overlap with the photoactive layer of the solar cells [93].

These antennas are especially useful in thin film solar cells, which use polymeric organic semiconductors as photoactive layer having diffusion length of less than 20 nm [78]. The incorporation of small NPs (5–20 nm) into the active layer of OPV devices could induce near field effect or localized surface plasmon resonance (LSPR) upon photoexcitation, which results in an enhancement of optical absorption efficiency. This principle of light manipulation is depicted schematically in Figure 1.5, where the metallic nanoparticles are embedded inside the semiconductor photoactive layer. The choice of the material, shape, size, concentration, composition, location and spacing of incorporated metal NPs are crucial parameters to tailor light concentration in thin film solar cell devices [69, 85, 95, 96]. Diukman et al [95] demonstrated that the absorption enhancement in organic photovoltaic cells can be achieved by the incorporation of Au nano-disk arrays

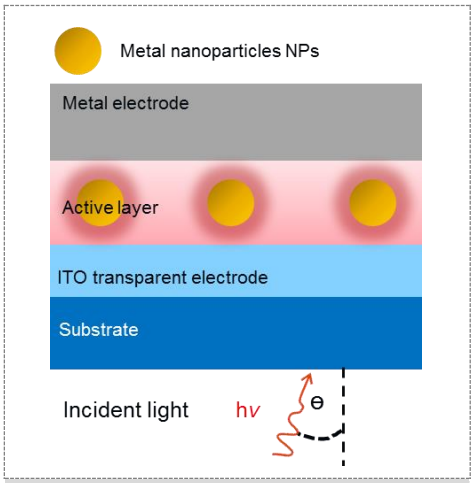

Fig. 1.5: Schematic representation of plasmonic light harvesting approach for OPV device, based on light concentration by localized surface plasmons. In this approach, the local enhancement of the electromagnetic field occurs as a result of the resonance effect, which leads to the effective light concentration near the surrounding of the metallic NPs [94].

that extend from the front transparent electrode ITO into the active layer. In another work by Liu et al [97], the power conversion efficiency of OPV device was improved from 5.75 % to 7.4 % by the incorporation of Au arrow-head nano-rods into the photoactive layer. In similarly way, LSPR exhibited by plasmonic nanomaterials of different shapes (nano-particles or nano- prisms act as nano-antennas) in the photoactive layer, improved the short-circuit photocurrent density by 17.91 % and the power conversion efficiency by 19.44 % compared to the pre-optimized OPV devices [98].

(iii) Light trapping by surface plasmon polaritons

In this approach a corrugated metallic film (as rear plasmonic electrode) on the back surface of an active layer can couple the light into surface plasmon polaritons (SPPs) modes [78]. SPPs are surface-bound electromagnetic waves which can propagate along metal-dielectric interfaces [99]. The light trapping by surface plasmon polaritons in the OPV device, is schematically depicted in Figure 1.6 and similarly to the previous section it relies on the near field enhancement occurring upon the resonant excitation of SPPs. One dimensional (1-D) Ag gratings were implemented into the structure of OPV device as electrode to excite the SPPs and a 2-fold improvement in photocurrent was reported [100]. Two-dimensional (2-D) periodic metal corrugation as plasmonic electrode for the replacement of 1-D gratings has been introduced into the structure of an OPV device to overcome the polarization dependence and narrow resonance of SPP modes. A 17.5 % enhancement was achieved in the power conversion efficiency compared to the flat OPV device [101]. Similarly, organic photovoltaic devices integrated with 1-D and 2-D surface relief gratings demonstrated improved incident-photon-to-current conversion efficiencies and an overall increase in power conversion efficiencies, indicating that the corrugated metallic structures as plasmonic electrode induce further photon absorption in the active layer [102].

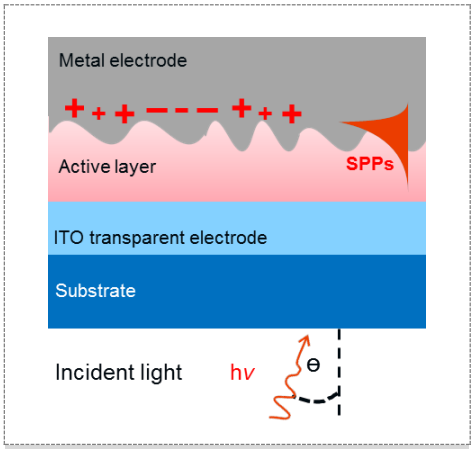

Fig. 1.6: Schematic representation of plasmonic light harvesting approach in OPV device. Coupling of light to surface plasmon polariton propagating along a metal electrode-active layer interface.

The first two methods i.e. light scattering and concentration by localized surface for the light management in the active layer, are not relevant to the work presented in this thesis and will be not discussed further. The focus will be on the third method i.e. light trapping by surface plasmon polaritons, which is the subject of this work and the most common approach used in the thin film solar cells for the manipulation of light. Further, this approach is arguably simpler to implement compared to approaches based on NPs.

1.3.2 Surface plasmon polaritons

SPPs can be excited by electrons or photons. The excitation of SPPs respect both energy and momentum conservation. The excitation by electrons is not relevant to the work presented in this thesis and will not be discussed any further. The focus will lie on the optical excitation of the surface plasmon polaritons. Figure 1.7 shows the schematic representation of the electromagnetic field associated with a surface plasmon polariton propagating along a metal-dielectric interface. The electromagnetic field of SPPs is

confined at the metal surface, with the electric field also enhanced perpendicular to the surface [103, 104]. The dispersion relationship of SPPs [104, 105] can be derived as stated in the following equation

$$K_{sp} = k_0 \sqrt{\frac{{n_d}^2 {n_m}^2}{{n_d}^2 + {n_m}^2}}, \qquad (1.13)$$

where K_{sp} is the wave vector of the SPP; $k_0 = 2\pi/\lambda$ is wavenumber of light in vacuum, n_d is the refractive index of dielectric material and n_m is the refractive index of the metallic material. Figure 1.8 displays the dispersion curve of an SPP mode; a momentum mismatch exists between the photon and SPPs, implying that direct excitation of SPPs with photons is not allowed in the case of a planar interface. The Figure 1.8 also shows graphically the condition for the excitation of the SPPs. The incident photon wave vector K_{in} must be increased by the missing momentum K to allow its coupling to SPPs at given energy $K_{sp} = K_{in} + K$, this condition can be achieved by the one of the following three approaches:

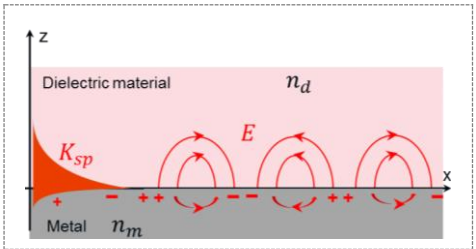

Fig. 1.7: Schematic representation of the electromagnetic field associated with a surface-plasmon polaritons propagating along a metal-dielectric interface. n_d and n_m represents the refractive index of the metal and dielectric regions, respectively.

(i) To use a prism covered with a thin layer of metal to increase the momentum of the incident light. This approach is called attenuated total reflection and was first demonstrated by Kretschmann and Raether [106].

(ii) To apply scattering centers to trigger SPPs [78, 107].

(iii) To employ corrugated metallic films, such as gratings. This is the most common approach used in organic photovoltaic devices for plasmonic light harvesting [70, 108-110].

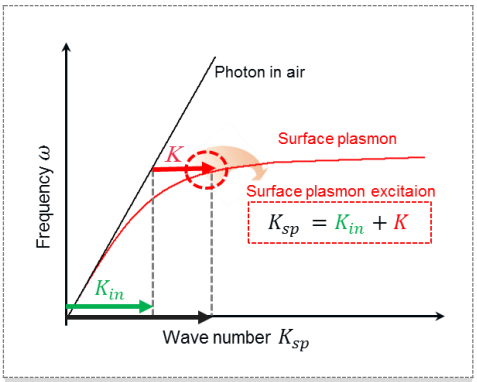

Fig. 1.8: Typical dispersion curve for a surface plasmon and for photon in air, where a momentum mismatch exists between the light and the SPPs. The condition for the excitation of SPPs is also depicted.

1.3.3 Dielectric slab waveguide

Another possible optical absorption enhancement mechanism includes the slab waveguide modes. A dielectric waveguide can be composed of a slab of dielectric material surrounded by media of lower refractive indices having two planar interfaces. In such waveguide configuration the higher refractive index slab represents a core that is surrounded by a lower refractive index cover and substrate [65], as depicted in Figure 1.9. In such configuration, the core slab can support a series of guided waves if its refractive index n_d and thickness d are sufficiently large. In the context of investigated solar cell geometries, let us assume the metallic cover material. Then guided waves can be confined in the core film through the reflecting metal surface and by total internal reflection at the interface with lower refractive index dielectric substrate.

The confined waves in waveguides propagate only at a discrete set of states (which are called modes) for which the field reflected from the metal and dielectric interfaces constructively interfere. In general, the waveguide supports either transverse magnetic (TM) or transverse electric (TE) modes. For TE modes the electric intensity vector E is parallel to the waveguide interfaces and for TM modes the magnetic field intensity H vector is parallel to the surface. The propagation constants β of TM-polarized waves propagating in polymer film can be determined by solving the following dispersion relation [104]:

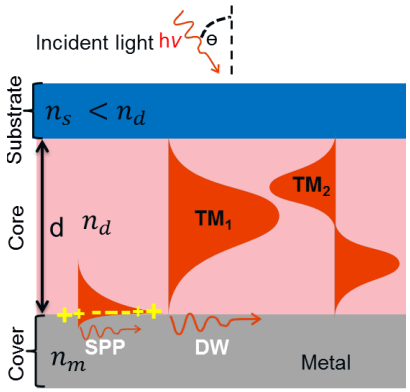

Fig. 1.9: Illustration of the stack of an OPV device as a planar dielectric waveguide, which consists of a slab of dielectric "core" having thickness d in between a lower refractive layer "substrate" and metal "cover". The active layer on a metallic electrode surface supporting guided waves.

$$\tan(kd) = \frac{\frac{\gamma_s n_f^2}{k n_s^2} + \frac{\gamma_m n_f^2}{k n_m^2}}{1 - \left(\frac{\gamma_s n_d^2}{k n_s^2}\right)\left(\frac{\gamma_m n_d^2}{k n_m^2}\right)}, \tag{1.14}$$

where n_d is the refractive index and d is the thickness of the waveguide film. For the TE polarization the dispersion relation yields

$$\tan(kd) = \frac{\frac{\gamma_s}{k} + \frac{\gamma_m}{k}}{1 - \left(\frac{\gamma_s}{k}\right)\left(\frac{\gamma_m}{k}\right)}. \tag{1.15}$$

The terms $k^2 = (k_o^2 n_d^2 - \beta^2)$, $\gamma_c^2 = (\beta^2 - k_o^2 n_m^2)$, and $\gamma_s^2 = (\beta^2 - k_o^2 n_s^2)$ are the transverse propagation constants in the waveguide film, the metal and the substrate, respectively. In general, the number of guided waves in a film slab increases with its thickness and refractive index.

1.3.4 Grating coupling

Grating coupling is a possible means to couple light propagating in the far field to SPPs and dielectric waveguide waves [78, 107]. This can be utilized by periodically corrugating the metal surface as showed in Figure 1.10. When plane wave hits the corrugated surface at certain angle θ, it can become scattered to a series of orders due to diffraction. This process can be described by phase-matching via increasing or decreasing of the parallel component of the incident beam wavevector by grating momentum vector k_g, given by:

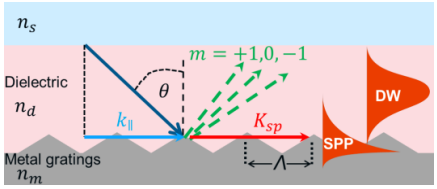

Fig. 1.10: Illustration of grating configuration for exciting SPP. The incident light diffracts into several modes, which can enhance the wave vector of the incident light, coupling light to the surface plasmon at interface between the metallic gratings and dielectric medium and to dielectric waveguide (DW) waves. Λ is the grating period and m is an integer representing the diffraction order.

$$k_g = \frac{2\pi}{\Lambda}, \tag{1.16}$$

where Λ is the grating period. The series of diffracted orders that exhibit the parallel component of their wave vector $k_{\parallel}$ modified as:

$$k'_{\parallel} = k_{\parallel} \pm mk_g = \frac{\omega}{c} sin\theta \pm mk_g, \tag{1.17}$$

where m is an integer. Via the diffraction, the magnitude of the parallel component of the wave vector of the incident light can be increased so it matches the propagation constant β of either the SPPs or dielectric waveguide mode:

$$\beta = \frac{\omega}{c} sin\theta \pm m\frac{2\pi}{\Lambda}. \tag{1.18}$$

This is known as grating coupling condition or phase-matching condition and for the SPPs the propagation constant $\beta = Re\{K_{SP}\}$ is defined in equation (1.13) and for the dielectric waveguides mode β can be obtained by solving (1.14) or (1.15).

1.3.5 Dielectric nanostructures for antireflection

Antireflection (AR) surfaces are desired to reduce reflections and improve the performance of optoelectronic devices including light emitting diodes flat panel displays, photodetectors and thin film solar cells. The AR surfaces have wide applications in photovoltaic technology and are essential for improving the photocurrent generation and *PCE* of the device. For example, the power conversion efficiency was improved by 19 %, by the introduction of a textured foil into the OPV device. The textured foil worked as AR surface and reduced the reflections of the incident light [111]. In another work, AR surface (transparent polymer micro-lens array) was implemented on the light incident surface (front side) of the OPV device, which increased the optical path length of the incident light and reduced the front side surface reflections resulting in a 15–60 % relative increase in the overall power conversion efficiency [112]. Similarly, AR coating (based on zinc oxide nanowires), was implemented on the front side of the OPV device, which enhanced the power conversion efficiency by 36 %. In the following section the basic theory and the mechanism by which AR surfaces operate is discussed.

1.3.5.1 Strategies to achieve antireflection layer

(i) Destructive interference

Destructive interference is the fundamental mechanism behind the thin films coating used for reduction of reflections at an interface. The antireflection coatings consist of one or two or more than two thin films layers. The idea behind an AR coating can be realized from a single layer dielectric thin film with a low refractive index n on a substrate with different refractive index designated as n_s, where $n_s > n$. This configuration leads to a creation of double interfaces, resulting in two reflected waves, see figure 1.11.

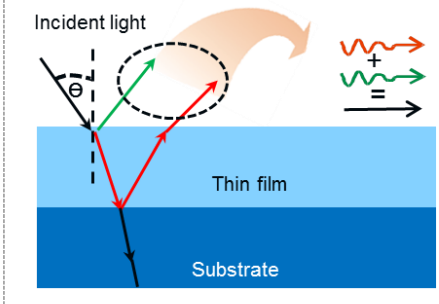

Fig. 1.11: Schematic illustration of an anti-reflection surface which consists of a single thin film coating having destructive interference mechanism for reduction of reflections.

When these two waves are out of phase, destructive interference occurs, cancelling both beams partially or totally before they exit the surface. This is schematically explained in Figure 1.11. The AR based on the destructive interference mechanism only work well for a limited range of wavelengths and angles of incidence [113, 114]. A broadband and angularly independent AR can be achieved by depositing a multilayer with a graded-index, but their processing can become complex and expensive [115]. The condition for good AR from multilayer system would be the same as that of a single film i.e. the refractive indices of the thin layers on the interface should be in increasing order from the air to the optical substrate. In multilayer system the reflection/transmission on each interface is very crucial and important as it governs the resulting AR from the system [116].

(ii) Multiple reflections

The mechanism behind the multiple reflections is texturing surfaces with geometric features i.e. microstructures [117, 118]. The microstructures could be either periodic regular or random, which leads to reduction of the reflection from the surfaces for incident light. This approach is very common and vital in industrial silicon solar cells as the un-textured silicon wafer reflects more than 30 % of the incident light [119]. To reduce reflections and produce AR behaviour in the industrial mono/multi-crystalline silicon solar cells, the top/front surface of Si wafer is textured [117, 119]. This texture typically comprises of overlapping pyramids having random heights and locations, see Figure 1.12(b). Texturing (usually upright randomly placed pyramids) causes reflected light to strike a second surface before it can escape, increasing the probability of absorption. The multiple reflections mechanism is explained schematically in Figure 1.12(a). The size of the microstructures used for the multiple reflections mechanism is quite large, and can't be applied inside the structure of the OPV device due to the thin photoactive layer (80–150nm). This type of microstructures are only applied on the top/front side (out-side of the OPV device) for the light harvesting purpose [120]. The size and geometry of the microstructures is very important as it influences the incident light on a solar cell device and it is optimized generally for antireflection of the visible spectrum (~400–700 nm).

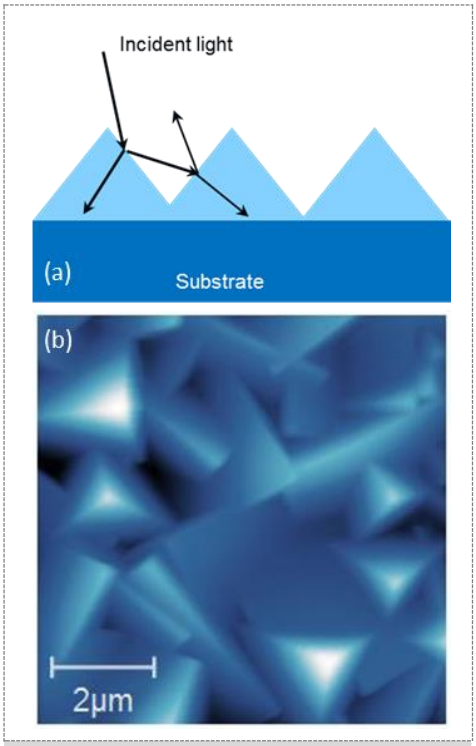

Fig. 1.12: (a) Schematic illustration of anti-reflection surface based on multiple reflections mechanism (b) Atomic force microscopy micrograph of a textured AR surface consists of randomly placed pyramid having random heights.

(iii) Nanostructured graded index

The first two approaches for AR is not relevant to the work presented in this thesis and will not be discussed any further. This focus will be on the so called nanostructured graded index [121, 122] method, which is arguably the most common approach used in

OPV solar cells. Moth eye nanostructures (MEN) are the most common example of nanostructured graded index method. MEN were discovered by Bernhard, Miller and Moller from nature on the corneas of night active insects [123, 124] and first artificially produced by Clapham and Hutley [125]. The MEN typically consist of arrays of nano-pillars or nanocones with spatial periodicity usually below the wavelength of the visible spectrum [126].

The basic principle of MEN antireflective surface is that the outer surface consists of nipple arrays, typically of sub-micron height and spacing [126]. The theory to describe how these MEN reduce reflections is known as the effective medium theory (EMT) [127-129]. The EMT theory was introduced to describe the effective dielectric constant of homogenously mixed materials. According to this theory as the fraction of air around these structures decrease gradually from the top of the tip of the nanostructure to its base, the effective refractive index (RI) changes gradually. Therefore, the incident light goes through the surface as if it is going through a gradient index environment, thus rendering low reflectance. The theory works generally well for both regular fine surface relief and random porous structures.

Figure 1.13 schematically explains the concept of MEN. The RI of the surface layer varies gradually from air to substrate, and effectively suppresses the specular reflectance at the interface of the two media. The optimum design of MEN AR surface can be analyzed from the dependence of the reflectance on the effective height h and spacing or period Λ of the nanostructures, and on the wavelength of the incident light. Another available theory is to view moth eye type nanostructures as an optical diffractive element with a surface-relief structure in two-dimension that only produces zero-ordered diffraction. To explain this effect, a 1-D surface-relief grating or a simple 1-D sub-wavelength grating structure having a period Λ is often discussed [130]. When a beam of incident light goes through a grating, it can be described by the following grating equation

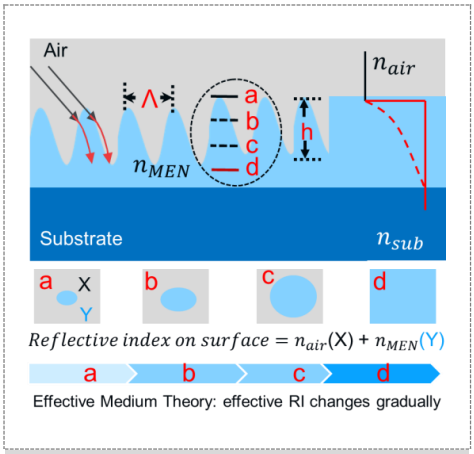

Fig. 1.13: Schematic illustration of anti-reflection surfaces with graded index mechanism. The periodic structure varying refractive index from air to substrate. Where "X" and "Y" represents the area ratio of air and MEN respectively.

$$\frac{m\lambda}{\Lambda} = (n_{sub}\, sin\, \theta_{sub}) - (n_{air}\, sin\, \theta_{air}). \tag{1.19}$$

In the above equation (1.16), n_{sub} and n_{air} are the refactive indices of the substrate and the air respectively; θ_{sub} represents the angle of the diffracted light beam and θ_{air} is the incident angle of the light; m is the diffracted order of the light and λ is the wavelength of the light. From equation (1.16), it can be deduced that the Λ of the grating structure should fulfil the condition as given in the below equation if there is only zero-ordered diffraction occurring

$$\Lambda < \frac{\lambda}{n_{sub} + n_{air}}. \tag{1.20}$$

Therefore, the moth-eye type antireflection calls for nanostructured surfaces having sub-wavelength periods. Further, the 1-D grating equation can be applied to 2-D gratings and to the nanostructures consisting of periodic arrays of pillars in artificial MEN by considering light incident at specific azimuthal angles related to the symmetry of the array [131].

Chapter 2 Research goals

The optical losses have a direct impact on the photo-generated current of the OPV device as they compete with the generation of excitons in the active layer. The main contributions to the optical losses can be attributed to the incomplete absorption of light in the active layer (since it is composed of materials with low carrier mobility which limits the film thickness) and optical reflections (due to the abrupt change in refractive index). To date, various approaches have been pursued to reduce such losses and thus to improve the performance of the OPV devices [60, 69, 72, 111, 132, 133]. The present work aims at pushing forward the performance improvement in this field by developing novel type of metallic and dielectric nanostructures tailored for the efficient manipulation of light in OPV solar cell architectures. By controlling and designing the nanoscale geometry, it is possible to confine the incident light in specific sections of the OPV device where it should be absorbed and contribute to excitons generation. Therefore, parasitic effects occurring outside this region such as reflections at interface of the stack of layers can be suppressed. The work particularly focuses on means of preparation of suitable structures on large areas in order to address the need of their scaled up production. The work is organized along the lines of four projects as specified below.

2.1 Broadband light harvesting plasmonic nanostructures

Chapter 4, section 4.1 presents a new approach for broadband light harvesting at a metallic electrode by using multi-diffractive plasmonic nanostructures. In general, resonant coupling of light to surface plasmons at surfaces of metallic films and nanoparticles can substantially enhance the absorption of light in the active layers of solar cells [70, 78, 134]. This strategy enables the utilization of absorber materials (active layer) with short carrier diffusion length such as those that are used in common OPV solar cells architectures [90, 94, 98, 101]. Since resonant light coupling to plasmonic modes occurs at narrow spectral windows, the positive effect of light harvesting is limited to certain wavelengths band that does not cover the broad spectrum of solar radiation. In order to address this challenge, the use of multi-diffractive gratings is

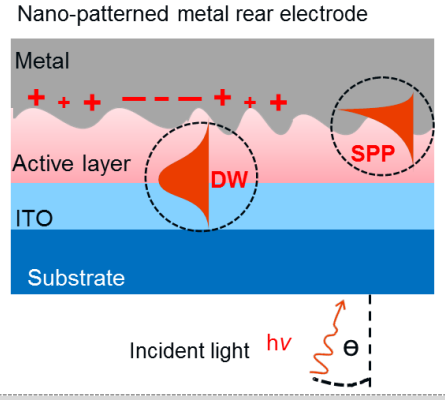

Fig. 2.1: Schematic of the research goal, a novel multi-diffractive plasmonic absorber for OPV device serve as plasmonic light trapping element and rear electrode. The plasmonic absorber could support the surface plasmon polaritons (SPPs) and additional waveguide modes (DW).

proposed, which can be incorporated to the OPV solar cell structure to serve simultaneously as broadband plasmonic absorber for light trapping and as well as a rear electrode, see Figure 2.1.

2.2 Broadband antireflection and broadband light trapping by dielectric nanostructures

Apart from using plasmonic nanostructure-based light harvesting, dielectric nanostructures have been also reported for light harvesting in OPV solar cells [133]. Chapter 4, section 4.2 presents results on optical manipulation of light for OPV solar cells based on nanostructured ITO electrode. ITO is one of common transparent conducting oxide materials, widely used as transparent electrode in OPV solar cells due to its relatively low refractive index as well as good optical and electrical properties [135-138]. To obtain state-of-the-art optical and electrical properties, ITO films are commonly deposited at high temperature or require high temperature post deposition steps [105, 124, 139-141]. The implementation of nanostructured ITO films that has been developed up to now [142-144] for light management, rely on complex, multi-step processing, and post deposition treatment which is a handicap for e.g. flexible substrate devices. To overcome this problem, nanostructured ITO films were prepared by adopting combination of sputtering at ambient temperature and UV nanoimprint lithography. The fabricated nanostructured ITO films can be incorporated to the OPV solar cell structure to serve simultaneously as light trapping or antireflection (moth eye) element at specific spectral windows. A broadband antireflection design of transparent ITO electrode was achieved for suppressing the Fresnel reflections at an interface and yielding high transmittance over a broad spectral and angular range compared to state-of-the-art flat ITO electrode. Furthermore, the same geometry was adopted for efficient light trapping by the use of diffraction coupling to series of waveguide modes supported by the ITO film, (see Figure 2.2).

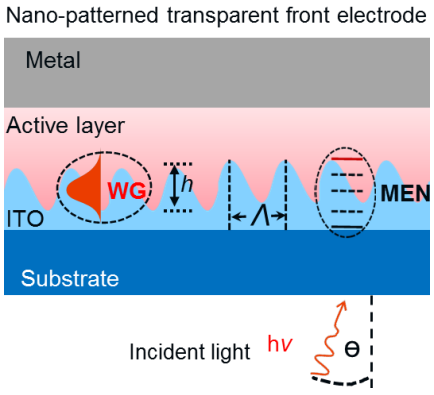

Fig. 2.2: Schematic of the front ITO electrode, which is corrugated to exhibit light trapping or antireflection properties at specific spectral windows. Depending on the period Λ and height h of the nanostructures, the wavelength-scale grating structures of ITO electrode could support the AR properties (MEN) or can produce significant absorption waveguide (DW) resonances in OPV solar cell architecture.

2.3 Metal nanowires

Chapter 4, section 4.3 deals with preparation and characterization of multi-diffractive arrays of metal nanowires (NWs). As discussed in chapter 1, one of the limiting factor of *PCE* is the low carries mobility of organic solar cells, which leads to poor charge collection [145]. In order to overcome this limit and enhance the *PCE,* metallic nanowires (NWs) can be incorporated into the structure of OPV devices. The incorporated NWs can provide direct pathways for fast charge transport. Furthermore, the research on metal NWs in the field of OPV focuses on three main purposes, replacement of transparent conductive (TCO) electrodes [146], light management [146] and enhancement of the conductivity of TCO electrodes [147]. The common model structure is a periodic nano-line (1D-nanogratings)/nano-wire or metallic nanogrid (2D) which have been extensively studied and has long been the focus of intensive research [148-152]. The fabrication of such structures has typically been carried out using focused ion beam milling or electron-beam lithography techniques that are relatively expensive and time consuming. In this work, an unconventional geometry that comprises multi-periodic plasmonic NWs is prepared by a combination of laser interference lithography over large areas.

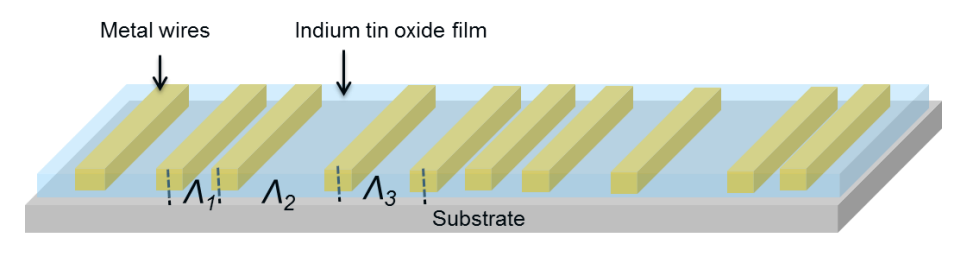

Fig. 2.3: Schematic of the investigated geometry for plasmonic transparent electrode based on multi-periodic metallic nanowires and thin ITO film.

2.4 Collaborative projects biosensors

In addition, series of collaborative projects out of the scope of OPVs were carried out as described in Chapter 4, section 4.4. These projects mainly focused on the application of developed plasmonic structures and protocols to prepare them for optical biosensors. In particular, these additional projects concern the utilization of compact surface plasmon resonance biosensor based on diffraction coupled-SPR on gold gratings, surface-enhanced Raman spectroscopy on arrays of gold nanoparticles, and SPR measurements in the ultraviolet part of spectrum with the use of aluminium gratings.

Chapter 3 Methods

3.1 Fabrication of nanostructures

3.1.1 Laser interference lithography

The laser interference lithography is a relatively simple, fast, cost-effective, and large- scale method compared to other ones such as e-beam lithography [153]. The schematic of the LIL using Lloyd's mirror configuration used in this work is shown in Figure 3.1. It utilizes of a laser source, microscope objective lens, a lens, a pinhole and a mirror. The mirror is placed perpendicular to the exposed surface of the sample to create a second beam. The laser HeCd source having output power of 4 mW, (model IK 3031 R-C from Kimmon) operating at λ= 325 nm is focused by a 40x microscope objective lens (LMU-40X-NUV, Thorlabs) to a pin hole with diameter of 10 µm. The combination of microscope objective lens, pinhole and lens expands the beam and makes its intensity homogeneous. This enables recording large areas (about 15 x 15 mm) with high intensity (32 µWcm^{-2}). The expanded and homogeneous beam is made incident on a sample holder which consisting of a rectangular dielectric mirror (RM-50.0-30.00-12.7-UV, CVI Melles Griot) and a holder for the sample. The sample holder can be rotated by an angle θ. The schematic of the two beam interference is shown in Figure 3.2(a), both beam generate a periodic interference pattern on photoresist surface. The period Λ of the recorded pattern into photoresist thin film can be calculated by following equation

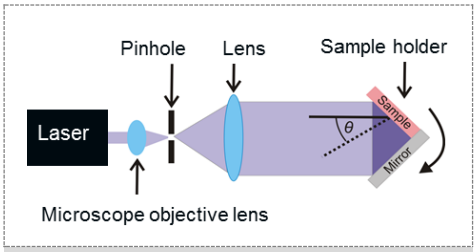

Fig. 3.1: Schematic of the laser interference lithography used for the nanostructures fabrication. The wavelength of laser is λ= 325nm and an output power 4 mW.

$$\Lambda = \frac{\lambda}{2sin\theta}, \tag{3.1}$$

where θ is the half angle of two incident beams intersect angle and λ is the wavelength of laser. Furthermore, the profile of intensity distribution of the interference of two beams at the sample surface (photoresist) is crucial for fabricating uniform patterns especially on large area. The intensity *I(x)* is given by the following equation [154, 155]

$$I(x) = 2A\left\{cos\left[\frac{4\pi x}{\lambda}\sin(\theta)\right] + 1\right\}, \tag{3.2}$$

where A is the wave amplitude of the partial beams.

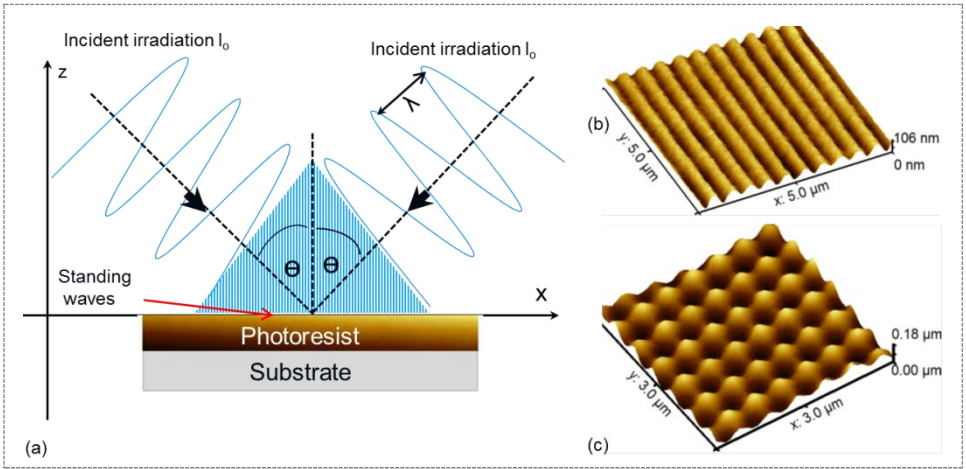

Fig. 3.2: (a) Schematic of two beams interference lithography. The directions of the two beams are shown by dashed arrows. Both beams generate an interference (standing waves) periodic pattern, which is recorded in a thin layer of photoresist on a substrate. (b) A 3D view of an AFM micrograph which is produced by single exposure results sinusoidal grating pattern. (c) A 3D view of an AFM micrograph which is generated by two exposures with a 90° rotation of the sample in between.

In this study positive photoresist Microposit S1805 from Microchem (USA) was used as photosensitive material for recording an interference field pattern. First, the photoresist layer was spun onto a BK7 clean glass substrate (area=20 × 20 mm) at 4500 rpm for 45 s (spin-coating parameters) yielding a thickness of 400 nm. In order to reduce the thickness, photoresist was diluted (1:2) with propylene glycol monomethyl ether acetate, yielding a thickness of 100 nm. Then, a soft baking step on a hot plate at 98 °C was applied for 120 s. Afterward, the substrate was mounted to the laser interference setup and exposed to the field of collimated interfering beams (with intensity of 32 µW cm^{-2}) emitted from a HeCd laser at wavelength λ = 325 nm. Then the recorded interference field pattern was etched into the photoresist by a developer AZ 303 from MicroChemicals (Germany) that was diluted by distilled water at a ratio of 1:15.

3.1.2 Nanoimprint lithography

A nanoimprint lithography used in this study is one of the most promising methods for nano-sized patterning due to its low cost, high throughput possibilities and simplicity resolution scalability and pattern repeatability [138]. A master with relief patterns and stamp are the two important components of the nanoimprint lithography technique. A master is first fabricated by conventional lithography techniques (photolithography, laser interference lithography or electron beam lithography).

The materials used for the stamp polydimethylsiloxane (PDMS) obtained under commercial name Sylgard 184 (Dow Corning USA). The PDMS is heat curing and consists of two components, i.e. a base part and a curing agent part. To make stamp, one part curing agent and ten parts of base (by weight) are mixed. Then stamp is made from the master, the steps are schematically shown and explained in Figure 3.3(a). In this work the photoresist nanostructured (Master prepared with LIL) were casted to PDMS, followed by a curing step for 3 days at room temperature. The PDMS copy was detached from the master and employed as a working stamp. The stamp is the key in nanoimprint lithography since it is used to generate and transfer the nanostructure pattern from master

to replica. Let us briefly describe the key NIL process for making copies from the master, which consists of the following steps.

3.1.2.1 Cleaning of substrate

Glass BK7 is used as a substrate in this work with a dimension of 25 × 25 mm. Substrates were cleaned by sonication in 1% Hellmanex (from Hellma GmbH & Co. KG, Germany) solution, followed by distilled water and ethanol for 15 minutes each and then blown-dry using air gun.

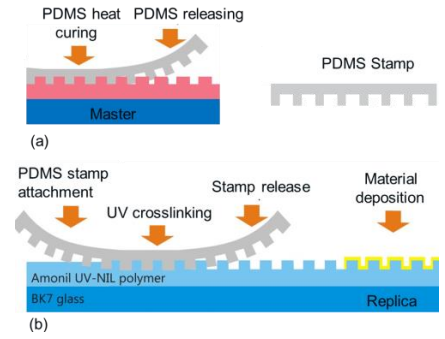

Fig. 3.3: Schematic of NIL (a) preparation of PDMS stamp from Master. Firstly, liquid PDMS is cast over a master containing the nanostructure pattern that is to be reproduced. The PDMS is then heat cured and released. (b) PDMS stamp is attached to a BK7 glass substrate with spin coated resist film on top, followed by crosslinking and removal of the stamp process.

3.1.2.2 Spin-coating of polymer on substrate

After the cleaning process, the imprint UV-curable polymer Amonil MMS 10 (from AMO GmbH) is spin coated on a clean glass substrate. In this study spin coater SCS G3 system (from Specialty Coating Systems USA) was used, the spin- coating parameters were set to 2000 rpm for 120 s which results in a layer thickness of 120 nm.

3.1.2.3 Nanoimprint process

During the imprint step, a PDMS stamp with nanostructures on its surface is pressed into a thin resist (Amonil) cast on a substrate, followed by crosslinking (in UV-chamber) and stamp release process. These steps duplicate the nanostructures on the stamp in the resist film. This is schematically shown in Figure 3.3 and the device used for imprint step is shown in Figure 3.4. In this study the crosslinking of Amonil layer was done by UV light (UV lamp Bio-Link 365 from Vilber Lourmat with the wavelength λ = 365 nm). The irradiation dose was set to 5 J cm^{-2}.

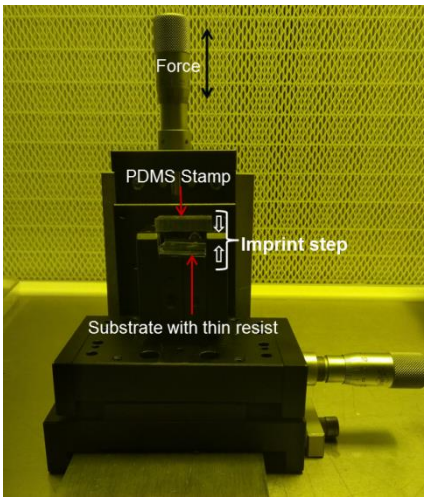

Fig. 3.4: A device made for nanoimprint step in NIL technique. The PDMS stamp with nanostructures on its surface is pressed into a thin resist cast on a substrate.

3.1.2.4 Characterization

The morphology of the imprinted structures is observed by an atomic force microscope (AFM) or scanning electron microscope (SEM).

3.2 Material deposition

DC magnetron sputtering UNIVEX 450C (from Leybold Systems, Germany) is used for the thin films deposition in this study. The basic working principle of a magnetron sputtering system is schematically shown in Figure 3.5. The basic processes in DC magnetron sputtering are as follows:

In high vacuum chamber (pressure of 1 to 10 mTorr) inert gas atoms (typically Argon) are introduced. Then a DC voltage is placed between the target (source of the material desired to be deposited) and substrate, which ionizes argon atoms and creates plasma (ions and electron) in the chamber. This kind of set-up for sputtering was first discussed in the literature by W.R. Grove in 1852 [156].

Electrons released during argon ionization are accelerated towards the substrate, subsequently colliding with additional argon atoms, creating more ions and free electrons in the process. The ions are accelerated to the target and bombarded, their collision with the target ejects target atoms, which travel to the substrate and start to condense into a thin film [157]. One or more layers of ejected atoms can be created at will depending on the sputtering time, allowing for production of precise layered thin-film structures. In this study a 4-inch diameter Al and ITO target were used for plasmonic and dielectric nanostructures fabrication respectively.

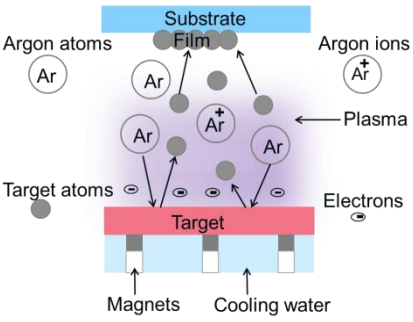

Fig. 3.5: Schematic shows the basics components and process of a magnetron sputtering system for the thin film deposition. The arrangement of the magnets creates a suitable magnetic field for the circulation of electrons near to the target surface and thus creates high density plasma. The closed-loop water-cooling circuit is for temperature control of the substrate.

The target to substrate distance was about 10 cm. The sputtering process was done with the substrate cooled at 25 °C using a closed-loop water-cooling circuit.

3.3 Characterization

3.3.1 Optical characterization

The samples were optically characterized using a Bruker Vertex 70 Fourier transform infrared spectrometer (FTIR), additionally equipped with a visible light source and integration sphere. The system is capable of making high quality transmission and reflection measurements. Direct transmittance was measured for normal incident light and referenced to the sample holder without sample (air). The optical system used for the angular reflectivity and transmission measurements in this work is home-made and it is schematically shown

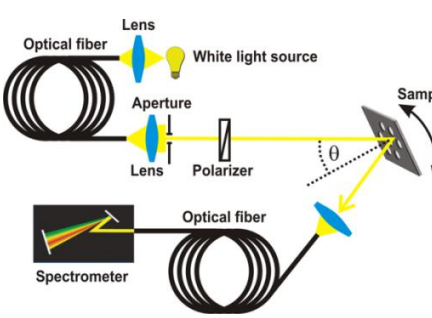

Fig. 3.6: Schematic of a home-made angular wavelength developed system used for the angular transmittance and reflectivity measurements typically from an angle of 0.3° to 60°.

in Figure 3.6. The system consists of a white light source (halogen lamp from LSH102 from LOT-Oriel) that is connected to an optical fiber M25L02 from Thorlabs (UK). The light emitted from the optical fiber tip is collimated by an achromatic lens 14 KLA 001 CVI from Melles Griot (Germany). For the angular reflectivity measurements, the collimated light beam is made incident at the sample, mounted on a motor controlled rotation stage from Huber GmbH (Germany). One motor was used for the control of angle of incidence, while the second motor was employed for rotating the optics

collecting the reflected light. For the angular transmission measurements, the second motor carrying the optics is fixed. The reflected/transmitted beam is coupled by the collimator F810SMA-635 from Thorlabs (UK) into an optical fiber M26L02 from Thorlabs (USA) that is connected to a spectrometer HR4000 from Ocean Optics (USA). Data acquisition and system control is performed by software developed in LabVIEW from National Instruments (USA).

3.3.2 Morphological characterization

The morphological characterization in this work was carried out for the prepared nanostructure by using nanoscale microscopy, which includes scanning electron microscopy and atomic force microscopy.

3.3.2.1 Scanning electron microscopy

Scanning Electron Microscopy (SEM) is a powerful method for the investigation of surfaces and can be used for precise measurement of small features and objects down to few nanometer in size. Figure 3.7 shows a schematic of typical SEM and its essential components. It consists of an electron source (electron gun), a series of lenses (condenser and objective), scanning coils and detector system. The electron beam (with energies typically up to 40 keV) produced by the electron gun is directed through condenser and objective lenses onto a sample in the sample chamber and scanned along a pattern of parallel lines. During the scanning the interaction of electron beam with sample generates a number of different types of signals (secondary electron, backscattered electrons characteristic X-rays) emitted from the area where the electron beam is impinging. These various signals are collected by a detector to form an image or data-set which provides the topographical, morphological and compositional information of the scanned surface of the sample [158].

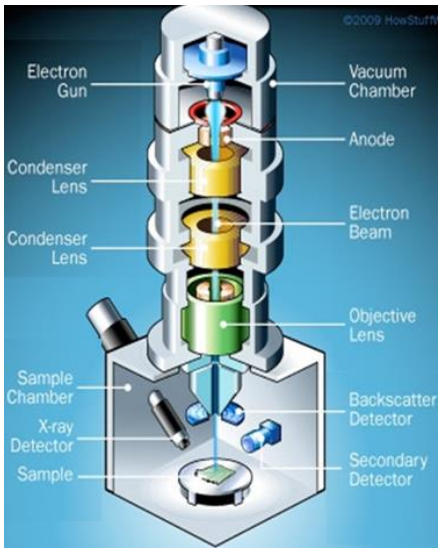

Fig. 3.7: Schematic diagram of a SEM. The electron beam produced by electron source is focussed onto the sample; a number of signals are generated due to interaction. These signals include secondary electrons, backscattered electrons. Image from: (science.howstuffworks.com)

(i) Secondary electrons

When the electrons of the SEM beam collide with electrons of the atoms of the sample, some of the more weakly bound electrons may be ejected from these atoms, they are referred to as "secondary electrons (SE)". Technically, any electron ejected from an atom due to the collision with another high energy electron is a secondary electron. These electrons are fairly low energy electrons (~ a few tens of eV) and emanate near the surface of the sample. The SE emanating deeper in the specimen are easily absorbed by the mass of the sample. The SE from the sample is attracted towards the tip of a detector known as secondary electron detector by applying voltage (typically 10 keV). The SE produces light, when it hits the fluorescent substance of the SE detector. The produced light is directed to a photomultiplier tube and finally converted to electrons.

These electrons are amplified as electric signal. Thus, the secondary electrons are useful in imaging the sample and the images produced by secondary electrons mainly provide morphology and topography information of the specimen surface. In this work, surface images of the prepared nanostructure films were recorded by SEM (Zeiss SUPRA 40) using an in-lens detector and 5 kV beam acceleration voltage.

(ii) Backscattered electrons and characteristic X-rays

When the electrons of incident beam collide with the nucleus of an atom of the sample it may be scattered in any direction without losing much of its energy. Those electrons scattered back towards the detector are referred to as "backscattered" electrons. They are often useful in imaging sample with a high mean atomic number and are thus often informative for determining the composition of the scanned sample. Higher accelerating voltages of the beam and higher mean atomic number samples atoms will yield greater backscattered electron signals. Furthermore in conjunction with SEM, energy dispersive x-ray spectroscopy is technique that utilizes x-ray emitted from the sample during the interaction of electron beam to characterize a localized chemical analysis (mostly elemental composition) of material imaged in a SEM [159].

3.3.2.2 Atomic force microscopy

Atomic force microscopy (AFM) is based on sensing the forces (Van der Waals forces, dipole-dipole interactions, electrostatic forces) between a sharp tip (<10 nm) and the surface of sample, this allows the atomic resolution images of surfaces and the determination of the surface topography in the nanometer. One of the most common models of AFM is schematically depicted in Figure 3.8(a). The tip is supported on a flexible cantilever. AFM tips and cantilevers are typically micro-fabricated from silicon nitride or silicon nitride Si_3N_4. Typical tip radius is from a few to 10s of nm.

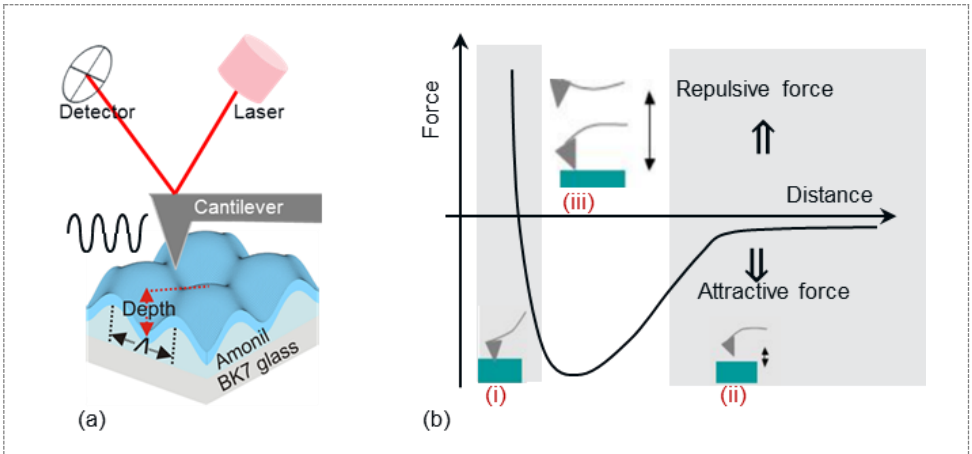

Fig. 3.8: (a) Schematic of the basic AFM model. (b) A typical force–distance curve showing three regions for three primary imaging modes (i) Contact mode: when the spring constant of cantilever is less than surface, the cantilever bends due to repulsive VdW forces on the tip. An image of the surface is obtained in this region, by maintaining a constant cantilever deflection (using the feedback loops) thus the force between the tip and the sample remains constant (ii) Non-contact mode: the tip does not contact the sample surface, but oscillates above the surface during scanning. The feedback electronic loop is used to monitor changes in the amplitude due to attractive VdW forces the surface topography can be measured and (iii) Tapping mode: the tip touch the surface only for a short time thus avoiding the issue of lateral forces and drag across the surface.

The forces between the tip and the surface of the sample lead to a deflection of the cantilever according to Hooke´s law $F = -kx$, where F is the force, k is spring constant

and x is the deflection of cantilever. The dominant interactions at short tip-sample distances in the AFM system are Van der Waals (VdW) interactions [160]. When the tip is in contact with the sample, it predominately experiences repulsive Van der Waals forces as shown in the force-distance curve in Figure 3.8(b-i). This mode of AFM operation is known as contact mode. As the tip moves further away from the surface of the sample attractive VdW forces are dominant as shown in force-distance curve. This mode of AFM operation is known as non-contact mode and it is schematically shown and explained in Figure 3.8(b-ii). A laser beam deflection system (reflecting from cantilever) is the most common detection method used in modern commercial AFMs, it was pioneered by Meyer and Amer [161, 162]. To acquire the image resolution, AFMs can generally measure the vertical and lateral deflections (reflecting a laser beam off the cantilever). The reflected laser beam strikes a position-sensitive photo-detector consisting of four-segment photo-detector, as shown schematically in Figure 3.8(a). The differences between the segments of photo-detector of signals indicate the position of the laser spot on the detector and thus the angular deflections of the cantilever. The deflections of the cantilever is controlled by piezoelectric elements and a feedback electronics loop system in the AFM set-up [160]. Besides high resolution and the determination of three-dimensional images, AFM allows the examination of all kind of samples in ambient atmosphere for example non-conductive and even surfaces in liquid can be scanned. In this work the periodicity, modulation depths and images of the prepared nanostructures were achieved by using AFM instrument from Molecular Imaging (USA). Tapping mode and standard tapping mode AFM tips PPP-NCHR-50 from NanoAndMore (USA) were used.

Chapter 4 Results

4.1 Plasmonic nanostructures for light manipulation

The coupling of light to surface plasmons that originate from collective oscillations of free electrons at metallic surfaces allows tightly confining its energy. Such plasmonic confinement of electromagnetic field allows bridging between dimensions dictated by the sub-micrometer wavelength of light in visible and near infrared (NIR) part of spectrum and nanoscale size of species which are often used as emitting or absorbing materials [163]. Currently, we witnessed numerous approaches to plasmonic light management in optical devices including thin film photovoltaics [164] and light emitting diodes [165]. In these technologies, the implemented plasmonic structures are typically designed to couple light over broad range of wavelengths and angles of incidence. For plasmonic broadband absorption of light, the majority of explored metallic structures support localized surface plasmons (LSPs). The most common approach implies a geometry consisting of metallic nanoparticles that are separated from a continuous metallic surface by a thin dielectric spacer. Such metal-dielectric-metal configurations were investigated in form of periodic arrays of rectangular and cylindrical nanoparticles [166] or nanoholes [167] and they showed the possibility to harvest light over broad range of angles of incidence. However, the resonant coupling to LSPs typically occurs only in a very narrow spectral window. In order to broaden the LSP resonance, superimposing multiple LSP resonances was investigated by stacking of nanoparticles perpendicular to the surface [168], by arranging arrays of nanoparticles with different size in the lateral direction [169], or by using nanostructures with more complex shapes [167, 170]. Exploitation of propagating surface plasmons (PSPs) travelling along continuous metallic films was proposed for broadband absorption of light by using geometries with singularities [171]. This concept was experimentally carried out by using arrays of deep convex gold slits that were adiabatically tapered. Structures with slit tapers featuring the width as small as ~ 10 nm were prepared by focused ion beam (FIB) milling and broadband absorption of light over visible and near infrared part of spectrum was demonstrated [172]. Contrary to these, shallow periodic corrugation of metallic surfaces can be utilized by simpler means of fabrication over large areas by techniques such as laser interference lithography (LIL) or nanoimprint lithography (NIL). When coated with a metal, these structures act as gratings that can be tuned to nearly perfectly absorb light by diffraction coupling to PSPs. However, similar to LSPs, the diffraction excitation of PSPs is resonant and occurs only at narrow wavelength band which is highly sensitive to variations in the angle of incidence. In order to broaden the wavelength range where light is absorbed by diffraction coupling to PSPs, a metallic film with a periodically corrugated interface in the lateral direction was interfaced with one-dimensional photonic crystal in the direction perpendicular to the surface, generating a rich spectrum of surface plasmon-like modes [173]. Besides periodic structures, also non-periodic patterns were investigated for broadband collecting of light by diffraction and scattering-based coupling to optical waveguide modes and PSPs. It should be noted that the excitation and scattering of PSP on rough metallic surfaces was a subject to studies since seventies in the last century

[174]. More recently we witnessed investigations on engineered randomized arrays of metallic bars [175] and dielectric pillars [176] for trapping in optical waveguides and metallic films with quasiperiodic arrays of nanoholes [177] and relief gratings [178] for the excitation of SPPs that were fabricated by electron beam lithography or FIB. Here we present a new type of broadband plasmonic absorber that relies on a periodic corrugation of metallic surface with multiple superimposed spatial frequencies. This approach allows for simultaneous diffraction coupling to PSPs at series of resonant wavelengths that span over a broad spectral range. The structures exhibit low aspect ratio features which makes them compatible with a range of thin film devices where active layers (thickness in the range of 100–200 nm) are used to emit or absorb light propagating at broad range of incident angles and wavelengths in the far field.

4.1.1 Results and Discussions

4.1.1.1 Investigated geometry

The investigated geometry consists of a metallic surface with relief corrugation profile that comprises multiple spatial frequencies. As indicated in Figure 4.1(a), this corrugation was designed to simultaneously excite PSPs at a series of distinct wavelengths. The corrugation (multi-diffractive grating nanostructures) was prepared by sequential LIL recording of a periodic sinusoidal interference pattern with varied period Λ into a photoresist layer. The angle of the interfering beams (intensity 32 μW/cm^2) was set to 17.68, 15.39 and 13.62 deg which corresponds to periods of Λ_1=535, Λ_2=612 and Λ_3=690 nm, respectively. In order to record a multi-diffractive structure, the photoresist layer was sequentially exposed to the interference field at each respective angle for 95 seconds. For the preparation of crossed gratings, the sequential exposure to interference fields was carried out twice for two orientations of the sample rotated by 90 degrees. Prepared photoresist grating were developed, and afterwards copied by UV nanoimprint lithography (UV-NIL) into 200 nm thick layer of Amonil MMS10 from AMO Gmbh (Germany). Such prepared replicas were subsequently coated with Al film with a thickness of d_{Al} ~100 nm by sputtering (UNIVEX 450C from Leybold Systems, Germany) and photoactive layer with a thickness of about d_a=35–40 nm. It should be noted that each sample comprised an area that was structured and an area that was flat and served as a reference in the optical measurements.

The materials used for making the photoactive layer film are regioregular poly(3-hexylthiophen-2,5-diyl) (P3HT) with a molecular weight MW=25–45 kDa and the fullerene derivative [6,6]-phenyl-C61-butyric acid methyl ester (PCBM), obtained from Sigma Aldrich (used without further purification). Both polymer materials were dissolved in chlorobenzene in a ratio of 1:1 and stirred at temperature of 70 °C for 3 h. To ensure a complete dissolution of P3HT and PCBM, the polymer blend was stirred for an additional 15 h at room temperature. For the demonstration of plasmonic multi-diffractive absorber, the P3HT: PCBM polymer blend (9 g L^{-1}) was spun onto the multi-diffractive grating structure coated with 100 nm of Al at 1200 rpm for 120 s. After the thermal annealing at 150 °C for 15 min, the thickness of prepared polymer film of d_a=35–40 was determined on a reference flat glass substrate.

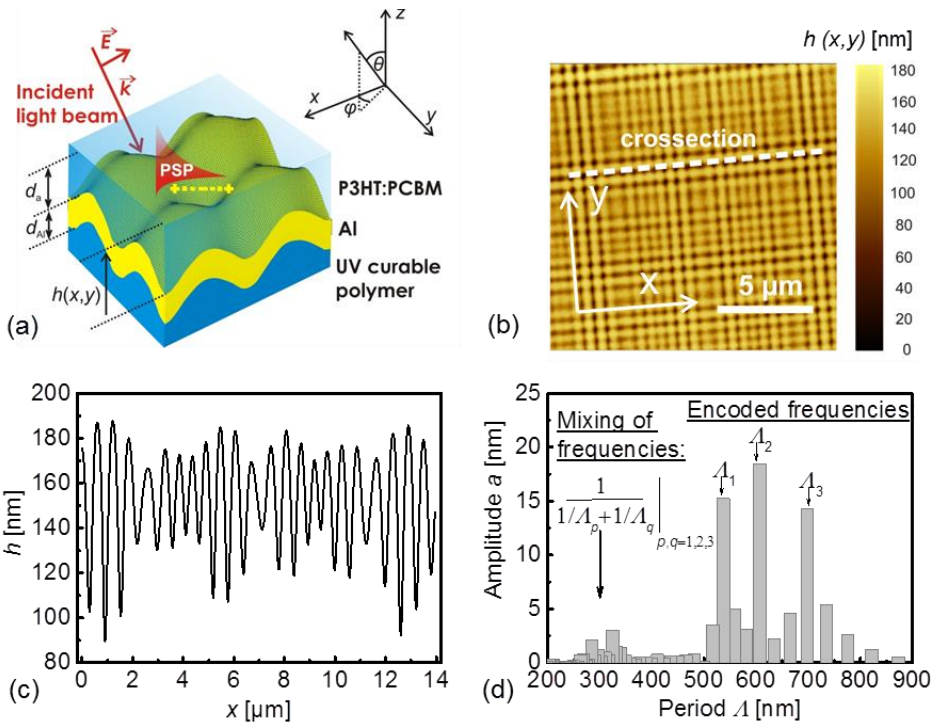

Fig. 4.1: (a) Geometry of a multi-diffractive grating with Al and P3HT: PCBM layers, (b) corrugation profile of 2D crossed multi-diffractive grating observed with AFM and (c) cross-section of the height dependence *h(x)* indicated as a dashed line in (b) with (d) respective FFT spectrum. Adapted with permission from **[179]**.

P3HT: PCBM was chosen as a model material because it is commonly used as the photoactive material layer in organic photovoltaic research [180]. This polymer blend strongly absorbs light at wavelengths around 500 nm but above the wavelength of 600 nm its absorption rapidly decreases. In order to absorb light in P3HT: PCBM more efficiently in the spectral window between 600–750 nm, the underneath Al surface was corrugated by a crossed grating with three encoded periods Λ_1=535 nm, Λ_2=612 nm, and Λ_3=690 nm as shown in Figure 4.1(b). Fourier transform analysis of a corrugation profile cross-section that is shown in Figure 4.1(c) was used to determine amplitudes a_1, a_2, and a_3 for each recorded period Λ_1, Λ_2, and Λ_3, respectively. The obtained Fourier spectrum in Figure 4.1(d) reveals that the prepared corrugation profile exhibits distinct peaks corresponding to modulation amplitudes of a_1=15.3 nm, a_2=18.5 nm, a_3=14.3 nm. In general, superimposing of spatial frequencies leads to their mixing and thus there occur additional modulations with periods $1/(1/\Lambda_p \pm 1/\Lambda_q)$, where p and q are integers. For the selected periods Λ_1, Λ_2, and Λ_3, the subtractive frequency mixing $1/(1/\Lambda_p - 1/\Lambda_q)$ gives rise to periods Λ of several micrometres. On the other side, the additive mixing $1/(1/\Lambda_p + 1/\Lambda_q)$ is represented by series of peaks at Λ=260–350 nm in the Fourier transform spectrum.

4.1.1.2 Choice of the periods

The periods in the investigated geometry were chosen based on the phase-matching condition in order to couple normally incident light to PSPs at the interface between Al and P3HT: PCBM. The coupling wavelengths were chosen with about 75 nm spacing in this spectral region. Relief periodic modulation of Al surface allows for diffraction coupling of far field optical waves to PSPs. On a linear 1D grating this coupling occurs

when an impinging transverse magnetically polarized (TM) wave is phase-matched with PSPs by the grating momentum $2\pi/\Lambda$:

$$\pm Re\{k_{psp}\} = k_o \sin(\theta) + m\frac{2\pi}{\Lambda}, \tag{10}$$

where θ is the angle of incidence of the incident optical beam, $k_o = 2\pi/\lambda$ is the wavenumber of light in vacuum, m is the diffraction order, and k_{psp} is the propagation constant of PSP modes at the Al surface. As illustrated in Figure 4.2(a), the phase- matching occurs at wavelengths where the PSP dispersion relation intersects with that of diffracted light. On Al surface in contact with air (without P3HT: PCBM), normally incident light beam couples to PSPs via the first diffraction order ($m = \pm 1$) at wavelengths λ between 540 and 700 nm when the grating period is tuned between Λ=535 nm and Λ=690 nm. The experimental data in Figure 4.2(b) reveal that on linear 1D Al grating with periods Λ_1=535 nm, Λ_2=612 nm, and Λ_3=690 nm and amplitudes a_1=15.3 nm, a_2=18.5 nm, a_3=14.3 nm a polychromatic normal incident beam simultaneously excites PSPs at three distinct wavelengths of λ=540, 630 and 700 nm. The PSP excitation manifests itself as reflectivity dips at wavelengths that agree with the values predicted by the phase-matching condition (compare with blue-marked intersections in Figure 4.2(a). At these wavelengths, the energy of an impinging optical beam with TM is transferred to PSPs and dissipates due to Ohmic losses in the metal. When increasing the polar angle of incidence θ, each resonance splits into two branches due to the plus and minus first order diffraction coupling ($m = +1$ or -1). The coupling that is associated with the additional spatial frequencies originating from mixing between Λ_1, Λ_2 and Λ_3 is not observed in the wavelength range of 400–850 nm. The reason is that respective periods are either too short (around 300 nm) or too long (several μm) and do not allow fulfilling the required phase-matching condition.

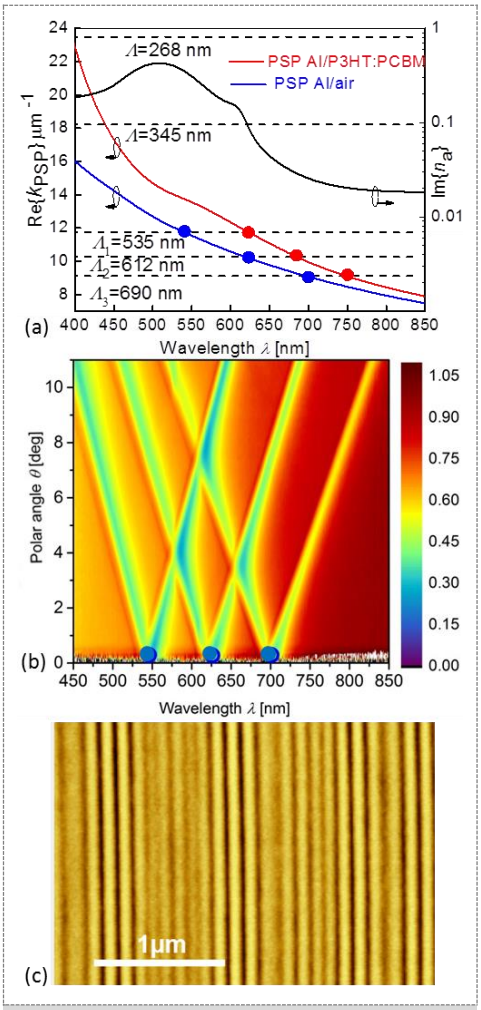

Fig. 4.2: (a) Diffraction phase matching of PSP dispersion relation on Al surface without (blue line) and with (red line) the P3HT:PCBM layer. Polymer layer thickness is of d_a=40 nm. For comparison, the imaginary part of P3HT:PCBM refractive index $Im\{n_a\}$ is shown. (b) Measured dependence of TM specular reflectivity on polar angle θ and wavelength λ for 1D three-diffraction Al grating without P3HT:PCBM layer. The specular reflectivity from the corrugated surface was normalized with that measured on a flat Al surface in contact with air. (c) The AFM image of 1D three-diffraction Al grating. The modulation amplitudes for corrugated surface are a_1=15.3, a_2=18.5, and a_3=14.3 nm and periods Λ_1=535, Λ_2=612, and Λ_3=690 nm. The plane of incidence is defined by x and z axis (with ϕ=0). Images (a) and (b) are adapted with permission from **[179]**

4.1.1.3 Reflectivity measurement of the investigated geometry

After depositing P3HT:PCBM film on a flat Al surface, the reflectivity decreases in the wavelength band between 450 and 600 nm where this polymer blend exhibits strong absorption. The measured data in Figure 4.3(b-d) show that when P3HT:PCBM layer is deposited on a corrugated surface of 1D three-diffraction Al grating, additional three reflectivity dips occur in the NIR part of spectrum besides the absorption band of P3HT:PCBM.

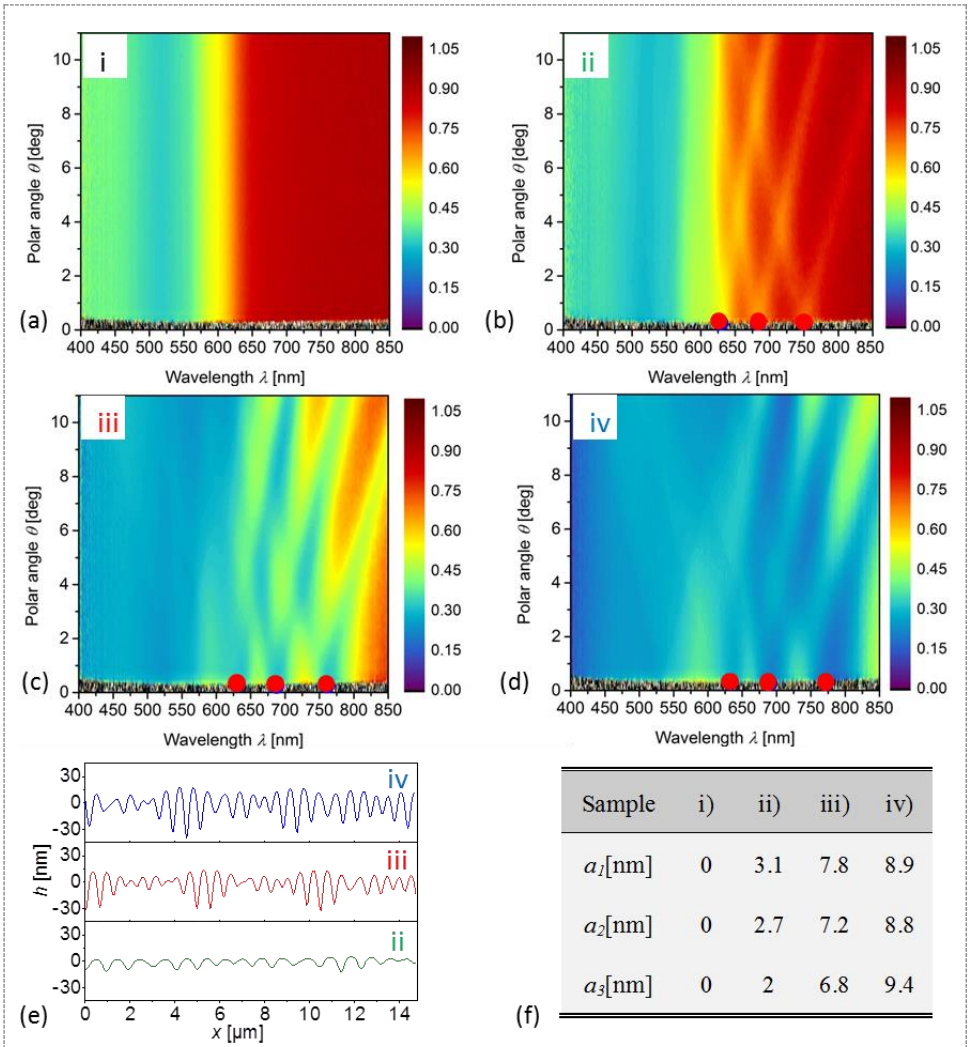

Sample	i)	ii)	iii)	iv)
a_1[nm]	0	3.1	7.8	8.9
a_2[nm]	0	2.7	7.2	8.8
a_3[nm]	0	2	6.8	9.4

Fig. 4.3: (a)-(d) Measured specular TM reflectivity from 1D three-diffractive gratings for increasing modulation depth as showed in (e) respective corrugation profile cross-sections. (f) Overview of determined corrugation amplitudes of modulations at periods Λ_1, Λ_2, and Λ_3. The Al surface was coated with a 35-40 nm thick layer of P3HT:PCBM.The plane of incidence is defined by x and z axis (ϕ=0). Adapted with permission from **[179]**

These dips are associated with the coupling to PSPs at wavelengths that are red shifted with respect to those observed on the Al surface in contact with air. The reason is that the polymer layer exhibits large real part of the refractive index $Re\{n_a\}$ which increases the PSPs propagation constant $Re\{k_{PSP}\}$. The three SPR resonances occur at wavelengths λ=635, 685 and 750 nm which is in the spectral region where P3HT:PCBM exhibits small

imaginary part of refractive index [$Im\{n_a\}$=0.16 at λ=600 nm 0.02 at λ=750 nm was measured by ellipsometry as seen in Figure 4. 2(a)] and thus it only weakly absorbs. One can see that the simultaneous coupling to these three PSPs modes at the Al interface efficiently extends the absorption on the surface in the selected wavelength range λ=600–750 nm. The coupling strength to PSPs can be controlled by tuning the modulation amplitude a at each period Λ. In order to demonstrate this, three samples with amplitudes a_1, a_2, and a_3 between 0 and 10 nm were prepared and coated with Al and P3HT:PCBM polymer layers (see Table in Figure 4.3f). Measured specular reflectivity spectra in Figure 4.3(b-c) reveal that the resonance dips associated to PSP diffraction coupling by Λ_1, Λ_2 and Λ_3 appear for weakly modulated surfaces at wavelengths predicted by the phase-matching condition (compare with Figure 4.2a). For deeper grating presented in Figure 4.3(d), the resonances are slightly red shifted which can be attributed to changes in the propagation constant of k_{PSP} caused by the curved Al interface. In addition, variations in the thickness of P3HT:PCBM layer occur on the stronger corrugated surface leading to a non-conformal geometry (AFM observations showed that the polymer preferably filled the grating valleys leading to the surface with substantially weaker corrugation at the polymer: air interface).

The above discussed data were measured on linear 1D gratings with a light beam that is TM polarized. For such geometry, the orthogonal transverse electrically (TE) polarized light beam does not couple to PSPs and is reflected similar to flat layers shown in Figure 4.3(a). In order to achieve strong broadband plasmonic absorption for both polarizations, a crossed 2D grating with a three-diffraction profile was prepared and coated with Al and P3HT:PCBM layers. Diffraction then occurs via grating momenta in both orthogonal x (indexed with m) and y (index with n) directions and the phase-matching condition can be expressed by using polar θ and azimuthal ϕ angles as

$$Re\{k_{psp}\}^2 = \left[k_o \sin(\theta)\cos(\phi) + m\frac{2\pi}{\Lambda}\right]^2 + \left[k_o \sin(\theta)\sin(\phi) + m\frac{2\pi}{\Lambda}\right]^2. \quad (10)$$

As can be seen in Figure 4.4(a) and 4.4(b), pronounced SPR dips occur both in TM and TE specular reflectivity wavelength spectrum due to the simultaneous diffraction coupling by periods Λ_1, Λ_2, and Λ_3 and orders (m,n)=(±1,0) and (0,±1). For TM polarized light and an azimuthal angle of ϕ=0, SPR dips split when increasing the angle of incidence θ as the coupling occurs via diffraction orders $(\pm 1,0)$ similar as for the 1D linear grating. However, the resonant wavelengths only weakly change with θ for the TE polarized light that couples to via a grating vector perpendicular to the plane of incidence (0, ±1). The wavelength dependence of specular reflectivity R_0 in Figure 4.4(c) compares the spectra measured on flat and corrugated Al surfaces for the polar angle θ=3 deg and azimuthal angle ϕ=0. As the polar angle θ is close to zero, reflectivity curves measured for TM and TE polarization are similar because the structure is symmetrical and thus polarization insensitive at normal incidence. The small difference between TE and TM reflectivity curves can be explained by the effect of resonance splitting due to slightly deviated angle θ. In the wavelength range of 650–750 nm more than 90 percent of light intensity is reflected from P3HT:PCBM layer on the top of a flat Al surface. However, the specular reflectivity R_0 drops to less than 30 percent when the Al interface is corrugated by the developed crossed 2D grating. It should be noted that besides the specular reflection also coupling of the incident light wave to other non-specular waves occurs via propagating diffraction orders below critical wavelengths associated with recorded periods Λ_1, Λ_2, and Λ_3 as well as due to the mixing of spatial frequencies. In order to evaluate this effect, total reflectivity was measured for a fixed angle of incidence

θ=13 degree by using an integration sphere and it was compared to the specular reflectivity at the same angle θ. The data is presented in Figure 4.5. The measured total reflectivity study shows that for long wavelengths > 800 nm the specular reflectivity R_0 and total reflectivity are similar. However, at short wavelengths the diffraction competes with specular reflection and it becomes more pronounced. At wavelength of λ=500 nm around 20 % of light intensity is scattered to propagating diffraction orders on crossed multi-diffractive grating. The above experimental work was supported and confirmed with the finite difference time domain (FDTD) simulations and can be find in the reference [179]. The simulations were performed by Hamid Keshmiri.

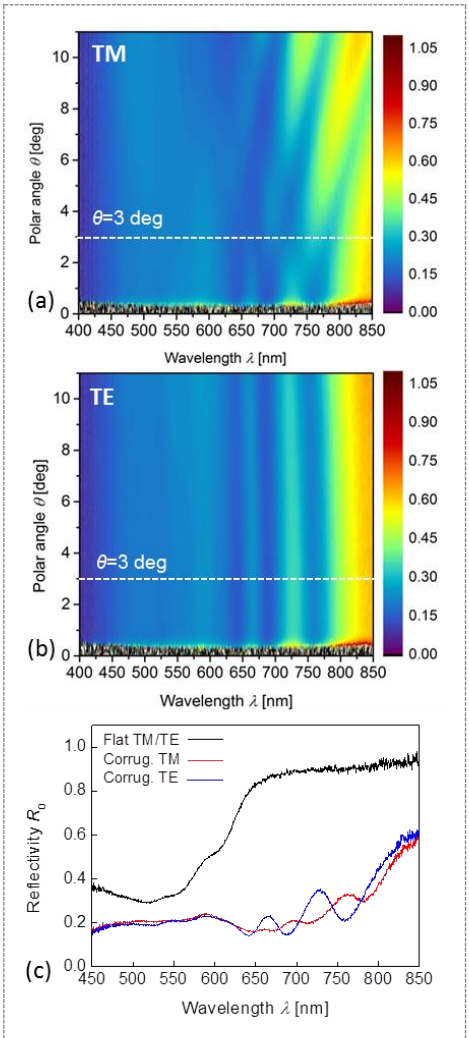

Fig. 4.4: Measured (a) TM and (b) TE specular reflectivity from a 2D (crossed) three-diffractive grating with Al and P3HT:PCBM layers. The profile of the structure is shown in Figure 4.1(b-d). The thickness of Al is 100 nm and thickness of active layer (polymer blend) is d_a=35–40 nm. (c) Cross-section of the specular reflectivity R_0 for a fixed angle of θ=3 deg and azimuthal angle ϕ. Adapted with permission from **[179]**.

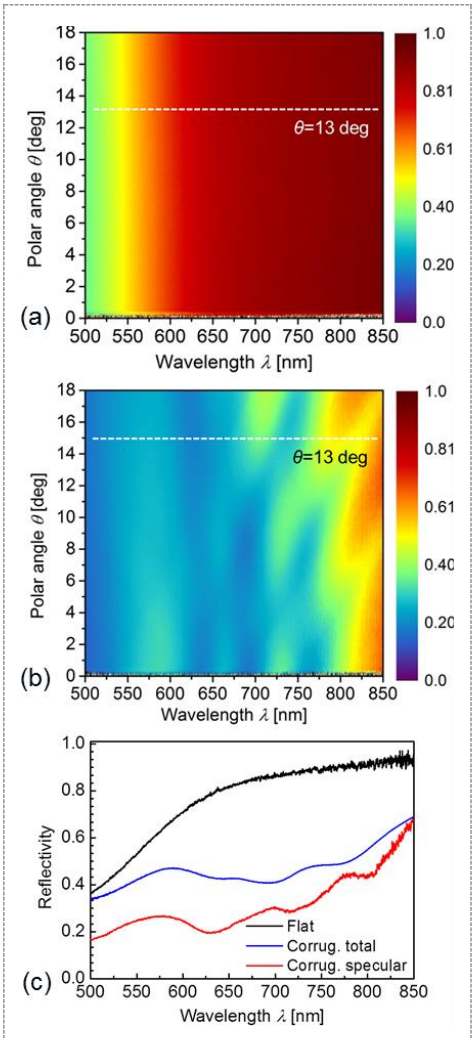

Fig. 4.5: Specular reflectivity measured with unpolarised light from (a) flat Al surface (b) 2D (crossed) three-diffractive Al grating coated with P3HT:PCBM layers and (c) Comparison of wavelength spectra obtained for a fixed angle of incidence θ=13 deg by using a system that measures total reflectivity and specular reflectivity from a flat and corrugated structures. Adapted with permission from **[179]**.

4.1.1.4 Summary

This work demonstrates that multi-diffractive plasmonic structure enhances the absorption in the P3HT:PCBM by a factor of 2.9 in the spectral window 600–750 nm where it is inherently weakly absorbing. Over the whole visible/NIR part of spectrum 400–750 nm the number absorbed photons in P3HT:PCBM is increased by 28 %. Further, let us point out that the chosen geometry demonstrating the enhanced absorption in a thin photoactive layer (d_a=35–40 nm) differs from those used in solar cell devices. In the presented work, we chose a thin absorber layer in order to simplify the analysis of the presented concept as then PSPs are the only guided modes on the surface that can be used for the trapping of light. Thin film OPV solar cells typically rely on absorber layers with thickness d_a=100–200 nm and then the layer structure supports additional waveguide modes. Indeed, the concept of enhancing absorption by multi-diffractive grating can be adopted for these waveguide modes as well and it can offer the advantage of smaller losses associated with the attenuation in metal.

4.2 Dielectric nanostructures for light manipulation

The use of plasmonic nanostructures has the tendency to increase parasitic optical absorption loss due to the metal, which competes with absorption in the photoactive layer of the solar cell device [181, 182]. Therefore we witnessed numerous approaches for optical manipulation of light in field of thin film solar cells, based on dielectric nanostructures [133, 183].

Indium tin oxide (ITO) is the most commonly used material for the preparation of transparent conductive electrodes, can be widely used as an antireflective and transparent electrode layer in OPV. It offers the advantage of high transparency in the visible spectrum of light (typically 85%) and good conducting properties (resistivity in the low 10^{-4} Ω cm regime) [135, 184]. To obtain state-of-the-art optical and electrical properties, ITO films are commonly deposited at high temperature or require high temperature post deposition treatment [105, 124, 139-141, 185-187], which is a handicap for e.g. flexible substrate devices. To this respect, it is highly attractive to improve the ITO properties for ambient temperature deposition.

Numerous approaches to integrate AR or light trapping nanostructures to ITO films have been pursued. A three-dimensional ITO nanohelix array, fabricated using an oblique-angle-deposition technique, was proposed as a multifunctional electrode for bulk heterojunction organic solar cells in order to simultaneously improve light absorption and charge carrier extraction from the active region [143]. Arrays of parabola-shaped subwavelength ITO nanostructures were utilized as AR in silicon-based solar cells, which were prepared by laser interference lithography combined with dry etching and subsequent sputtering processes [142]. Embedded ITO biomimetic nanostructures were used for light trapping and as AR in hydrogenated amorphous silicon solar cells. They were prepared by using polystyrene nanosphere lithography on an index-matching silicon-nitride layer, followed by reactive ion etching [144]. In another report, the ITO electrode layer of an organic LED was textured with one and two dimensional gratings to extract light trapped in waveguide modes and thus enhance the efficiency of the device. The gratings were fabricated by using laser interference lithography and physical plasma etching, followed by a lift off process [188]. ITO nano-rods grown by oblique electron-beam evaporation were demonstrated to provide increased optical transmittance for LED

applications [140]. In another work, ITO nano-rod film grown on a glass substrate using radio frequency magnetron sputtering was reported having sheet resistance and transmittance (at 500 nm) of 90 Ω/square and 85 %, respectively [189]. In a nutshell, the reported nanostructures are complex, requiring multi-step processing and post deposition treatment. Furthermore, most of these works focus on the performance of devices, without detailed information on the optical characteristics of ITO electrode itself [140, 144]. In this work, we report on a facile route to fabricate nanostructured transparent ITO electrodes at room temperature with the improved optical transmission compared to that of the flat films. It is based on a combination of nanoimprint lithography (NIL) and sputtering, without any additional post deposition treatment e.g. complex etching and annealing steps. This approach holds potential for the cost-efficient implementation of AR or light trapping which can be scaled up [138] and find its application, in e.g. emerging field of flexible electronics.

4.2.1 Results and discussion

4.2.1.1 Investigated geometry

The investigated geometry is schematically shown in Figure 4.6 and it consists of a periodic cross grating that is conformally coated with an ITO film. Geometrical parameters of the corrugated surface are studied that would allow its use for two specific purposes. Firstly, to act as a broadband absorber, by suppressing transmittance via the excitation of waveguide modes travelling along the ITO film. Secondly, to work as AR-coating for increasing the transmittance by reducing the reflectance of the incident light intensity at the ITO film interfaces. In particular, the effects of the grating period Λ, the modulation depth MD are assessed.

4.2.1.2 Preparation of nanostructured ITO films

The periodic master structures, later used for the NIL, were prepared by using UV laser interference lithography (LIL) into the positive photoresist. The angle of the interfering beams was set to 54.34°, 32.79°, 23.97° and 18.96° which corresponds to periods of Λ=200, 300, 400 and 500 nm, respectively. In order to record a cross grating structure, the exposure was carried for two orientations of the sample with a rotation angle of 90°.

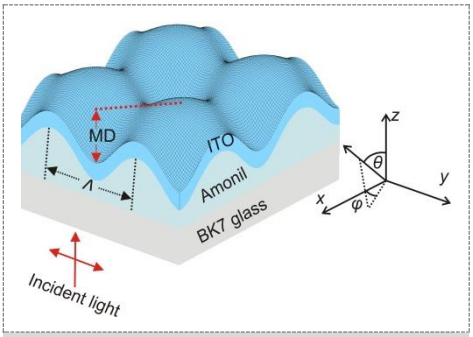

Fig. 4.6: Investigated geometry of nanostructured ITO films. Adapted with permission from **[190]**.

The total exposure dose was 19 mJ cm^{-2}. The exposed samples were developed, and afterwards copied by UV-NIL into 200 nm thick layer of Amonil MMS 10 from AMO Gmbh (Germany) by using protocols mentioned in section 3.1 chapter 3. The obtained cross grating structures were coated with 110 nm of ITO by DC magnetron sputtering (UNIVEX 450C from Leybold Systems, Germany) in pure Ar atmosphere from 4-inch diameter ITO (In2O3:SnO2=90:10 wt. %) target with a purity of 99.9 %. The sputtering was performed at a power of 20 W and 0.2 Pa gas pressure, yielding a sputter rate of 0.086 nm/s. The target to substrate distance was about 10 cm. The sputtering was done with the substrate cooled at 25 °C using a closed-loop water-cooling circuit.

The morphology of the prepared samples was observed with atomic force microscopy from Molecular Imaging (USA). Tapping mode and standard tapping mode AFM tips

PPP-NCHR-50 from NanoAndMore (USA) were used. In addition to AFM imaging, samples were also observed with scanning electron microscopy from Zeiss Microscopy (USA). The morphology of the prepared of samples with periodically corrugated ITO layer can be seen in Figure 4.7, AFM was used to observe the morphology of the structures that exhibited modulation depth of MD=100–120 nm and period Λ=200, 300, 400, and 500 nm. The sheet resistance of ITO films was measured by four point probe method. The sheet resistance of the flat ITO film d_{ITO}=110 nm was of 30±3 Ω/square. The nanostructured ITO films with the same ITO layer thickness presented a slightly increased sheet resistance of to 35±3 Ω/square. These values are quite low, considering the fact that the ITO was deposited without substrate heating and it is worth of noting that the sheet resistance can be further improved by post annealing. Amonil MMS 10 is thermally stable to 150 °C, and its use will not limit its use in the modern next generation of flexible organic photovoltaics and optoelectronics devices.

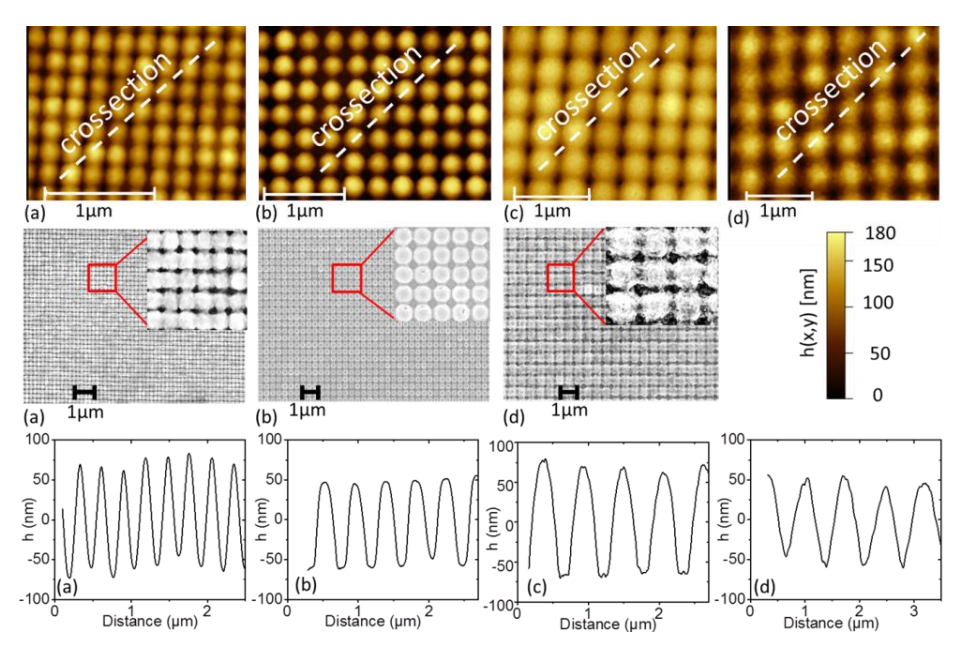

Fig. 4.7: AFM (top and bottom panels) and SEM (middle panels) characterization of nanostructured ITO films with period Λ and modulation depth MD of (a) Λ = 200 nm (MD = 120 nm), (b) Λ = 300 nm (MD = 110 nm), (c) Λ = 400 nm (MD = 120 nm) and (d) Λ = 500 nm (MD = 100 nm). Adapted with permission from **[190]**.

4.2.1.3 Optical properties of nanostructured ITO films

As seen in Figure 4.8 (a), the optical transmittance of the structures with periods Λ=200–500 nm was recorded as a function of wavelength in the spectral window λ=400–900 nm for the normally incident beam θ=0. For the nanostructured sample with a period of Λ=200 nm, the transmission above λ>450 nm is strongly increased and maximum enhancement by 10 % occurs at λ=568 nm. For the sample with longer period Λ=300 nm, the transmission is enhanced at longer wavelengths λ>600 nm similar to the previous sample (maximum enhancement by 10 % is observed at λ=700 nm). At shorter wavelengths around λ~500 nm the transmission decreases by about 50 % due to the first order diffraction coupling to TM_0 and TE_0 waveguide modes. When further increasing the period Λ, the spectral range below which light is trapped at the surface is shifted to longer

wavelength (to λ<650 nm for Λ=400 nm and λ<800 nm for Λ=500 nm). On the other side at longer wavelengths the transmittance is improved and the corrugation serves as antireflection nanostructure. The transmittance decreases owing to the reflection at the interfaces of ITO/air superstrate and Amonil/ITO. The structure-induced continuous change in the effective refractive index through the layer allows suppressing such reflections, which occurs at interfaces with abrupt refractive index changes. This effect can be seen at wavelengths λ, which are above the spectral region where light, couples via diffraction to waveguide modes.

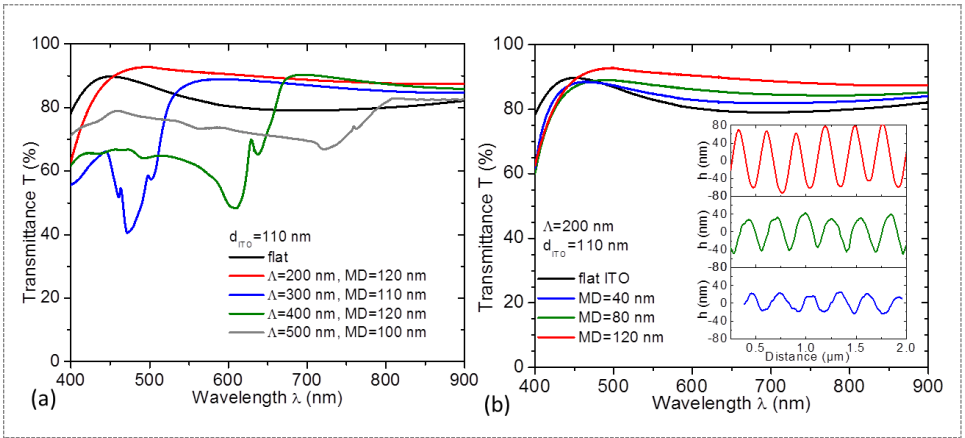

Fig. 4.8: (a) Measured transmission spectra for flat and nanostructured ITO films of thickness 110 nm with periods Λ=200, 300, 400, and 500 nm as indicated in the graph (b) Measured transmission from fixed period at 200 nm, fixed ITO thickness at 100 nm for increasing modulation depth from 0–120 nm. Adapted with permission from **[190]**.

Importantly, the diffraction excitation of the guided wave is angularly sensitive and depends on the azimuthal φ and polar θ angles of the incident light beam [38]. This effect was investigated for the polar angle varied between θ=0 and 22° and the azimuthal angle set to φ~0. On a reference sample with flat ITO layer, the transmittance does not vary when increasing the polar angle θ, see Figure 4.9(a). When tilting the beam hitting the surface of the sample carrying corrugated ITO film with the period Λ=200 nm, the transmittance decreases at a narrow band at λ<450 nm, see Figure 4.9(b). When increasing the period to Λ=250 nm and Λ=300 nm [see Figure 4.9(c) and (d), respectively], this band shifts to longer wavelengths, similar to the normal incident beam (see Figure 4.8). On these samples, the changing of polar angle θ leads to a split of the band to two branches that weakly shift with θ. In addition, there occur two branches with resonant wavelengths linearly increasing and decreasing with θ which forms a characteristic V-shaped feature. The spectral bands that weakly shift with the angle θ are due to the first diffraction order excitation of TM_0 and TE_0 modes travelling in the direction perpendicular to the plane of incidence (marked as $\perp$ in the Figure 4.9). The V-shaped branches are associated to the diffraction coupling to these modes in the direction lying in the incidence plane and splitting to plus first and minus first orders marked as $\parallel$ in the Figure 4.9. Furthermore, as it is crucial to study the performance of nano-photonic structures at high angle of incidence. Therefore the angular response of the samples at high incident angle was measured in range e.g. 0–60 degrees. Similar trend in the diffraction coupling to waveguide modes occurs when increasing polar angle up to 60°, as illustrated by the measurements presented in Figure 4.10(b).

Besides changing the period Λ, the effect of varying modulation depth MD between 0 and 120 nm was studied as shown in figure 4.8(b). The transmittance gradually increases with MD and the highest increase by about 10 % occurs in the red part of spectrum for the period Λ = 200 nm. Let us point out the simulation studies of ITO nanostructures [190] (by Dr. Martin Bauch for this work) predict that higher transmittance can be achieved for deeper structures, however in the herein presented work the modulation depth was limited to MD = 120 nm. The reason is the limitations imposed by the used UV-NIL process, which does not allow reliable imprinting of structures with higher aspect ratio. In addition, the use of high aspect ratio nanostructures deployed to devices may introduce non-uniform electric field strength and eventually deteriorate their electronic performance characteristics [191].

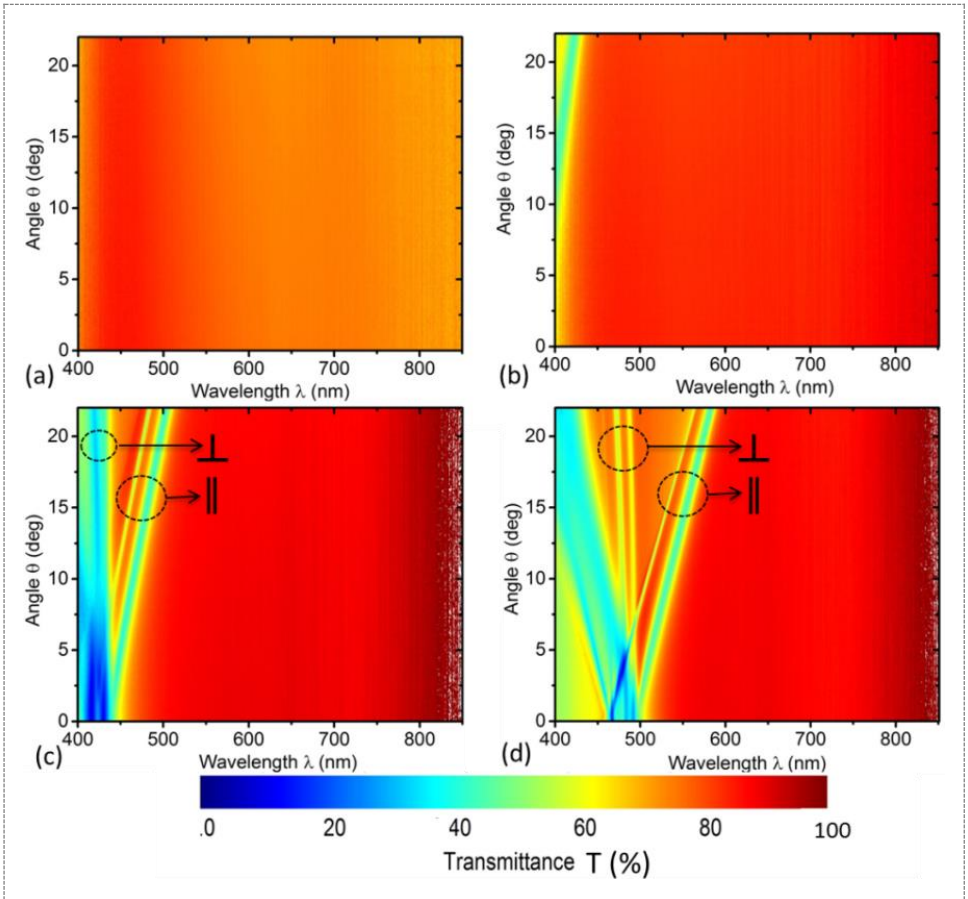

Fig. 4.9: Measured optical transmittance of un-polarized light through 110 nm thick ITO film with (a) flat surface and corrugated interfaces with the period of (b) 200 nm, (c) 250 nm and (d) 300 nm. The modulation depth of corrugated samples was of MD=120 nm. The dependence in wavelength λ and polar angle θ is showed for the azimuthal angle $\varphi \sim 0$. Adapted with permission from **[190]**.

In order to demonstrate the antireflection properties of nanostructures, the reflectance from ITO film with d_{ITO} = 110 nm, period of Λ = 300 nm and modulation depth around MD = 130 nm was measured as a function of wavelength at fixed angle of incidence θ = 13°. The data is shown in Figure 4.10(a) and it shows that the increase in the transmittance is complemented by the decrease in the reflectance and the red part of spectrum is lowered by 12 %.

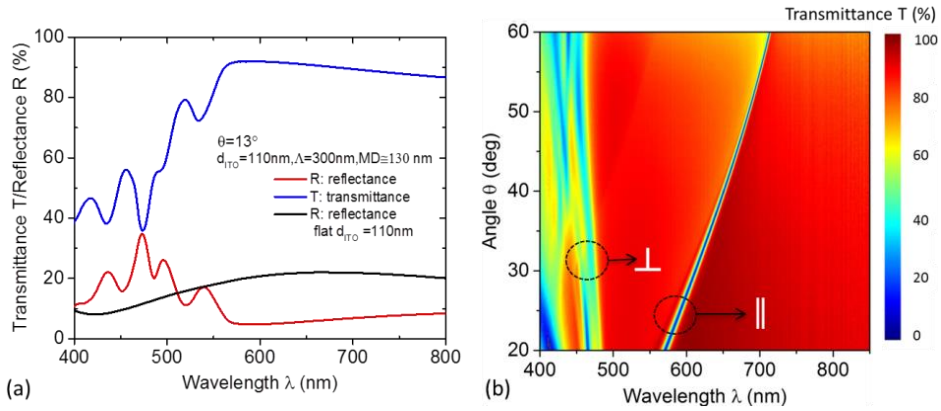

Fig. 4.10: (a) Comparison of reflectance and transmittance spectra at $\theta = 13°$ for flat and nanostructured ITO films with a thickness of $d_{ITO} = 110$ nm, period of $\Lambda = 300$ nm and MD = 130 nm. (b) Measured optical transmittance of un-polarized light through 110 nm thick ITO film have corrugated interfaces with the period of 300 nm. The modulation depth of corrugated samples was of MD=120 nm. The dependence in wavelength λ and polar angle θ is showed for the azimuthal angle $\varphi \sim 0$. Adapted with permission from **[190]**.

4.2.1.3.1 Shape of the waveguide resonance

As seen in Figure 4.8(a) the waveguide resonances are smeared as their spectral width is broader, which can be ascribed to irregularities of the prepared nanostructures and to the divergence of the polychromatic optical beam used in the optical measurements. In the following sections, we investigated the irregularities of the prepared nanostructured and its effects on the shape of the optical waveguide resonances.

(a) Irregularities of the prepared nanostructures

Figure 4.11 illustrates a loss of fidelity upon the replication process by using AFM observation of two samples (named sample 1 and sample 2) with Λ=300 nm. It shows smearing of the nanostructure pattern due to small deviations in the transfer of the motif by using a PDMS stamp (assumedly due to the mechanical moving upon the curing). The variations in the profile of the nanostructured ITO film are seen from three cross section of the height dependence marked as lines (i), (ii) and (iii). The AFM profile analysis shows that sample 1 is smeared and shows broader peaks than sample 2 (deviation less than 20 %). A typical peak height variation is 5 %.

(b) Optical system

Figure 4.12 shows the optical transmittance of the nanostructured ITO films d_{ITO}= 110 nm having periodicity in the nanostructures Λ= 300 nm and modulations depths shown in Figure 4.11. The transmittance was measured with two different optical systems, Bruker Vertex 70 commercial optical system and homemade optical system. The commercial optical system uses a non-collimated beam; the beam was focused to a 1 mm diameter spot size on the sample. The homemade optical system uses a collimated beam; the diameter of the collimated light was reduced to 2 mm spot size on the sample by using an aperture. The schematic presentation of the both systems is shown in Figure 4.12(a-b inset).

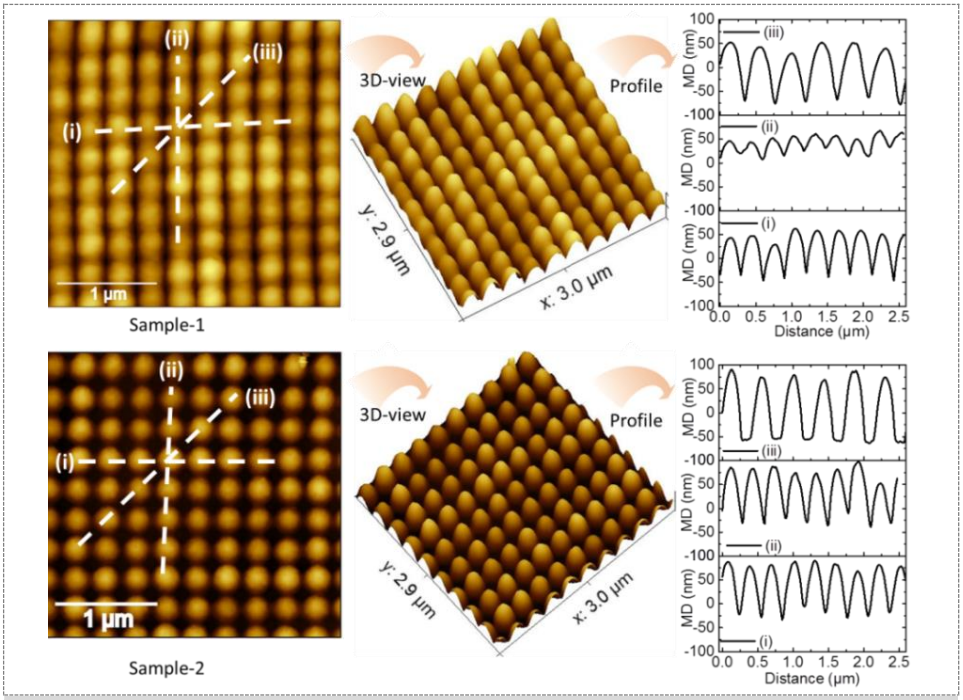

Fig. 4.11: AFM images and profiles of the nanostructured ITO films having period Λ= 300 nm and ITO thickness d_{ITO} =110 nm. Sample-1 shows irregularities in the modulation depths compared to sample-2.

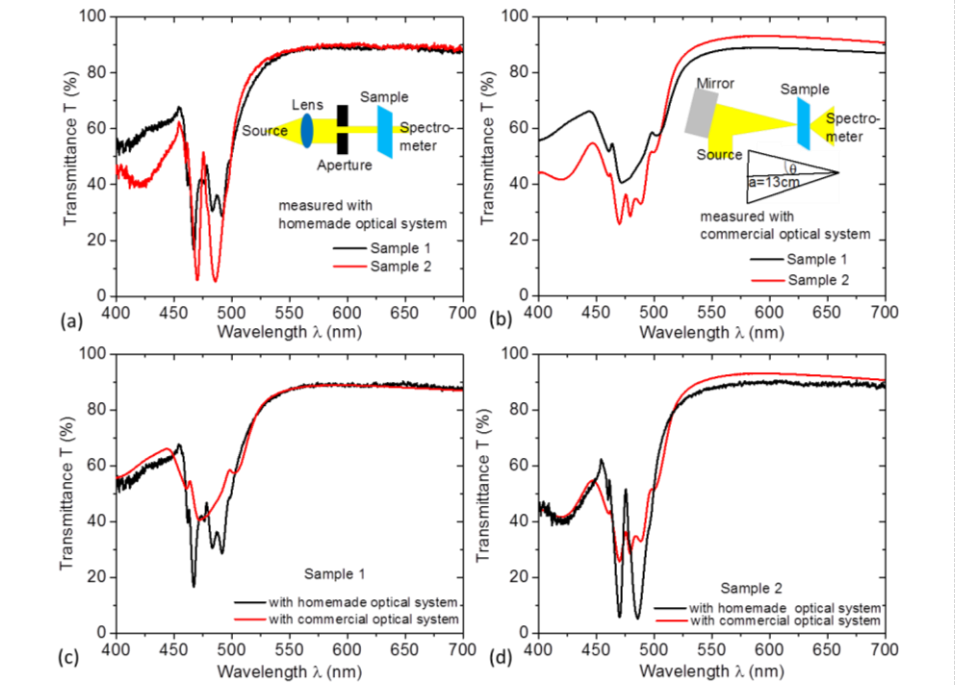

Fig. 4.12: Measured transmission spectra from sample-1 and sample-2 with commercial and homemade optical systems. Both samples have same ITO thickness d_{ITO} = 110 nm, period Λ= 300 nm and modulation depths MD as indicated in the Figure 4.11. Adapted with permission from **[190]**.

4.2.1.4 Optical quality of the prepared nanostructured ITO thin films

The main challenge in the field of nanofabrication is to achieve procedures that ensure controlled nanostructure patterning on large areas and exhibit good optical quality. For

instance in reference [188], it has been proven by optical transmission measurements that the resonant mode has a drift of 0.4 % over the 5 mm length of the ITO grating samples. Therefore, let us discuss the spatial homogeneity of transmittance for the prepared ITO nanostructures samples. The dimension of each substrate was 25 × 25 mm and it contained 15 × 15 mm nanostructured area in its central part; see Figure 4.13(a). Optical transmittance was measured at five spots (area 0.8 mm^2) and over larger area of 78.5 mm^2 for the same sample. As seen in Figure 4.13(b), small variation of around 1 nm (0.2 % $\Delta\lambda/\lambda$) occurs in the spectral position of the resonant coupling to waveguide modes and the transmittance changed by less than 2 % at longer wavelengths. This shows that the nanostructured films produced in this work have excellent homogeneity and optical quality over the entire structured area of the substrate.

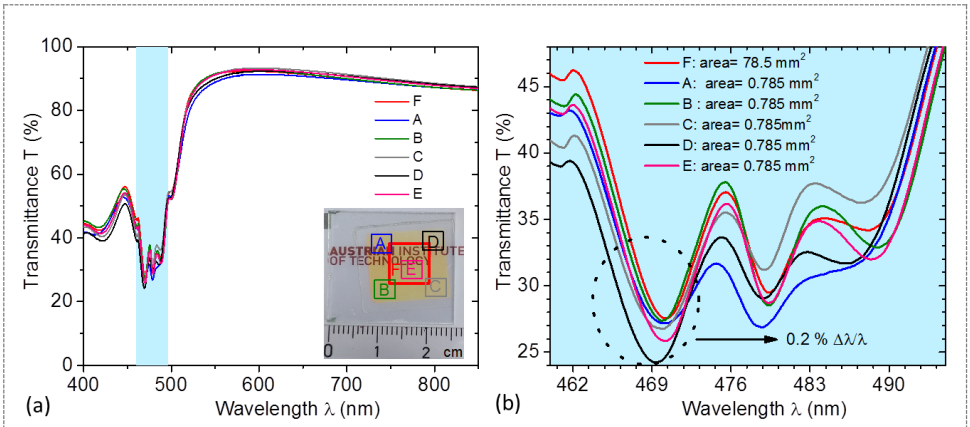

Fig. 4.13: (a) Spatial homogeneity of transmittance for nanostructured ITO films with a thickness of $d_{ITO} = 110$ nm, period of $\Lambda = 300$ nm and MD = 130 nm measured at $\theta = 0$. Inset shows a photograph of the nanostructured ITO sample. The optical transmittance was measured at five spots having an area 0.8 mm^2 and over a larger area of 78.5 mm^2. (b) Small variation of around 1 nm (0.2 % $\Delta\lambda/\Lambda$) in the spectral position of the resonant coupling.

4.2.1.5 Replication of high-aspect-ratio nanostructures

The fidelity of high aspect ratio nanostructure pattern transfer is an important issue in the field of nanofabrication and defects in the transferred pattern could be generated [192, 193]. Figure 4.14(a) shows the master prepared in this work with laser interference lithography, having Λ=200 nm and modulation about MD=250 nm. Such high aspect ratio nanostructure could be prepared easily with proper dose during laser interference lithography exposure process and proper developing time during development process. Making copy replica from such subwavelength nanostructures with nanoimprint lithography technique as schematically shown in 4.14(b) becomes difficult by using the soft PDMS stamp. The nanostructure either completely collapsed as shown in Figure 4.14(d) or shows high irregularities in MD or period as shown in Figure 4.14(c). This happens during the nanoimprint lithography process illustrated in Figure 4.14(b), either making the PDMS stamp from master [curing parameters, which include curing times at different temperatures, ratio of the polymer for hardening and low Young's modulus (~1.8 MPa)] or making replica from PDMS stamp (pressing parameters: which include imprint force and mechanical movements of surfaces during PDMS stamp and sample pressing step). Due to these limitation, in this work we had control for nanostructure having Λ=200 nm and MD in range 20–120 nm.

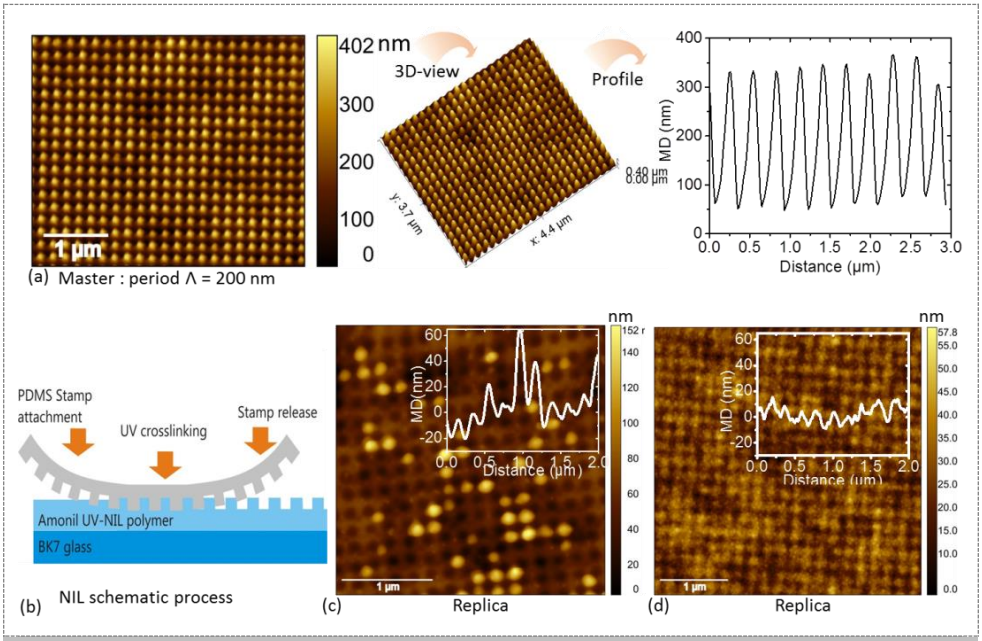

Fig. 4.14: (a) AFM image and profile of master prepared with LIL having period 200 nm and MD above 250 nm (b) schematic of NIL process used for the fabrication of replica (c) high irregularities in the nanostructures occurred during NIL process and (d) nanostructures collapsed during NIL process. Adapted with permission from **[190]**.

4.2.1.6 Summary

This work shows that the dense cross gratings of the corrugated and conformal ITO enhance the light transmission in the 450–850 nm range by 8% (absolute) compared to flat ITO films. This is one of the largest performance improvements reported in the literature for nanostructured transparent electrodes. While increasing the grating period shifts the threshold for diffraction-coupling to waveguide modes in the visible and near-infrared part of spectrum, resulting in broad light trapping behaviour at wavelengths below this threshold. This work demonstrates a simple processing route at ambient temperature for the fabrication of high-performance transparent electrodes in order to fulfil different device requirements. Furthermore, the experiments were supported by numerical simulations and can be find in the reference [190]. The simulations were performed by Dr. Martin Bauch.

4.3 Metal nanowires

Metal nanowires (NWs) have attracted a great deal of interest during the last decade because of their unique electronic and optical properties along with their applications in thin films solar cells, sensors, organic light-emitting diodes (OLEDs), liquid-crystal displays (LCDs). The research on metal NWs focuses on the following main three purposes:

(i) Replacement of transparent conductive oxides

Transparent electrodes (TEs) are an inevitable component, which play a pivotal role in a variety of modern devices such as touch screens; LCDs, OLEDs and thin film solar cells. Traditionally, this role has been well served by state-of-the-art large bandgap semiconductors doped with metal, known as transparent conductive oxides (TCOs) [194]. Among the TCOs, indium tin oxide (ITO), aluminium-doped zinc oxide and fluorine-

doped tin oxide is commonly used as TEs in optoelectronic devices owing to its low sheet resistance transmittance over the whole visible range and suitable work function [135]. In recent years various concepts have been investigated for the replacements of ITO. Among them, transparent metallic electrodes based on nano-pattern plasmonic metals (Ag, Au, Cu and Al) have attracted a lot of attention due to their unique optoelectronic properties. Due to recent advances in nanoscale fabrication techniques the nano-patterning of the metallic films provide viable alternative to TCOs as transparent electrode. In an effort to replace TCOs, metal NWs were recently investigated, because the conductive electrode based on metallic nanostructures could potentially lead to the development of low cost and high performance large area transparent electrodes. For example, Ag NWs functioning as transparent electrode to replace ITO electrode in thin film solar cells was successfully demonstrated [70, 146, 151]. Similarly, in another work, 40 nm thick Au periodic lines as TEs were demonstrated for OLED applications [195].

(ii) Light manipulation

The nano-patterned metal based transparent electrodes (NPMTEs) provide opportunities to manipulate photons and electrons that are not possible for flat transparent electrodes. The light manipulation (scattering and coupling) in NPMTEs provides additional benefits for device applications, particularly for thin film photovoltaics solar cells where light scattering enhances the light absorption in the active layer. For example, periodic Ag nanowires with a line width of 55 nm were successfully employed as transparent electrodes and for light manipulation purposes in organic solar cells. A 35% overall increase in *PCE* of the device due to surface plasmon enhanced photocurrent was observed [146]. In another work, a nanoscale dense Cu mesh structure was replicated by using a high modulus PDMS stamp. The author shows that the transmittance is increased by reducing the linewidth of the mesh pattern and an average transmittance of 75% was achieved [196].

(iii) Enhancing electrical conductivity of TCO

Despite its brittleness [197], ITO is widely used as transparent electrode material due to its relatively high conductivity and transparency, which leads to high performance in lab-scale devices [135]. As mentioned in section 4.2, the state-of-the-art ITO films are commonly obtained by annealing at high temperature (>300 °C) during or after the deposition process to achieve high conductive films, which is a handicap for e.g. flexible substrate devices. To this respect, it is highly attractive to improve the ITO conductive properties for ambient temperature. Several investigations on decreasing the sheet resistance of ITO electrodes without losing a significant part of their optical transmittance have been made. For example introducing an ultrathin metal layer or thin metallic grids or NWs on top or in between layers of ITO, reduces the sheet resistance of ITO remarkably [147, 198, 199].

In order to achieve all the above three purposes, one common model structure is a periodic nano-line (1D-nanogratings) or nano-wire or metallic nanogrid (2D) which has been extensively studied and has long been the focus of intensive research [148, 149, 151, 152]. The fabrication of such structures has typically been carried out using focused ion beam milling or electron-beam lithography techniques that are relatively expensive and time consuming.

In this work, we report the fabrication of multi-periodic nanowires by UV laser interference lithography combined with dry etching. Our methodology is versatile which can be used to fabricate NWs of any metal that may be deposited through standard evaporation processes, could be produced through nanoimprint lithography. Our multi-

periodic NWs offers several unique advantages like the wavelength, number and intensity of resonances can be tailored, can work as broadband plasmonic absorber and reduce the sheet resistance of the ITO films.

4.3.1 Results

4.3.1.1 Investigated geometry

The investigated geometry of multi-periodic NWs is shown in Figure 4.15. The geometry consists of multi-periodic Au NWs, conformally coated with an ITO film d_{ITO}=110 nm. This geometry was designed to act as plasmonic transparent electrode and achieve two purposes. Firstly, to act as broadband absorber via the excitation of waveguide modes travelling along the ITO film and excitation of localized surface plasmons. Secondly, to reduce the sheet resistance of the ITO film.

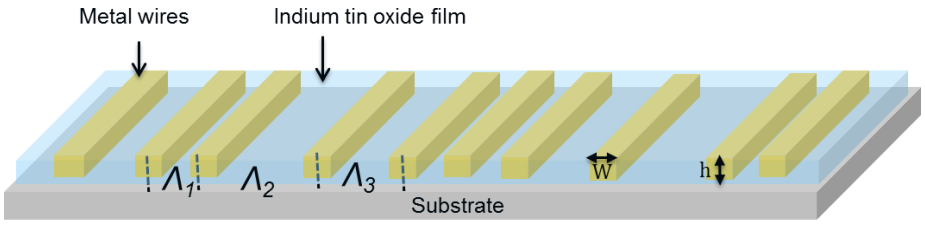

Fig. 4.15: Investigated geometry of a multi-periodic Au NWs with periods Λ_1, Λ_2 and Λ_3 on glass substrate, coated with ITO layer. The width is denoted by w and height by h.

4.3.1.2 Preparation of nanowires

A 5 nm thick ITO (as adhesion layer) and a 50 nm thick gold layer were sequentially sputtered on clean glass microscope slides (20x20 mm). Glass substrates were then spin-coated at 4500 rpm for 45 s with Microposit S1805 G2 positive photoresist diluted (1:2) with propylene glycol monomethyl ether acetate, originating a 100 nm thick film. Afterward, substrates were soft-baked at 98 °C on a hot plate for 120 s. The multi-periodic NWs design was prepared by sequential LIL recording of a periodic sinusoidal interference pattern with varied period Λ into a photoresist layer. After exposure, substrates were immersed in a diluted AZ 303 developer solution with distilled water at a ratio 1:15. Directional dry etching with an argon milling system (Roth & Rau IonSys 500) was carried out to transfer the multi-periodic NWs pattern into the underlying gold layer (etching time 450 seconds, 70 degrees). Finally, the remaining resist was removed by oxygen plasma using parameters, 5 minutes process time, 1 mbar pressure and 40 W power.

4.3.1.3 Bi-periodic gold nanowires

Figure 4.16 shows an example of Au NWs having two periods Λ_1 = 400 and Λ_2 =550 nm. The width w of the Au NWs is in the range of 110-115 nm and height h= 50 nm. The optical transmittance was recorded as function of wavelength in the spectral window λ=380–1050 nm for normally incident beam [with the Au NWs at the front (incident) side] using Bruker Vertex 70 Fourier transform infrared spectrometer. The measured transmission spectra (blue curve-Figure 4.16) shows around 60 % transmittance in the spectral window range λ=400–700 nm and above 70 % in the range λ=800–1050 nm.

Further, a transmission valley can be seen in the spectra as well, which is attributed to the excitation of localized surface plasmon resonance (LSPR). In order to see the light trapping properties of this prepared Au NWs samples, 110 nm thick ITO was sputtered on the top of NWs and optical transmittance was recorded. The measured transmission spectra (red curve in Figure-4.16) shows reduction of transmittance compared to flat 110 nm ITO film (black-curve). The observed dips in measured transmission spectra are attributed with the excitation of LSPRs and to the diffractive coupling of light to dielectric waveguide modes in the ITO film.

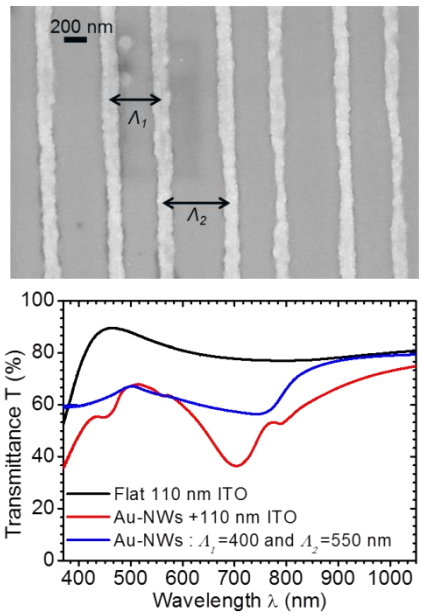

Fig. 4.16: SEM characterization of Au NWs with periods Λ_1 = 400 and Λ_2 =550 nm, width w=110–115 nm and height h=50 nm. The measured transmittance for Au NWs, flat ITO and NWs coated with 110 nm ITO film is shown as well.

4.3.1.4 Multi-periodic gold nanowires

Similarly two samples (namely sample 1 and sample 2) of Au NWs were prepared having three periods. Sample 1 having periods Λ_1 = 250, Λ_2 =300 and Λ_3 = 375 nm, w in the range of 150–200 nm and h=50 nm. Sample 2 having periods Λ_1 = 400, Λ_2 =600 and Λ_3 = 700 nm, w in the range of 100-120 nm and h=50 nm. The transmittance measurement of both sample 1 and sample 2 are shown in Figure 4.17 (blue curves). The measurements show that the optical transmittance of sample 2 is much higher than samples 1 and its transparency comparable to the flat 110 nm ITO film. The transmission of sample 1 near the resonant wavelength~ 600 nm and overall as well, is lower due to the higher density Au NWs and its widths. Both samples were coated with 110 nm ITO film, and the optical transmittance was recorded. These measurements, graphed in Figure 4.17 (red curves), show that transmittance is reduced and additional dips appears. These additional tips can be attributed to the diffractive coupling of light to dielectric waveguide modes in the ITO film, which were discussed in details in section 4.2.

Finally, let us comment on the electrical properties of investigated geometry, which were assessed by measuring sheet resistance with four point probe method. The average sheet resistance of the 110 nm thick ITO film was 30±3 Ω/square. The Au NWs sample having Λ_1 = 400 and Λ_2 =550 nm reduce the sheet resistance of ITO film from 30±3 Ω/square to 20 Ω/square. The Au NWs sample having Λ_1 = 400, Λ_2 =600 and Λ_3 = 700 nm reduced the sheet resistance of ITO film from 30±3 Ω/square to 17 Ω/square. The Au NWs sample having Λ_1 = 250, Λ_2 =300 and Λ_3 = 375 nm reduced the sheet resistance of ITO film from 30 Ω/square to 13 Ω/square.

In summary the trade-off between optical transmittance and low sheet resistance on different Au NWs array geometry embedded in ITO film was explored. Increasing the periods of the Au NWs and decreasing the widths of the Au NWs leads to high optical transmission and higher sheet resistance values. While reducing the periods of Au NWs

and increasing widths reduce the optical transparency but yields lower sheet resistance values.

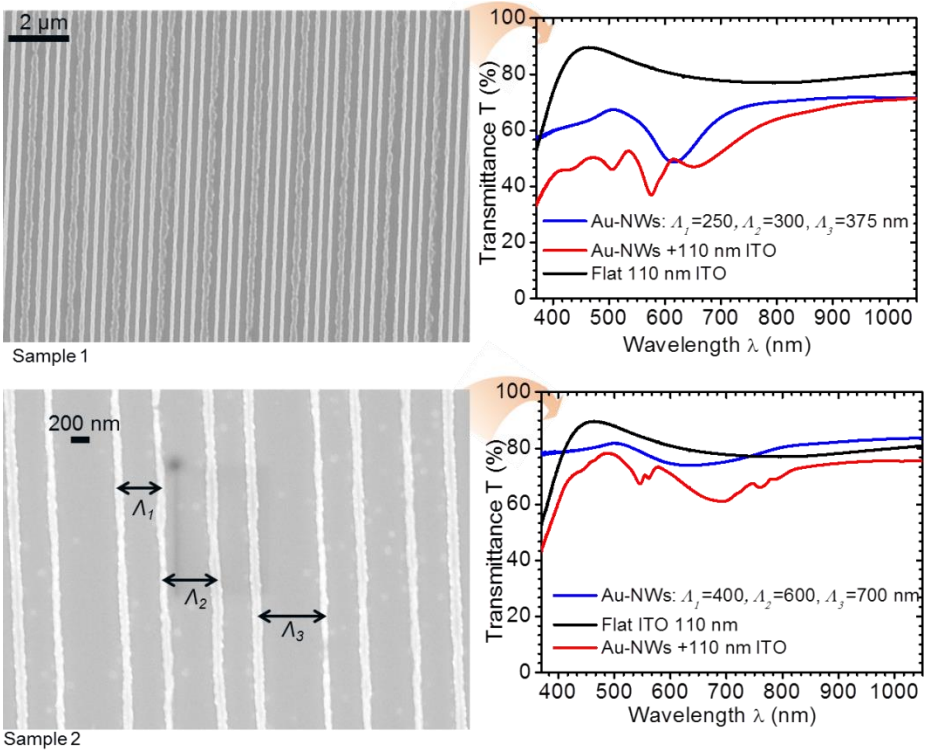

Fig. 4.17: SEM characterization of sample1 and sample 2. Sample 1: Au NWs with periods $\Lambda_1 = 250$, $\Lambda_2 = 300$ and $\Lambda_3 = 375$ nm, width w=150–200 nm and height h=50 nm. Sample 2: periods $\Lambda_1 = 400$, $\Lambda_2 = 600$ and $\Lambda_3 = 700$ nm, width w=100–120 nm and height h=50 nm. The measured transmittance for both samples (Au NWs), flat ITO and NWs coated with 110 nm ITO film is shown as well.

4.4 Collaborative projects

The established methods for preparation of plasmonic nanostructures were exploited outside of the OPV device through collaboration projects in the field of biosensor. Biosensors are under intensive development worldwide because they have many potential application e.g. in the field of clinical diagnostics, food analysis, environmental monitoring and process control of industrial process [200-202].

A Biosensor is an analytical device that transforms biochemical information into useful electrical signals and provides fast, portable and cost-effective analysis. The general structure of a biosensor comprise of main three parts, a recognition system, a detector and a transducer [200, 203]. This is schematically shown is Figure 4.18. The recognition system of a biosensor is a biological recognition element or bio-receptor generally consists of an immobilized bio-component that is able to detect the specific target analyte (molecular species, we wish to identify and quantify) [200, 204]. These bio-components are mainly composed of proteins, antibodies, nucleic acids, enzyme, animal/plant cells and etc. The transducer element of biosensor is a converter, which has an important role in the signal detection process. It converts a wide range of physical, chemical or

biological effects (produced due to the reaction between the analyte and bio-receptor) into an electrical signal with high sensitivity and minimum disturbance to the measured [195, 200].

Normally, biosensors are categorized according to the transduction method e.g. electrochemical, piezoelectric, calorimetric and optical. The detector system measures the properties such as optical and offer high sensitivity to small changes. The optical method of transduction had made rapid advances over the past decades and has been employed in many classes of biosensor. The reason behind is there exist many different types of spectroscopy, for example absorption, fluorescence, phosphorescence, surface enhanced Raman scattering (SERS) and dispersion spectroscopy [205]. The optical biosensors based on surface plasmons resonance or fluorescence (integrated with optical fibre) is the most popular method for biosensing and it has momentous progress to other biosensing approaches due to its rapid and high sensitive response [201, 202, 206, 207]. The optical based biosensor using two detection protocols, label-free and labelled. The most widely used label-free optical biosensor is the SPR sensor and has become an established technology for biomolecular interaction analysis and for detection of chemical and biological species [208]. In label-free detection protocol, the SPR change their optical resonance wavelength (shift in the SPR dip) when an analyte binds to the surface (biomolecular interaction) and thus a change in refractive index around the metal interface occurs. The shift in the SPR dip can be precisely monitored and information on the binding events (biomolecular interaction) can be gathered [209].

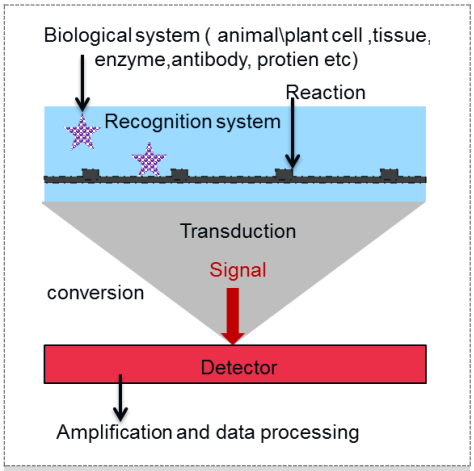

Fig. 4.18: Schematic showing the principal of a biosensor.

4.4.1 Project-I: Smartphone biosensor

For early diagnosis, domestic healthcare and environmental monitoring in remote locations, on-site detection of chemical and biological species is of paramount importance and interest [210]. For example, in remote locations conventional analytical tools are not available. Further, the conventional analysis in a clinical setting usually requires highly-trained personnel, sophisticated instruments and state-of-the-art procedures and protocols e.g. examinations (X-ray, tomographic and ultrasonic imaging, etc.), lab-tests (mass spectroscopy, electrochemical assay and enzyme-linked immunosorbent assay [ELISA] etc.) [211]. Indeed the conventional methods provide high sensitivity; however they are not suitable for on-site analysis. The conventional methods are time consuming, not usable for daily life, and often not affordable for deploying in resource-limited areas. In this context, multiple strategies have been proposed to address the technical challenges in the area of point-of-care (POC) and field diagnosis based on optical/electrical components [212]. For example, the POC systems such as paper-based devices for HIV detection [213] and colorimetric immunoassays have been proposed [214]. Although these simple colorimetric assays can be read by the naked eye, more sensitive and precise analysis requires amplification, image capturing and data processing. Among the external auxiliary tools, the smartphones are gradually standing out because of the global ubiquity,

steady upgrading functions and straightforward coupling with optical methods that utilize absorbance/transmittance, fluorescence, chemiluminescence and spectroscopy of guided waves based on photonic crystal and surface plasmon resonance [215-219]. Such developments may provide new solutions for routine daily personal healthcare and tests of contaminants in drinking water and food. It can also serve as a first hand tool for the characterization of injectable biofluids prior to use. Critical reviews on the smartphone biosensors based on optical and electrical detection methods have been reported elsewhere [220].

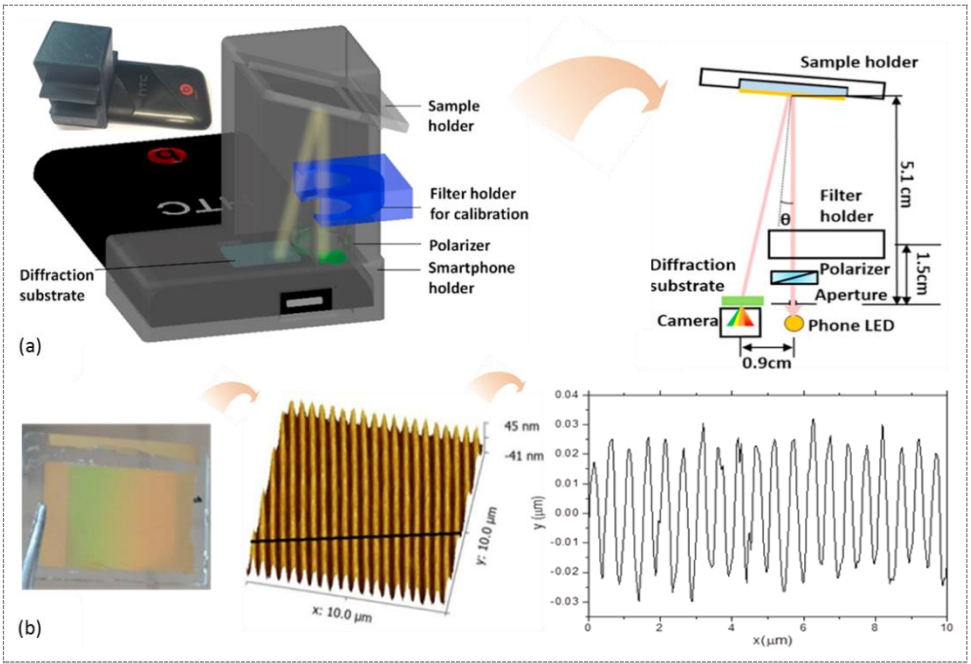

Fig. 4. 19: The top panel (a) Schematic structure of the smartphone spectrometer relying the in-built LED light, a CD diffraction substrate and the smartphone camera. Inset is a photo of 3D printing plastic sample chamber kit attached on HTC sensation XE smartphone. The optical arrangement of the smartphone spectrometer. The bottom panel (b) a photo of an Au sensor chip with diffraction grating, a corresponding AFM image and surface profile of the sensor chip. Adapted with permission from **[221]**.

Lipopolysaccharide (LPS) also known as endotoxin [222] is one of such targets present in the outer membrane of Gram-negative bacteria. It consists of three covalently bound parts, an inner core, outer core and O-antigen. LPS is an inflammatory stimulator that may trigger septic shock. Septic shock is severe pathophysiological syndrome in response to an infection that in many cases is fatal as it can lead to organ failure [223]. Human beings are exposed to LPS through drinking water and injectable biofluids (including various supplements and infusion liquids). The first detection method for LPS, rabbit pyrogen test (RPT) dates back to 1940s [224]. Other approaches have been established since then including the widely used limulus amoebocyte lysate (LAL) test [225]. Apart from these complicated methods, some of which involved animals, methods that are fully synthetic and are easy to operate are in great demand.

In this project we demonstrate a portable LPS detection platform based on a smartphone and a grating-coupled SPR (GC-SPR), as shown in Figure 4.19(a). Compared to previous designs of portable biosensors that utilize wavelength interrogation of GC-SPR and immunoassays [226], the reported sensor system does not require additionally external

light source and detector which greatly simplifies the whole platform. In addition, specific analysis of target analyte is assured by using a synthetic peptide receptor immobilized on the sensor chip surface which provides more robust disposable sensor chips with longer shelf-life.

4.4.1.1 Sensor chip preparation

The linear grating master was prepared by the LIL with Lloyd's mirror configuration into the positive photoresist, as explained in the previous chapters (Chapter-3 and 4). The angle of the interfering beams was set to 18.96° which corresponds to periods of Λ=500 nm. After words copies were made from master by using UV-NIL. A clean glass substrate was spin coated with UV curable polymer (AMONIL-MMS10) having thickness 120 nm and a PDMS stamp (replicated from master) was placed on it. Then it was subjected to curing step under UV light (wavelength 365 nm) for 5 minutes. After peeling off the PDMS stamp, the substrate was coated with 2 nm Cr followed by 70 nm Au film. The Au grating substrates can be mass produced with the PDMS stamp and UV curing procedure, which is also compatible with roll-to-roll printing. AFM characterization indicated the sinusoidal modulation with period of Λ = 500 nm and modulation depth of MD = 50 nm as shown in Figure 4.19(b). The gratings Au substrate was analysed by a commercial spectrometer Ocean Optics HR4000 for angles of incidence 0–30° by using our home made optical angular reflectivity system explained in section 3.3. During the measurement the gratings oriented perpendicular to the plane of incidence. The data is shown in Figure 4.20(a-b). The GC-SPR associated with the coupling of incident light to surface plasmons via diffraction coupling is manifested as a narrow dip in the reflectivity spectrum. The measured reflectivity spectrum shows that the resonance occurs at normal incidence at around 550 nm. When the angle of incidence is increased, the resonance splits into two branches due to the plus and minus first order diffraction coupling (m = +1 or −1). The −1st diffraction order branch is red shifted. The −1st order resonant wavelength increases linearly from about 570–730 nm with the incident angle increase from 4° to 25°, as shown in Figure 4.20(a). The coupling to surface plasmons is stronger and the resonant dip is narrower (width of 20–50 nm) for the −1st diffraction order than for the +1st diffraction order. The reason is that the +1st diffraction order SPR occurs at short wavelengths close to the plasma frequency of gold. The prepared Au gratings substrates were handed were to our collaborators, and were subjected to a cleaning step by O_2 plasma for 3 min. After 4h incubation in aqueous solution with 50 µM KC-13, the surface was rinsed by distilled water and dried by a stream of N_2. The peptide forms covalent interaction between the Au and thiol terminated group from the cysteine of the

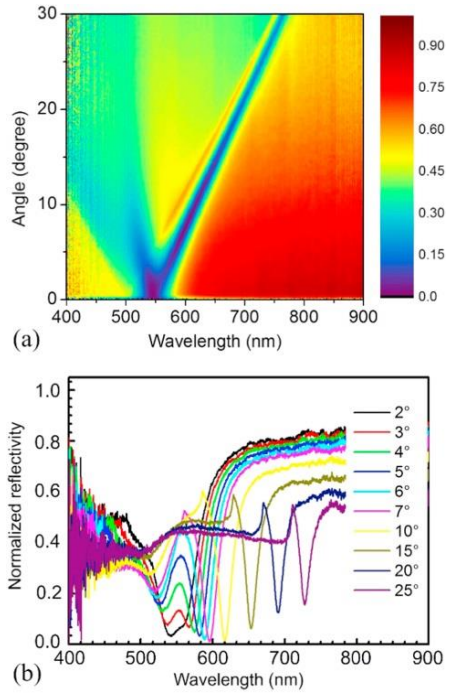

Fig. 4.20: (a) Measured angular-reflectance dispersion of grating Au substrates under incident angles from 0° to 30° (step of 0.1°) and wavelength range between 400 nm and 900 nm. (b) Reflective spectra of grating Au substrates measured under 10 different incident angles in air. Adapted with permission from **[221]**.

peptide. The peptide-modified Au substrates were used further for LPS detection, the summary is presented in the following section.

4.4.1.2 Summary

Linear gratings having period 500 nm and modulation depth around 50 nm prepared in this work were used to build a grating-coupled SPR smartphone spectrometer. It was applied for the detection of lipopolysaccharides. This optical instrument does not contain electronic components and solely relies on the LED flash light source and the CMOS camera built in the used smartphone. The spectrometer is able to perform the analysis in a spectral range of 430–650 nm and it was employed for SPR spectroscopy on sensor chips with Au diffraction gratings that are be prepared by mass production-compatible means. As a receptor, synthetic peptide KC-13 ligand was immobilized on the Au grating sensor chip for specific capture of lipopolysaccharides. The measurement was performed ex situ based on monitoring the resonant wavelength shift. The results show the feasibility for the detection of lipopolysaccharides at detection limit of 32.5 ng/mL, and good selectivity for the lipopolysaccharides detection with practical application for real samples/matrices detection such as clinical injectable fluids [221].

4.4.2 Project-II: UV -surface plasmon resonance biosensor

The majority of SPR biosensors utilize sensor chips with gold films or gold nanoparticles in order to probe the captured target analyte with the confined surface plasmon field at wavelengths in the green, red or near infrared part of spectrum. The use of silver instead of gold offers the advantage of lower ohmic losses and possible SPR probing at lower wavelengths in the blue part of the spectrum [227]. In recent years, aluminium becomes increasingly explored for SPR sensing at even lower wavelengths in UV part of spectrum [228]. It is worth of noting that surface plasmon excitation at aluminium occurs at wavelength as low as 200 nm [229]. In contact with air, a native oxide layer is formed on the top of aluminium films, which provides similar chemical inertness as gold. The thickness of this layer is mostly reported as 2-3 nm [228], which is much smaller than the penetration depth of surface plasmons and does not prevent its utilization for sensing [230]. The oxide passivation layer enables functionalization by using silane linkers instead of thiols that are most often used for gold. The probing with surface plasmons at UV wavelengths in aqueous environment holds potential for increasing detection sensitivity of direct SPR biosensors and it offers means for the implementation of plasmon-enhanced fluorescence [230-232] for several analytes that exhibit inherent absorption in this wavelength range. These include DNA, proteins (absorption bands at 200–280 nm), various odorant binders [233], and e.g. aflatoxins [229]. However, the probing of the aluminium sensor surface with light at UV wavelengths imposes several challenges. The increasing absorptivity of the high refractive index optical glasses in the UV requires usage of fused silica [234]. Therefore, the commonly used attenuated total internal reflection method with a prism made of such low refractive index glass does not allow reaching the high momentum of the incident light needed for the phase matching with surface plasmons. Thus, the resonant excitation of surface plasmons on aluminium surfaces allowed the probing only ex situ on dry sensor chips, while in situ measurements of kinetics of surface reactions in contact with water were not reported.

In order to overcome the above-mentioned restrictions, the using of aluminium grating-coupled SPR sensor is reported for the in situ observation of proteins at UV wavelength of 280 nm in an aqueous environment. According to our knowledge, wavelength

interrogation of SPR is utilized for the first time for the observation of molecular binding events in aqueous environment in this wavelength range, which is not possible for the more commonly used Kretschmann-Raether geometry [106]. As model analyte, the odorant-binding protein 14 (OBP14) of the honeybee (Apismellifera) is used [235], which might be of interest for odorant binding analyses with recently developed artificial fluorescent odorant analogues that absorb in the UV-range [236].

4.4.2.1 Sensor chip preparation

Crossed grating nanostructures were prepared with LIL and NIL standard protocols used in the previous sections for UV-surface plasmon resonance biosensor. Briefly, a 400 nm thick layer of positive photoresist (S1805) was deposited on BK7 glass substrates.

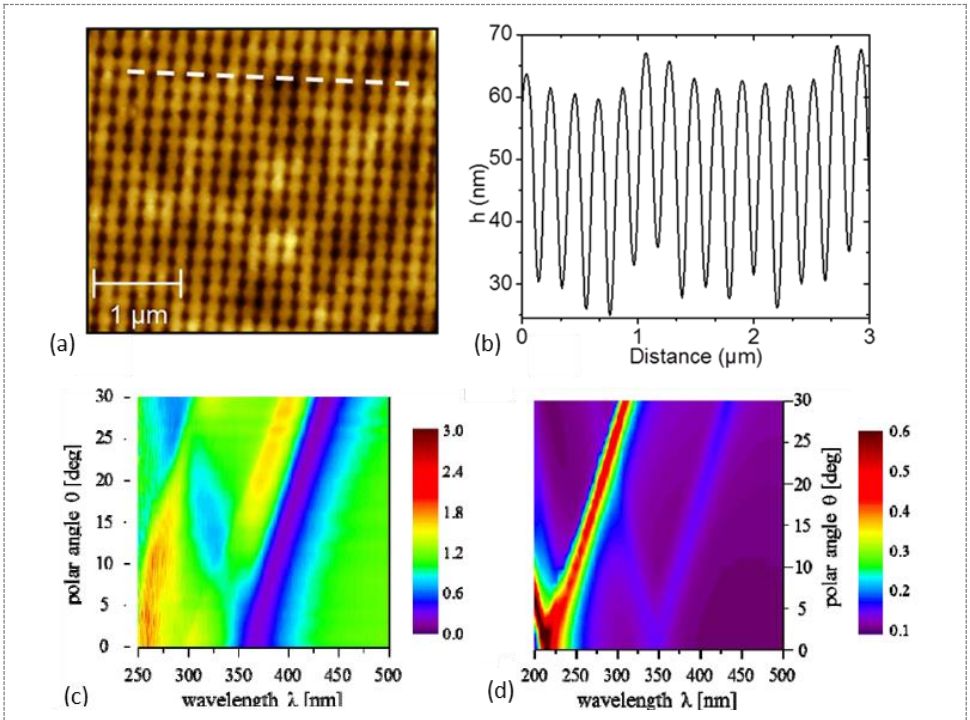

Fig. 4.21: Characterization of a crossed Al grating by (a) AFM and (b) profile cross-section. Angle–wavelength dependence of transmission for Al gratings in contact with air (c) measured and (d) simulation. Image (c) and (d) are adapted with permission from **[237]**.

These substrates were exposed to the interference field with the intensity of 32 µW/cm^2 at an angle of 54.34 deg, which, corresponds to a grating period of Λ=200 nm. The exposure was carried out twice for two orientations of the sample with a rotation angle of 90 deg. The exposed samples were developed and then replicas of the relief LIL grating were prepared on the top of UV-transparent on cleaned fused silica glass substrates (from Neubert-Glas). The obtained crossed grating structures were coated with 20 nm of aluminium by vacuum thermal evaporation (HHV AUTO 306 from HHV Ltd.) in a vacuum of at least 10^{-7} bar. Samples without the corrugation were prepared in order to serve as reference. The morphology of the nanostructure gratings samples was studied with AFM. The periodicity in the nanostructure was 200 nm and modulation depth about 30 nm as shown in Figure 4.21(a-b).

Transmission wavelength spectrum was measured for the aluminium crossed grating that was brought in contact with air. The angle of incidence was varied in the range θ=0–30

deg. The acquired wavelength transmission spectrum was normalized with that measured for a plane surface without grating. The experimental results are compared with simulations in Figure 4.21(b-c). Firstly, dependence of absorption on the wavelength and angle of incidence θ was used in order to identify dispersion of excited surface plasmon modes at the air-aluminum and Amonil-aluminum interfaces. Figure 4.21(c) reveals the excitation of two of these surface modes at the interface with a sample (SPs) and Amonil (SPa) which is manifested as increased absorption. The resonant excitation of surface plasmons travelling along the air interface with a normally incident beam θ=0 deg occurs at the wavelength of λ=214 nm. For the interface with Amonil, the resonance occurs at longer wavelength around λ=350 nm due to its higher refractive index n_a. When increasing the angle of incidence, these resonances split to two branches resulting in characteristic V-shaped spectra. The reason is that the excitation occurs simultaneously via +1st or –1st diffraction orders at wavelength where the phase-matching condition is fulfilled. When the angle of incidence is θ=0, the resonance associated with the coupling via $m = +1$ and $m = -1$ overlaps at each interface. However, when the angle of incidence θ deviates from zero, each resonance split to two branches. The prepared cross-gratings substrates were handed were to our collaborators, and were used for the UV-SPR biosensor for biomolecular interaction studies. The summary of these studies is presented in the following section.

4.4.2.2 Summary

A facile implementation of UV-SPR biosensor that is suitable for the in situ observation of molecular binding at the aluminium surface is reported. The results clearly indicate the possibility to resonantly excite and interrogate surface plasmons at wavelength of 280 nm. Diffraction coupling to SPR in the UV range exhibit similar sensitivity to that reported on regular gold diffraction grating sensors that operated in the red part of spectrum. The aluminium surface can be functionalized with silane-based linkers for the immobilization of biomolecules with density that is comparable to that observed for regular thiol self-assembled monolayer architectures on gold. The use of the UV wavelength of 280 nm holds potential for the combined measurement of plasmonically amplified auto-fluorescence of proteins. For the developed grating chip, the resonant wavelength can be easily tuned by adjusting the angle of incidence to even lower wavelengths, e.g. towards 260 nm where the DNA exhibits absorption maximum.

4.4.3 Project-III: Plasmonic nanoparticle arrays for surface enhanced Raman scattering spectroscopy

Metallic nanoparticles have the capability to couple light energy with collective oscillations of electron density at narrow wavelength bands. This phenomenon is referred to as localized surface plasmon resonance and it is associated with enhanced absorption and scattering [238]. In addition, it allows to strongly confining energy of electromagnetic field which is accompanied with its increased intensity. These characteristics can strongly amplify weak spectroscopic signals such as Raman scattering and fluorescence by several orders of magnitudes, enabling ultrasensitive detection of chemical and biological species [80].

During this work, protocols were established for the preparation of arrays of nanoparticles with period, diameter and height controlled in a desired range over large surface areas (area = 20 × 20 mm) by LIL. The fabrication method of NPs arrays is illustrated schematically in Figure 4.22. BK7 glass microscope slides (20 × 20 mm) having a 2 nm thick chromium layer (as adhesion), a 50 nm thick gold layer, and a 100

nm thick positive photoresist film, were exposed by 1D sinusoidal interference pattern formed by two crossed coherent collimated beams in a Lloyd's mirror interferometer setup. This produce a periodic interference pattern on a photoresist film with a spatial period of $\Lambda = \lambda/2\sin\theta$, where λ is the wavelength of the laser (in this work 325 nm) and θ is the half angle between the two beams. In order to prepare 2D sinusoidal pattern in the photoresist film each sample was rotated by 90° (after the first interferometric exposure) along the axis perpendicular to its surface and the exposure was repeated. The exposed photoresist film was developed in AZ 303 developer. By controlling the development time t_{dev}, the photoresist layer can be fully removed from the exposed area which yields a mask in form of periodic arrays of resist features. Afterwards, directional dry etching with an argon milling system (Roth & Rau IonSys 500) was carried out to transfer the pattern into the underlying gold layer (etching time 450 seconds, 70 degrees). Finally, the remaining resist was removed using oxygen plasma.

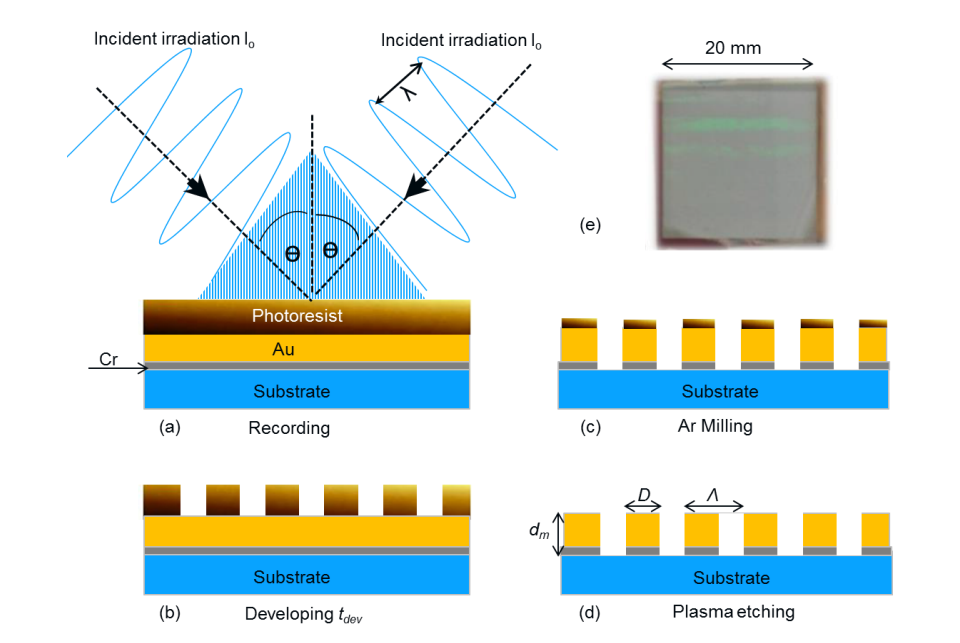

Fig. 4.22: (a-d) Schematic representation of the steps involved in the preparation of gold nanoparticles on a BK7 glass substrate with a thin adhesion promoter film Cr, using LIL combined with dry and plasma etching. (a) Recording of an interference field pattern into a photoresist. (b) Development of photoresist. (c) Dry etching. (d) Plasma etching. (e) Example of prepared gold nanoparticle arrays on a glass substrate with the size of 20 × 20 mm.

Figure 4.23 shows an example of the nanoparticles arrays prepared in this work by LIL, the fabrication of such array of nanoparticles with tailored morphology has typically been carried out using focused ion beam milling of electron-beam lithography techniques that are relatively expensive and time consuming [239, 240]. The LIL approach offers means for rapid fabrication of periodic arrays of nanostructures with facile control over shape, size, and spacing [241]. Adjusting the parameters of the LIL process allows for the preparation of nanoparticles with diameter below hundred nano-meters independently of their lattice spacing. The nanoparticle arrays can be engineered to be resonant to desired wavelengths in the visible and near infrared part of the spectrum. Applicability of these substrates is demonstrated for surface enhanced Raman scattering (SERS) spectroscopy,

where tailored, cost-effective, large area, uniform and reproducible substrates are of paramount importance for practical applications.

The fabrication of metal nanoparticles with LIL method using lift-off or ion etching steps has been already reported. In the lift-off approach, arrays metallic nanoparticles are fabricated by evaporating metal inside the photoresist cavities which are typically removed afterwards by a solvent [242]. The example of such cavities prepared in this work is shown in Figure 4.24(a). In this approach, nanoparticle size for a particular period is fixed since the pore size is bound to the pitch length, leading to restricted diameter/period configurations [243, 244]. In this context, additional strategies such as increasing the number of interfering beams or those based on a sacrificial layer often require facilitating the lift-off and avoiding resist caps and complete coating of the sidewalls [245, 246]. In both approaches, the tuning of LSPR on prepared arrays of metallic nanoparticles was mainly achieved by changing the angle between the interfering beams which changed both period and size of metallic nanoparticles. Besides the lack of independent control of these parameters, additional limitation of lift-off based LIL is the limited smallest attainable size feature. Features below hundred nano-meters have been only obtained for very small periodicities of the arrays or by using complex systems such as extreme ultraviolet LIL with a beam emitted from a synchrotron [242, 243].

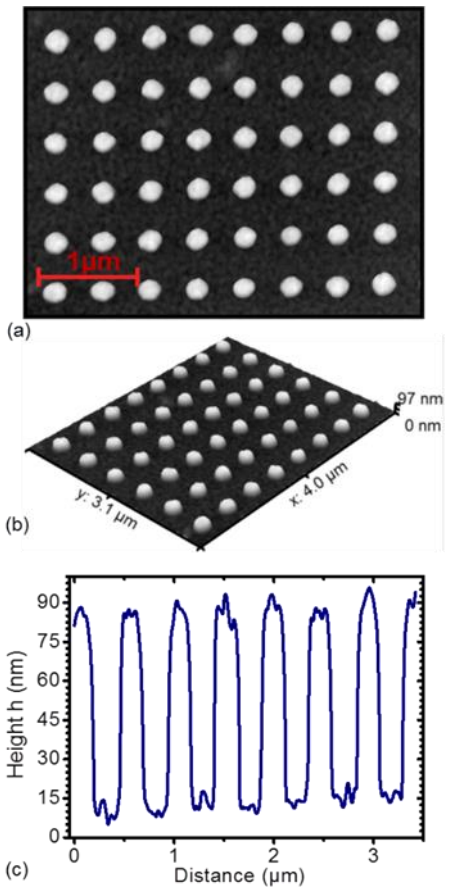

Fig. 4.23: (a) AFM image (b) 3D view and (c) height profile of the nanoparticles arrays. The exposure to LIL was carried out twice for two orientations of the sample rotated by 90° along the axis perpendicular to the substrate, each exposure time was 3 min and development time was 55 sec.

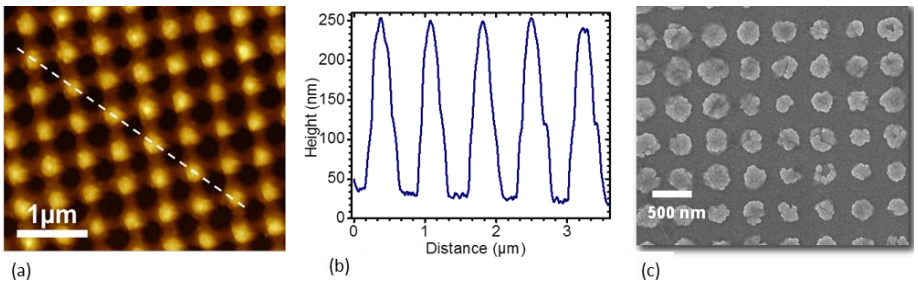

Fig. 4.24: (a-b) AFM image and cross section profile of the photoresist film with cavities made with LIL (c) the zinc oxide rods grown in photoresist cavities by electrochemical deposition method for transparent electrode applications.

The established protocols for the fabrication of arrays of nanoparticles during this work were further improved and fine-tuned by Nestor Gisbert Quilis. The summary of the prepared gold nanoparticle arrays is presented in the following section.

4.4.3.1 Summary

Plasmonic properties of arrays of metallic nanoparticles strongly depend on particle size, composition, surrounding medium and period [242, 243]. Therefore the plasmonic nanostructures have to be engineered and tuned for specific applications, requiring highly tuneable nanofabrication methods. We report on a rapid LIL implementation that offers high tunability of arrays of metallic nanoparticles over a square centimeter surface area by independent control of their diameter and period. Series of substrates with arrays of cylindrical gold nanoparticles exhibiting LSPR wavelength in the red and near infrared part of the spectrum were prepared by independently varying the diameter between 70 and 350 nm and period between 260 and 560 nm (see Figure 4.25). For the SERS experiments plasmonic substrates with identical LSPR wavelengths tuned to the vicinity of 785 nm and different spectral width were prepared. The importance of the control of both these parameters that was enabled by the developed LIL method to maximize the SERS signal is demonstrated.

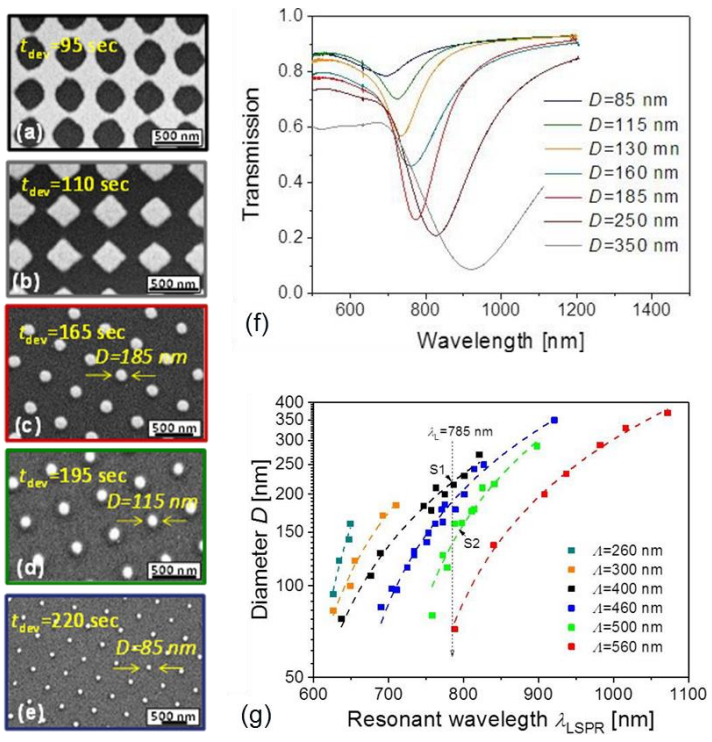

Fig. 4.25: SEM images of metallic nanoparticle arrays for varied development time t_{dev} and a period fixed of Λ=460 nm. (a) t_{dev} = 95 s, D=350 nm; (b) t_{dev} =110 s, D=350 nm; (c) t_{dev} =165 s, D=185 nm; (d) t_{dev} =195 s, D=115 nm; (e) t_{dev} =220 s, D=85 nm. (f) Transmission spectra measured for indicated gold disk diameters D and period Λ=460 nm. The spectral position of LSPR is manifested as a dip in the transmission spectrum. The wavelength at which minimum of the dip occurs λ_{LSPR} red shifts when increasing the diameter. (g) Dependence of the resonant wavelength λ_{LSPR} on gold nanoparticle arrays in contact with air on the diameter D and period between Λ=260–560 nm. The ability of independent tuning by both period and diameter for the control of LSPR is demonstrated in the broad range of λ_{LSPR}=620–1050 nm

Chapter 5 Conclusions and outlook

Photovoltaics represents a research domain that is pursued to provide sustainable, cheap and environmentally friendly source of energy to modern society. These efforts aim at harnessing light energy radiated by the Sun which reaches Earth's surface. The efficient exploiting of this source can make photovoltaic technology a major source of electricity and satisfy world's current and future power demands. To make this happen, the recently emerged thin film photovoltaic cells and already stablished industrial (silicon-based and chalcogenide-based) solar cells that are available on the market has to be economically competitive with other conventional energy sources. The photovoltaic community suggests different approaches to address this challenge i.e. to reduce the cost per Watt of generated energy from photovoltaic technology. These approaches can be categorized into following three fields, which usually influencing each other and therefore puts a huge challenge on the overall optimization of the photovoltaic device and its power conversion efficiency.

- Material engineering: it includes; engineering of semiconductor absorber to have good electronic properties, bandgap engineering for broader absorption spectrum and development of new cheap materials (active layer, electrodes).
- Processing engineering: investigation and optimization of deposition methods (low-temperature processing and low vacuum deposition conditions), interface engineering of different layers of the device.
- Optical engineering: device design and optical optimization of active layer thickness and light management.

This work deals with field of optical engineering and focuses on the light management. Light management in photovoltaic technology, in general, is carried out to more efficiently absorb incident photons in the absorber layer of the device, while using less material volume. This is of paramount interest, not only because the use of less material usually leads to a lower manufacture cost of the device, but also because of the use of less material reduces distances across the photovoltaic device, which suppresses non-radiative recombination and therefore increases the power conversion efficiency. The nanostructured materials explored in this thesis fall under umbrella of light management and may offer a panel of different attractive ways to manipulate with light in thin film devices for the control of optical properties. In the field of photovoltaic solar cells technologies, purposeful design of plasmonic and dielectric nanostructures may advance their characteristics in order to meet the required level by the industry. The work presented here deals with light management with plasmonic and dielectric nanostructures while aiming at realistic designs from a technological point of view.

The advances in nanofabrication and computational simulations opened up a wide variety of new nanostructures. The nano-photonic community has primarily focused on nanostructures that enhance the optical absorption without increasing the thickness of the absorber layers in organic photovoltaics. One promising approach incorporates plasmonic nanostructures and studies have generally found these nanostructures to be very effective in enhancing the absorption. However, resonant coupling of light to plasmonic modes occurs only at narrow spectral windows, which does not allow for the efficient light harvesting over the broad spectrum of solar radiation. In the work presented in section 4.1

a new approach to broadband plasmonic absorber is carried out. It takes advantage of the coupling to surface plasmons on a multi-diffractive metallic grating that provides access to tunable and rich spectrum of momenta for their phase matching with incident light. In order to demonstrate this concept, a multi-diffractive structure was recorded by laser interference lithography into a photoresist, copied into a UV cross-linkable polymer, and subsequently coated by aluminium and a thin standard polymer-based photovoltaic active material layer (poly(3-hexylthiophene) (P3HT) and 1-(3-methoxycarbonyl)propyl-1-phenyl[6,6]C61 (PCMB)). The presented work showed that superimposing three diffraction gratings allows extending the absorption band of applied polymer blend into the NIR part of spectrum. The work demonstrates that this structure enhances the absorption in the P3HT:PCBM by a factor of 2.9 in the spectral window 600–750 nm where it is inherently weakly absorbing. Over the whole visible / NIR part of spectrum 400–750 nm the number of absorbed photons in P3HT:PCBM is increased by 28 %. It is important to note here, micro/nano-structures that enhance light absorption in the absorber do not necessarily translate to an improvement of the overall PV solar cell power conversion efficiency. In general, this is not an issue for aperiodic nanostructures [247] and periodic microstructures [111, 112] that are separated from active layers of a solar cell by a transparent substrate. However, when high aspect ratio metallic nanostructures are deployed between electrodes that directly interface with solar cell absorber layer, electric field becomes modulated along the surface which can deteriorate charge carrier extraction and eventually cancel the positive effect of enhanced absorption [191]. It is therefore underlined that the impact of light management architecture that increases absorption should be at least neutral to the electrical charge transport process. The multi-diffractive gratings investigated in the present work exhibit relatively shallow topographic profile. Therefore, they are not expected to cause significant electric field inhomogeneities that would hinder charge carrier harvesting. Recent investigations reported on the using of randomly attached Ag nanoparticles [248] and aperiodic relief nanostructures on Al electrode [249] in thin film plasmonic solar cells. They comprised features with feature size comparable to the present work and they were demonstrated to significantly enhance power conversion efficiency by the increased light absorption.

The use of plasmonic nanostructures has the tendency to increase parasitic optical absorption loss due to the Ohmic losses in the metal, which competes with absorption in the photoactive layer of the solar cell device. Therefore we witnessed numerous approaches for optical manipulation of light in field of thin film solar cells, based on dielectric nanostructures. In section 4.2, the work focuses on dielectric nanostructures for light management. In this context the transparent electrode ITO of organic photovoltaic solar cell was corrugated. The ITO film was sputtered to an UV-NIL imprinted glass substrate and experimentally investigated. The design of the corrugation in order to function as light trapping or antireflection nanostructure is demonstrated and elucidated in terms of diffraction coupling to dielectric waveguide modes and by suppressing the reflections at ITO interfaces respectively. The design identifies key rules to tune the structure to serve for high transmission or light trapping applications. For dense periodic structure with Λ=200 nm and aspect ratio of about 0.5, the average increase of transmittance by 8 % at broad spectral window λ=450–850 nm is measured for polar angles between 0 and 60°. When increasing the period, light trapping becomes dominant via diffraction coupling to waveguide modes. The light trapping over broad range of angles and wavelength in the visible and near infrared part of spectrum occurs for about

100 nm thick ITO films without significant change in its sheet resistance which is 35 ± 3 Ω/square.

In nutshell, new facile means for the preparation of nanostructures with tailored optical properties that can be scaled up were developed based on laser interference lithography. The investigated nanostructures in this work may offer attractive means for improving performance of thin film solar cells and can potentially find its applications also in other fields e.g. light emitting diodes other optoelectronics devices and in the field of biosensing. For example, the single period crossed relief aluminium grating prepared in this work was successfully employed for diffraction coupling to surface plasmons in the UV part of spectrum as an alternative to more commonly used attenuated total reflection method [237]. Similarly, linear grating prepared in this work were used in a smartphone label-free biosensor platform based on grating coupled surface plasmon resonance for the detection Lipopolysaccharides [221]. Besides to these applications, the herein presented nanomaterials and means to prepare them can find their application in other technologies and provide functionalities such as polarizers [250], colour filters [251], and selective reflectors [252, 253].

References

1. A. Jäger-Waldau, "PV Status Report 2008. Research, Solar Cell Production and Market Implementation of Photovoltaics," (Renewable Energy Unit, 2008).

2. M. D. Archer, and M. A. Green, *Clean electricity from photovoltaics* (World Scientific, 2014).

3. L. L. Kazmerski, "Solar photovoltaics R&D at the tipping point: A 2005 technology overview," Journal of Electron Spectroscopy and Related Phenomena **150**, 105-135 (2006).

4. A.-E. Becquerel, "Mémoire sur les effets électriques produits sous l'influence des rayons solaires," Comptes rendus **9**, 1839 (1839).

5. D. M. Chapin, C. Fuller, and G. Pearson, "A new silicon p-n junction photocell for converting solar radiation into electrical power," Journal of Applied Physics **25**, 676-677 (1954).

6. L. Schnatbaum, "Solar thermal power plants," The European Physical Journal-Special Topics **176**, 127-140 (2009).

7. S. Bockamp, T. Griestop, M. Fruth, M. Ewert, H. Lerchenmüller, M. Mertins, G. Morin, A. Häberle, and J. Dersch, "Solar thermal power generation," in *Power-Gen Europe*(2003).

8. M. A. Green, "Thin-film solar cells: review of materials, technologies and commercial status," Journal of Materials Science: Materials in Electronics **18**, 15-19 (2007).

9. A. J. Trappey, C. V. Trappey, H. Tan, P. H. Liu, S.-J. Li, and L.-C. Lin, "The determinants of photovoltaic system costs: an evaluation using a hierarchical learning curve model," Journal of Cleaner Production **112**, 1709-1716 (2016).

10. H. Shirakawa, E. J. Louis, A. G. MacDiarmid, C. K. Chiang, and A. J. Heeger, "Synthesis of electrically conducting organic polymers: halogen derivatives of polyacetylene,(CH) x," Journal of the Chemical Society, Chemical Communications, 578-580 (1977).

11. S. Günes, H. Neugebauer, and N. S. Sariciftci, "Conjugated polymer-based organic solar cells," Chemical Reviews **107**, 1324-1338 (2007).

12. C. Brabec, U. Scherf, and V. Dyakonov, *Organic photovoltaics: materials, device physics, and manufacturing technologies* (John Wiley & Sons, 2011).

13. S. E. Shaheen, D. S. Ginley, and G. E. Jabbour, "Organic-based photovoltaics: toward low-cost power generation," MRS bulletin **30**, 10-19 (2005).

14. C. J. Brabec, "Organic photovoltaics: technology and market," Solar Energy Materials and Solar Cells **83**, 273-292 (2004).

15. A. Goetzberger, C. Hebling, and H.-W. Schock, "Photovoltaic materials, history, status and outlook," Materials Science and Engineering: R: Reports **40**, 1-46 (2003).

16. P. Peumans, A. Yakimov, and S. R. Forrest, "Small molecular weight organic thin-film photodetectors and solar cells," Journal of Applied Physics **93**, 3693-3723 (2003).

17. G. Hadziioannou, and P. Van Hutten, *Semiconducting polymers* (Wiley VCH, 2000).

18. M. Wright, and A. Uddin, "Organic—inorganic hybrid solar cells: A comparative review," Solar Energy Materials and Solar Cells **107**, 87-111 (2012).

19. S. S. Sun, and N. S. Sariciftci, *Organic Photovoltaics: Mechanisms, Materials, and Devices* (CRC Press, 2005).

20. H. Kallmann, and M. Pope, "Photovoltaic effect in organic crystals," The Journal of Chemical Physics **30**, 585-586 (1959).

21. A. K. Ghosh, and T. Feng, "Merocyanine organic solar cells," Journal of Applied Physics **49**, 5982-5989 (1978).

22. G. Chamberlain, "Organic solar cells: A review," Solar cells **8**, 47-83 (1983).

23. C. W. Tang, "Two-layer organic photovoltaic cell," Applied Physics Letters **48**, 183-185 (1986).

24. G. Yu, J. Gao, J. C. Hummelen, F. Wudl, and A. J. Heeger, "Polymer photovoltiac cells: Enhanced efficiencies via a network of internal donor-acceptor heterojunctions," Science **270**, 1789 (1995).

25. S. E. Shaheen, C. J. Brabec, N. S. Sariciftci, F. Padinger, T. Fromherz, and J. C. Hummelen, "2.5% efficient organic plastic solar cells," Applied Physics Letters **78**, 841-843 (2001).

26. R. F. Service, "Solar energy. Outlook brightens for plastic solar cells," Science (New York, NY) **332**, 293 (2011).

27. J. Hou, and X. Guo, "Active layer materials for organic solar cells," in *Organic Solar Cells*(Springer, 2013), pp. 17-42.

28. S. H. Park, A. Roy, S. Beaupré, S. Cho, N. Coates, J. S. Moon, D. Moses, M. Leclerc, K. Lee, and A. J. Heeger, "Bulk heterojunction solar cells with internal quantum efficiency approaching 100%," Nature photonics **3**, 297-302 (2009).

29. S. J. Kim, G. Y. Margulis, S.-B. Rim, M. L. Brongersma, M. D. McGehee, and P. Peumans, "Geometric light trapping with a V-trap for efficient organic solar cells," Opt. Express **21**, A305-A312 (2013).

30. A. Pivrikas, N. S. Sariciftci, G. Juška, and R. Österbacka, "A review of charge transport and recombination in polymer/fullerene organic solar cells," Progress in Photovoltaics: Research and Applications **15**, 677-696 (2007).

31. J. Gilot, I. Barbu, M. M. Wienk, and R. A. Janssen, "The use of ZnO as optical spacer in polymer solar cells: Theoretical and experimental study," Applied Physics Letters **91**, 113520 (2007).

32. Z. Wang, E. Wang, L. Hou, F. Zhang, M. Andersson, and O. Inganäs, "Mixed solvents for reproducible photovoltaic bulk heterojunctions," Journal of Photonics for Energy **1**, 011122-011122-011127 (2011).

33. B. Kippelen, and J.-L. Brédas, "Organic photovoltaics," Energy & Environmental Science **2**, 251-261 (2009).

34. H. Hoppe, and N. S. Sariciftci, "Organic solar cells: An overview," J. Mater. Res **19**, 1924-1945 (2004).

35. K. Petritsch, *Organic solar cell architectures* (na, 2000).

36. W. Peter, and W. Uli, *Physics of solar cells: from basic principles to advanced concepts* (John Wiley & Sons, 2016).

37. C. Brabec, U. Scherf, and V. Dyakonov, *Organic Photovoltaics: Materials, Device Physics, and Manufacturing Technologies* (Wiley, 2014).

38. D. Wöhrle, and D. Meissner, "Organic solar cells," Advanced Materials **3**, 129-138 (1991).

39. H. Hoppe, and N. S. Sariciftci, "Organic solar cells: An overview," Journal of materials research **19**, 1924-1945 (2004).

40. M. A. Green, "High efficiency silicon solar cells," in *Seventh EC Photovoltaic Solar Energy Conference*(Springer, 1987), pp. 681-687.

41. J.-M. Nunzi, "Organic photovoltaic materials and devices," Comptes Rendus Physique **3**, 523-542 (2002).

42. C. Deibel, and V. Dyakonov, "Polymer–fullerene bulk heterojunction solar cells," Reports on Progress in Physics **73**, 096401 (2010).

43. M. C. Scharber, and N. S. Sariciftci, "Efficiency of bulk-heterojunction organic solar cells," Progress in polymer science **38**, 1929-1940 (2013).

44. T. Kirchartz, K. Taretto, and U. Rau, "Efficiency limits of organic bulk heterojunction solar cells," The Journal of Physical Chemistry C **113**, 17958-17966 (2009).

45. A. J. Mozer, and N. S. Sariciftci, "Conjugated polymer photovoltaic devices and materials," Comptes Rendus Chimie **9**, 568-577 (2006).

46. E. Bucher, "Solar cell materials and their basic parameters," Applied physics **17**, 1-26 (1978).

47. L. Sicot, "Etude et réalisation de cellules photovoltaïques en polymère," (1999).

48. J. Rostalski, and D. Meissner, "Monochromatic versus solar efficiencies of organic solar cells," Solar Energy Materials and Solar Cells **61**, 87-95 (2000).

49. W. C. Choy, *Organic solar cells: materials and device physics* (Springer, 2012).

50. N. Blouin, A. Michaud, and M. Leclerc, "A low-bandgap poly (2, 7-carbazole) derivative for use in high-performance solar cells," Advanced Materials **19**, 2295-2300 (2007).

51. H.-Y. Chen, J. Hou, S. Zhang, Y. Liang, G. Yang, Y. Yang, L. Yu, Y. Wu, and G. Li, "Polymer solar cells with enhanced open-circuit voltage and efficiency," Nature photonics **3**, 649-653 (2009).

52. J. Peet, J. Y. Kim, N. E. Coates, W. L. Ma, D. Moses, A. J. Heeger, and G. C. Bazan, "Efficiency enhancement in low-bandgap polymer solar cells by processing with alkane dithiols," Nature materials **6**, 497-500 (2007).

53. P. W. Blom, V. D. Mihailetchi, L. J. A. Koster, and D. E. Markov, "Device physics of polymer: fullerene bulk heterojunction solar cells," Advanced Materials **19**, 1551-1566 (2007).

54. L. M. Chen, Z. Hong, G. Li, and Y. Yang, "Recent progress in polymer solar cells: manipulation of polymer: fullerene morphology and the formation of efficient inverted polymer solar cells," Advanced Materials **21**, 1434-1449 (2009).

55. S. Albrecht, S. Schäfer, I. Lange, S. Yilmaz, I. Dumsch, S. Allard, U. Scherf, A. Hertwig, and D. Neher, "Light management in PCPDTBT: PC 70 BM solar cells: A comparison of standard and inverted device structures," Organic Electronics **13**, 615-622 (2012).

56. S.-B. Rim, S. Zhao, S. R. Scully, M. D. McGehee, and P. Peumans, "An effective light trapping configuration for thin-film solar cells," Applied Physics Letters **91**, 243501 (2007).

57. L. Song, and A. Uddin, "Design of high efficiency organic solar cell with light trapping," Opt. Express **20**, A606-A621 (2012).

58. H. Zhen, K. Li, Z. Huang, Z. Tang, R. Wu, G. Li, X. Liu, and F. Zhang, "Inverted indium-tin-oxide-free cone-shaped polymer solar cells for light trapping," Applied Physics Letters **100**, 213901 (2012).

59. B. O'Connor, C. Haughn, K.-H. An, K. P. Pipe, and M. Shtein, "Transparent and conductive electrodes based on unpatterned, thin metal films," Applied Physics Letters **93**, 433 (2008).

60. Y. Long, and 龙拥兵, "Improving optical performance of inverted organic solar cells by microcavity effect," Applied Physics Letters **95**, 295 (2009).

61. J. Lee, S.-Y. Kim, C. Kim, and J.-J. Kim, "Enhancement of the short circuit current in organic photovoltaic devices with microcavity structures," Applied Physics Letters **97**, 187 (2010).

62. G. H. Jung, K. Hong, W. J. Dong, S. Kim, and J. L. Lee, "BCP/Ag/MoO3 transparent cathodes for organic photovoltaics," Advanced Energy Materials **1**, 1023-1028 (2011).

63. N. P. Sergeant, A. Hadipour, B. Niesen, D. Cheyns, P. Heremans, P. Peumans, and B. P. Rand, "Design of transparent anodes for resonant cavity enhanced light harvesting in organic solar cells," Advanced Materials **24**, 728-732 (2012).

64. S. Schubert, J. Meiss, L. Müller-Meskamp, and K. Leo, "Improvement of transparent metal top electrodes for organic solar cells by introducing a high surface energy seed layer," Advanced Energy Materials **3**, 438-443 (2013).

65. B. E. Saleh, M. C. Teich, and B. E. Saleh, *Fundamentals of photonics* (Wiley New York, 1991).

66. K. Tvingstedt, S. Dal Zilio, O. Inganäs, and M. Tormen, "Trapping light with micro lenses in thin film organic photovoltaic cells," Opt. Express **16**, 21608-21615 (2008).

67. S. J. Choi, and S. Y. Huh, "Direct Structuring of a Biomimetic Anti-Reflective, Self-Cleaning Surface for Light Harvesting in Organic Solar Cells," Macromolecular rapid communications **31**, 539-544 (2010).

68. J. D. Chen, L. Zhou, Q. D. Ou, Y. Q. Li, S. Shen, S. T. Lee, and J. X. Tang, "Enhanced Light Harvesting in Organic Solar Cells Featuring a Biomimetic Active Layer and a Self-Cleaning Antireflective Coating," Advanced Energy Materials **4** (2014).

69. H. Shen, P. Bienstman, and B. Maes, "Plasmonic absorption enhancement in organic solar cells with thin active layers," Journal of Applied Physics **106**, 073109 (2009).

70. C. Min, J. Li, G. Veronis, J.-Y. Lee, S. Fan, and P. Peumans, "Enhancement of optical absorption in thin-film organic solar cells through the excitation of plasmonic modes in metallic gratings," Applied Physics Letters **96**, 56 (2010).

71. D. Duche, P. Torchio, L. Escoubas, F. Monestier, J.-J. Simon, F. Flory, and G. Mathian, "Improving light absorption in organic solar cells by plasmonic contribution," Solar Energy Materials and Solar Cells **93**, 1377-1382 (2009).

72. S.-W. Baek, J. Noh, C.-H. Lee, B. Kim, M.-K. Seo, and J.-Y. Lee, "Plasmonic forward scattering effect in organic solar cells: a powerful optical engineering method," Scientific Reports **3** (2013).

73. K. Forberich, G. Dennler, M. C. Scharber, K. Hingerl, T. Fromherz, and C. J. Brabec, "Performance improvement of organic solar cells with moth eye anti-reflection coating," Thin Solid Films **516**, 7167-7170 (2008).

74. S. Lal, S. Link, and N. J. Halas, "Nano-optics from sensing to waveguiding," Nat Photon **1**, 641-648 (2007).

75. Z. Jacob, and V. M. Shalaev, "Plasmonics goes quantum," Science **334**, 463-464 (2011).

76. J. Homola, "Surface plasmon resonance based sensors, Springer series on chemical sensors and biosensor/Methods and Applications," Springer tracts in modern physics, Springer-Verlag Berlin ed., Heidelberg NY **4**, 7-8 (2006).

77. S. Pillai, and M. Green, "Plasmonics for photovoltaic applications," Solar Energy Materials and Solar Cells **94**, 1481-1486 (2010).

78. H. A. Atwater, and A. Polman, "Plasmonics for improved photovoltaic devices," Nature materials **9**, 205-213 (2010).

79. V. E. Ferry, J. N. Munday, and H. A. Atwater, "Design considerations for plasmonic photovoltaics," Advanced Materials **22**, 4794-4808 (2010).

80. M. Bauch, K. Toma, M. Toma, Q. Zhang, and J. Dostalek, "Plasmon-enhanced fluorescence biosensors: a review," Plasmonics **9**, 781-799 (2014).

81. A. Polman, and H. A. Atwater, "Plasmonics: optics at the nanoscale," Materials Today **8**, 56 (2005).

82. B. Zeng, Q. Gan, Z. H. Kafafi, and F. J. Bartoli, "Polymeric photovoltaics with various metallic plasmonic nanostructures," Journal of Applied Physics **113**, 063109 (2013).

83. B. H. Nguyen, V. H. Nguyen, and D. L. Vu, "Plasmonic enhancement of light trapping into organic solar cells," Advances in Natural Sciences: Nanoscience and Nanotechnology **6**, 043002 (2015).

84. P. Spinelli, V. Ferry, J. Van de Groep, M. Van Lare, M. Verschuuren, R. Schropp, H. Atwater, and A. Polman, "Plasmonic light trapping in thin-film Si solar cells," Journal of Optics **14**, 024002 (2012).

85. S.-S. Kim, S.-I. Na, J. Jo, D.-Y. Kim, and Y.-C. Nah, "Plasmon enhanced performance of organic solar cells using electrodeposited Ag nanoparticles," Applied Physics Letters **93**, 305 (2008).

86. K. Kim, B. Jung, J. Kim, and W. Kim, "Effects of embedding non-absorbing nanoparticles in organic photovoltaics on power conversion efficiency," Solar Energy Materials and Solar Cells **94**, 1835-1839 (2010).

87. W. Hergert, and T. Wriedt, *The Mie Theory: basics and applications* (Springer, 2012).

88. Q. Fu, and W. Sun, "Mie theory for light scattering by a spherical particle in an absorbing medium," Appl. Opt. **40**, 1354-1361 (2001).

89. I. Kim, T. S. Lee, D. S. Jeong, W. S. Lee, and K.-S. Lee, "Size effects of metal nanoparticles embedded in a buffer layer of organic photovoltaics on plasmonic absorption enhancement," Journal of Physics D: Applied Physics **45**, 065101 (2012).

90. K. Jung, H.-J. Song, G. Lee, Y. Ko, K. Ahn, H. Choi, J. Y. Kim, K. Ha, J. Song, and J.-K. Lee, "Plasmonic organic solar cells employing nanobump assembly via aerosol-derived nanoparticles," ACS nano **8**, 2590-2601 (2014).

91. S.-W. Baek, G. Park, J. Noh, C. Cho, C.-H. Lee, M.-K. Seo, H. Song, and J.-Y. Lee, "Au@ Ag core–shell nanocubes for efficient plasmonic light scattering effect in low bandgap organic solar cells," ACS nano **8**, 3302-3312 (2014).

92. P. Du, P. Jing, D. Li, Y. Cao, Z. Liu, and Z. Sun, "Plasmonic Ag@ oxide nanoprisms for enhanced performance of organic solar cells," Small **11**, 2454-2462 (2015).

93. Y. A. Akimov, W. S. Koh, and K. Ostrikov, "Enhancement of optical absorption in thin-film solar cells through the excitation of higher-order nanoparticle plasmon modes," Opt. Express **17**, 10195-10205 (2009).

94. S.-Q. Zhu, T. Zhang, X.-L. Guo, F. Shan, and X.-Y. Zhang, "Light absorption enhancement in organic solar cell by embedding Ag nanoparticles and nanochains within the active layer," Journal of Nanomaterials **2014**, 45 (2014).

95. I. Diukman, L. Tzabari, N. Berkovitch, N. Tessler, and M. Orenstein, "Controlling absorption enhancement in organic photovoltaic cells by patterning Au nano disks within the active layer," Opt. Express **19**, A64-A71 (2011).

96. D. Qu, F. Liu, Y. Huang, W. Xie, and Q. Xu, "Mechanism of optical absorption enhancement in thin film organic solar cells with plasmonic metal nanoparticles," Opt. Express **19**, 24795-24803 (2011).

97. C. Liu, C. Zhao, X. Zhang, W. Guo, K. Liu, and S. Ruan, "Unique Gold Nanorods Embedded Active Layer Enabling Strong Plasmonic Effect To Improve the Performance of Polymer Photovoltaic Devices," The Journal of Physical Chemistry C **120**, 6198-6205 (2016).

98. X. Li, W. C. H. Choy, H. Lu, W. E. Sha, and A. H. P. Ho, "Efficiency Enhancement of Organic Solar Cells by Using Shape-Dependent Broadband Plasmonic Absorption in Metallic Nanoparticles," Advanced Functional Materials **23**, 2728-2735 (2013).

99. H. Raether, *Surface plasmons on smooth and rough surfaces and on gratings* (Springer-Verlag Berlin An, 2013).

100. A. Baba, N. Aoki, K. Shinbo, K. Kato, and F. Kaneko, "Grating-coupled surface plasmon enhanced short-circuit current in organic thin-film photovoltaic cells," ACS applied materials & interfaces **3**, 2080-2084 (2011).

101. X. Li, W. C. Choy, X. Ren, J. Xin, P. Lin, and D. C. Leung, "Polarization-independent efficiency enhancement of organic solar cells by using 3-dimensional plasmonic electrode," Applied Physics Letters **102**, 64 (2013).

102. S. I. Na, S. S. Kim, J. Jo, S. H. Oh, J. Kim, and D. Y. Kim, "Efficient polymer solar cells with surface relief gratings fabricated by simple soft lithography," Advanced Functional Materials **18**, 3956-3963 (2008).

103. P. Zijlstra, J. W. M. Chon, and M. Gu, "Five-dimensional optical recording mediated by surface plasmons in gold nanorods," Nature **459**, 410-413 (2009).

104. J. Dostálek, and W. Knoll, "2.26 - Plasmonics A2 - Matyjaszewski, Krzysztof," in *Polymer Science: A Comprehensive Reference*, M. Möller, ed. (Elsevier, Amsterdam, 2012), pp. 647-659.

105. R. Bel Hadj Tahar, T. Ban, Y. Ohya, and Y. Takahashi, "Tin doped indium oxide thin films: Electrical properties," Journal of Applied Physics **83**, 2631-2645 (1998).

106. E. Kretschmann, and H. Raether, "Notizen: radiative decay of non radiative surface plasmons excited by light," Zeitschrift für Naturforschung A **23**, 2135-2136 (1968).

107. W. L. Barnes, A. Dereux, and T. W. Ebbesen, "Surface plasmon subwavelength optics," Nature **424**, 824-830 (2003).

108. J. You, X. Li, F. x. Xie, W. E. Sha, J. H. Kwong, G. Li, W. C. Choy, and Y. Yang, "Surface Plasmon and Scattering-Enhanced Low-Bandgap Polymer Solar Cell by a Metal Grating Back Electrode," Advanced Energy Materials **2**, 1203-1207 (2012).

109. M. Niggemann, M. Glatthaar, A. Gombert, A. Hinsch, and V. Wittwer, "Diffraction gratings and buried nano-electrodes—architectures for organic solar cells," Thin Solid Films **451**, 619-623 (2004).

110. S.-I. Na, S.-S. Kim, S.-S. Kwon, J. Jo, J. Kim, T. Lee, and D.-Y. Kim, "Surface relief gratings on poly (3-hexylthiophene) and fullerene blends for efficient organic solar cells," Applied Physics Letters **91**, 173509 (2007).

111. S. Esiner, T. Bus, M. M. Wienk, K. Hermans, and R. A. Janssen, "Quantification and validation of the efficiency enhancement reached by application of a retroreflective light trapping texture on a polymer solar cell," Advanced Energy Materials **3**, 1013-1017 (2013).

112. J. D. Myers, W. Cao, V. Cassidy, S.-H. Eom, R. Zhou, L. Yang, W. You, and J. Xue, "A universal optical approach to enhancing efficiency of organic-based photovoltaic devices," Energy & Environmental Science **5**, 6900-6904 (2012).

113. P. Doshi, G. E. Jellison, and A. Rohatgi, "Characterization and optimization of absorbing plasma-enhanced chemical vapor deposited antireflection coatings for silicon photovoltaics," Appl. Opt. **36**, 7826-7837 (1997).

114. H. K. Raut, V. A. Ganesh, A. S. Nair, and S. Ramakrishna, "Anti-reflective coatings: A critical, in-depth review," Energy & Environmental Science **4**, 3779-3804 (2011).

115. J.-Q. Xi, M. F. Schubert, J. K. Kim, E. F. Schubert, M. Chen, S.-Y. Lin, W. Liu, and J. A. Smart, "Optical thin-film materials with low refractive index for broadband elimination of Fresnel reflection," Nature photonics **1**, 176-179 (2007).

116. C. S. Solanki, and H. K. Singh, *Anti-reflection and Light Trapping in c-Si Solar Cells* (Springer Singapore, 2017).

117. V. V. Iyengar, B. K. Nayak, and M. C. Gupta, "Optical properties of silicon light trapping structures for photovoltaics," Solar Energy Materials and Solar Cells **94**, 2251-2257 (2010).

118. R. B. Stephens, and G. D. Cody, "Optical reflectance and transmission of a textured surface," Thin Solid Films **45**, 19-29 (1977).

119. P. Hersch, and K. Zweibel, "Basic photovoltaic principles and methods," (Solar Energy Research Inst., Golden, CO (USA), 1982).

120. I. Hwang, D. Choi, S. Lee, J. H. Seo, K.-H. Kim, I. Yoon, and K. Seo, "Enhancement of Light Absorption in Photovoltaic Devices using Textured PDMS Stickers," ACS applied materials & interfaces (2017).

121. H. A. Macleod, *Thin-film optical filters* (CRC press, 2001).

122. D. Chen, "Anti-reflection (AR) coatings made by sol–gel processes: a review," Solar Energy Materials and Solar Cells **68**, 313-336 (2001).

123. C. Bernhard, "Structural and functional adaptation in a visual system," Endeavour **26**, 79-& (1967).

124. J. Gwamuri, A. Vora, J. Mayandi, D. Ö. Güney, P. L. Bergstrom, and J. M. Pearce, "A new method of preparing highly conductive ultra-thin indium tin oxide for plasmonic-enhanced thin film solar photovoltaic devices," Solar Energy Materials and Solar Cells **149**, 250-257 (2016).

125. P. B. Clapham, and M. C. Hutley, "Reduction of Lens Reflexion by the [ldquo]Moth Eye[rdquo] Principle," Nature **244**, 281-282 (1973).

126. Y. Li, J. Zhang, and B. Yang, "Antireflective surfaces based on biomimetic nanopillared arrays," Nano Today **5**, 117-127 (2010).

127. P. Lalanne, and J.-P. Hugonin, "High-order effective-medium theory of subwavelength gratings in classical mounting: application to volume holograms," JOSA A **15**, 1843-1851 (1998).

128. P. Lalanne, "Effective medium theory applied to photonic crystals composed of cubic or square cylinders," Appl. Opt. **35**, 5369-5380 (1996).

129. W.-K. Kuo, J.-J. Hsu, C.-K. Nien, and H. H. Yu, "Moth-Eye-Inspired Biophotonic Surfaces with Antireflective and Hydrophobic Characteristics," ACS applied materials & interfaces **8**, 32021-32030 (2016).

130. A. Gombert, and B. Blasi, "The moth-eye effect—From fundamentals to commercial exploitation," Functional properties of bio-inspired surfaces: characterization and technological applications. World Scientific Publishing Co., Hackensack, NJ, 79-102 (2009).

131. P. I. Stavroulakis, S. A. Boden, T. Johnson, and D. M. Bagnall, "Suppression of backscattered diffraction from sub-wavelength 'moth-eye'arrays," Opt. Express **21**, 1-11 (2013).

132. D.-H. Ko, J. R. Tumbleston, A. Gadisa, M. Aryal, Y. Liu, R. Lopez, and E. T. Samulski, "Light-trapping nano-structures in organic photovoltaic cells," Journal of Materials Chemistry **21**, 16293-16303 (2011).

133. A. Raman, Z. Yu, and S. Fan, "Dielectric nanostructures for broadband light trapping in organic solar cells," Opt. Express **19**, 19015-19026 (2011).

134. X. Li, W. C. Choy, L. Huo, F. Xie, W. E. Sha, B. Ding, X. Guo, Y. Li, J. Hou, and J. You, "Dual plasmonic nanostructures for high performance inverted organic solar cells," Advanced Materials **24**, 3046-3052 (2012).

135. P. P. Edwards, A. Porch, M. O. Jones, D. V. Morgan, and R. M. Perks, "Basic materials physics of transparent conducting oxides," Dalton Transactions, 2995-3002 (2004).

136. S. Nowy, B. C. Krummacher, J. Frischeisen, N. A. Reinke, and W. Brütting, "Light extraction and optical loss mechanisms in organic light-emitting diodes: Influence of the emitter quantum efficiency," Journal of Applied Physics **104**, 123109 (2008).

137. Z. Xia, *Biomimetic Principles and Design of Advanced Engineering Materials* (John Wiley & Sons, 2016).

138. S. Y. Chou, P. R. Krauss, and P. J. Renstrom, "Imprint lithography with 25-nanometer resolution," Science **272**, 85 (1996).

139. K. Carl, H. Schmitt, and I. Friedrich, "Optimization of sputtered ITO films with respect to the oxygen partial pressure and substrate temperature," Thin Solid Films **295**, 151-155 (1997).

140. C. Chiu, P. Yu, C. Chang, C. Yang, M. Hsu, H. Kuo, and M. Tsai, "Oblique electron-beam evaporation of distinctive indium-tin-oxide nanorods for enhanced light extraction from InGaN/GaN light emitting diodes," Opt. Express **17**, 21250-21256 (2009).

141. K. Kato, H. Omoto, T. Tomioka, and A. Takamatsu, "Changes in electrical and structural properties of indium oxide thin films through post-deposition annealing," Thin Solid Films **520**, 110-116 (2011).

142. J. W. Leem, and J. S. Yu, "Indium tin oxide subwavelength nanostructures with surface antireflection and superhydrophilicity for high-efficiency Si-based thin film solar cells," Opt. Express **20**, A431-A440 (2012).

143. H. Kwon, J. Ham, D. Y. Kim, S. J. Oh, S. Lee, S. H. Oh, E. F. Schubert, K. G. Lim, T. W. Lee, and S. Kim, "Three-Dimensional Nanostructured Indium-Tin-Oxide Electrodes for Enhanced Performance of Bulk Heterojunction Organic Solar Cells," Advanced Energy Materials **4** (2014).

144. M.-A. Tsai, H.-W. Han, Y.-L. Tsai, P.-C. Tseng, P. Yu, H.-C. Kuo, C.-H. Shen, J.-M. Shieh, and S.-H. Lin, "Embedded biomimetic nanostructures for enhanced optical absorption in thin-film solar cells," Opt. Express **19**, A757-A762 (2011).

145. R. A. Janssen, and J. Nelson, "Factors limiting device efficiency in organic photovoltaics," Advanced Materials **25**, 1847-1858 (2013).

146. M. G. Kang, T. Xu, H. J. Park, X. Luo, and L. J. Guo, "Efficiency enhancement of organic solar cells using transparent plasmonic Ag nanowire electrodes," Advanced Materials **22**, 4378-4383 (2010).

147. J. Van Deelen, L. Klerk, M. Barink, H. Rendering, P. Voorthuijzen, and A. Hovestad, "Improvement of transparent conducting materials by metallic grids on transparent conductive oxides," Thin Solid Films **555**, 159-162 (2014).

148. G. Kulkarni, and B. Radha, "Metal nanowire grating patterns," Nanoscale **2**, 2035-2044 (2010).

149. P. B. Catrysse, and S. Fan, "Nanopatterned metallic films for use as transparent conductive electrodes in optoelectronic devices," Nano Letters **10**, 2944-2949 (2010).

150. S. H. Ahn, and L. J. Guo, "Spontaneous formation of periodic nanostructures by localized dynamic wrinkling," Nano Letters **10**, 4228-4234 (2010).

151. J. Van De Groep, D. Gupta, M. A. Verschuuren, M. M. Wienk, R. A. Janssen, and A. Polman, "Large-area soft-imprinted nanowire networks as light trapping transparent conductors," Scientific Reports **5** (2015).

152. B. Zeng, Z. H. Kafafi, and F. J. Bartoli, "Transparent Conducting Electrodes based on 1D and 2D Ag Nanogratings for Organic Photovoltaics," arXiv preprint arXiv:1412.3439 (2014).

153. A. Fernandez, J. Decker, S. Herman, D. Phillion, D. Sweeney, and M. Perry, "Methods for fabricating arrays of holes using interference lithography," Journal of Vacuum Science & Technology B: Microelectronics and Nanometer Structures Processing, Measurement, and Phenomena **15**, 2439-2443 (1997).

154. J.-H. Seo, J. H. Park, S.-I. Kim, B. J. Park, Z. Ma, J. Choi, and B.-K. Ju, "Nanopatterning by laser interference lithography: applications to optical devices," Journal of nanoscience and nanotechnology **14**, 1521-1532 (2014).

155. Q. Xie, M. Hong, H. Tan, G. Chen, L. Shi, and T. Chong, "Fabrication of nanostructures with laser interference lithography," Journal of alloys and compounds **449**, 261-264 (2008).

156. W. R. Grove, "LXXIX. On the electro-chemical polarity of gases," Philosophical Magazine Series 4 **4**, 498-514 (1852).

157. S. Rossnagel, W. Sproul, and K. Legg, "Sputter Deposition. Opportunities for Innovation, Advanced Surface Engineering, Switzerland," (Technomic Publishing Co, 1995).

158. W. Zhou, and Z. L. Wang, *Scanning microscopy for nanotechnology: techniques and applications* (Springer science & business media, 2007).

159. D. Shindo, and T. Oikawa, "Energy Dispersive X-ray Spectroscopy," in *Analytical Electron Microscopy for Materials Science*(Springer, 2002), pp. 81-102.

160. E. Meyer, "Atomic force microscopy," Progress in surface science **41**, 3-49 (1992).

161. G. Meyer, and N. M. Amer, "Novel optical approach to atomic force microscopy," Applied Physics Letters **53**, 1045-1047 (1988).

162. S. Alexander, L. Hellemans, O. Marti, J. Schneir, V. Elings, P. K. Hansma, M. Longmire, and J. Gurley, "An atomic-resolution atomic-force microscope implemented using an optical lever," Journal of Applied Physics **65**, 164-167 (1989).

163. V. Giannini, A. I. Fernández-Domínguez, S. C. Heck, and S. A. Maier, "Plasmonic nanoantennas: fundamentals and their use in controlling the radiative properties of nanoemitters," Chemical Reviews **111**, 3888-3912 (2011).

164. K. Catchpole, and A. Polman, "Plasmonic solar cells," Opt. Express **16**, 21793-21800 (2008).

165. G. Lozano, D. J. Louwers, S. R. Rodríguez, S. Murai, O. T. Jansen, M. A. Verschuuren, and J. G. Rivas, "Plasmonics for solid-state lighting: enhanced excitation

and directional emission of highly efficient light sources," Light: Science & Applications **2**, e66 (2013).

166. N. Liu, M. Mesch, T. Weiss, M. Hentschel, and H. Giessen, "Infrared perfect absorber and its application as plasmonic sensor," Nano Letters **10**, 2342-2348 (2010).

167. C. Hu, L. Liu, Z. Zhao, X. n. Chen, and X. Luo, "Mixed plasmons coupling for expanding the bandwidth of near-perfect absorption at visible frequencies," Opt. Express **17**, 16745-16749 (2009).

168. J. Wang, C. Fan, P. Ding, J. He, Y. Cheng, W. Hu, G. Cai, E. Liang, and Q. Xue, "Tunable broad-band perfect absorber by exciting of multiple plasmon resonances at optical frequency," Opt. Express **20**, 14871-14878 (2012).

169. L. Wen, F. Sun, and Q. Chen, "Cascading metallic gratings for broadband absorption enhancement in ultrathin plasmonic solar cells," Applied Physics Letters **104**, 151106 (2014).

170. Z. H. Jiang, S. Yun, F. Toor, D. H. Werner, and T. S. Mayer, "Conformal dual-band near-perfectly absorbing mid-infrared metamaterial coating," ACS nano **5**, 4641-4647 (2011).

171. A. Aubry, D. Y. Lei, A. I. Fernández-Domínguez, Y. Sonnefraud, S. A. Maier, and J. B. Pendry, "Plasmonic light-harvesting devices over the whole visible spectrum," Nano Letters **10**, 2574-2579 (2010).

172. T. Søndergaard, S. M. Novikov, T. Holmgaard, R. L. Eriksen, J. Beermann, Z. Han, K. Pedersen, and S. I. Bozhevolnyi, "Plasmonic black gold by adiabatic nanofocusing and absorption of light in ultra-sharp convex grooves," Nature communications **3**, 969 (2012).

173. A. S. Hall, M. Faryad, G. D. Barber, L. Liu, S. Erten, T. S. Mayer, A. Lakhtakia, and T. E. Mallouk, "Broadband light absorption with multiple surface plasmon polariton waves excited at the interface of a metallic grating and photonic crystal," ACS nano **7**, 4995-5007 (2013).

174. H. Raether, *Surface plasmons on smooth and rough surfaces and on gratings* (Springer, 2006).

175. R. A. Pala, J. S. Liu, E. S. Barnard, D. Askarov, E. C. Garnett, S. Fan, and M. L. Brongersma, "Optimization of non-periodic plasmonic light-trapping layers for thin-film solar cells," Nature communications **4**, 2095 (2013).

176. E. R. Martins, J. Li, Y. Liu, V. Depauw, Z. Chen, J. Zhou, and T. F. Krauss, "Deterministic quasi-random nanostructures for photon control," Nature communications **4**, 2665 (2013).

177. A. Ostfeld, and D. Pacifici, "Plasmonic concentrators for enhanced light absorption in ultrathin film organic photovoltaics," Applied Physics Letters **98**, 113112 (2011).

178. I. Dolev, M. Volodarsky, G. Porat, and A. Arie, "Multiple coupling of surface plasmons in quasiperiodic gratings," Optics letters **36**, 1584-1586 (2011).

179. I. Khan, H. Keshmiri, F. Kolb, T. Dimopoulos, E. J. List-Kratochvil, and J. Dostalek, "Multidiffractive broadband plasmonic absorber," Advanced Optical Materials **4**, 435-443 (2016).

180. M. Graetzel, R. A. Janssen, D. B. Mitzi, and E. H. Sargent, "Materials interface engineering for solution-processed photovoltaics," Nature **488**, 304-312 (2012).

181. R. A. Pala, J. White, E. Barnard, J. Liu, and M. L. Brongersma, "Design of plasmonic thin-film solar cells with broadband absorption enhancements," Advanced Materials **21**, 3504-3509 (2009).

182. D. Paz-Soldan, A. Lee, S. M. Thon, M. M. Adachi, H. Dong, P. Maraghechi, M. Yuan, A. J. Labelle, S. Hoogland, and K. Liu, "Jointly tuned plasmonic–excitonic photovoltaics using nanoshells," Nano Letters **13**, 1502-1508 (2013).

183. J. Grandidier, D. M. Callahan, J. N. Munday, and H. A. Atwater, "Light absorption enhancement in thin-film solar cells using whispering gallery modes in dielectric nanospheres," Advanced Materials **23**, 1272-1276 (2011).

184. K. Chopra, S. Major, and D. Pandya, "Transparent conductors—A status review," Thin Solid Films **102**, 1-46 (1983).

185. R. N. Chauhan, R. Anand, and J. Kumar, "Structural, electrical and optical properties of radio frequency sputtered indium tin oxide thin films modified by annealing in silicon oil and vacuum," Thin Solid Films **556**, 253-259 (2014).

186. K. Shamala, L. C. Murthy, and K. Narasimha Rao, "Studies on tin oxide films prepared by electron beam evaporation and spray pyrolysis methods," Bulletin of Materials Science **27**, 295-301 (2004).

187. U. Betz, M. K. Olsson, J. Marthy, M. Escolá, and F. Atamny, "Thin films engineering of indium tin oxide: large area flat panel displays application," Surface and Coatings Technology **200**, 5751-5759 (2006).

188. U. Geyer, J. Hauss, B. Riedel, S. Gleiss, U. Lemmer, and M. Gerken, "Large-scale patterning of indium tin oxide electrodes for guided mode extraction from organic light-emitting diodes," Journal of Applied Physics **104**, 093111 (2008).

189. H. K. Park, S. W. Yoon, W. W. Chung, B. K. Min, and Y. R. Do, "Fabrication and characterization of large-scale multifunctional transparent ITO nanorod films," Journal of Materials Chemistry A **1**, 5860-5867 (2013).

190. I. Khan, M. Bauch, T. Dimopoulos, and J. Dostalek, "Nanostructured as-deposited indium tin oxide thin films for broadband antireflection and light trapping," Nanotechnology (2017).

191. Y. Liu, C. Kirsch, A. Gadisa, M. Aryal, S. Mitran, E. T. Samulski, and R. Lopez, "Effects of nano-patterned versus simple flat active layers in upright organic photovoltaic devices," Journal of Physics D: Applied Physics **46**, 024008 (2012).

192. T. W. Lee, O. Mitrofanov, and J. W. Hsu, "Pattern-Transfer Fidelity in Soft Lithography: The Role of Pattern Density and Aspect Ratio," Advanced Functional Materials **15**, 1683-1688 (2005).

193. Y. S. Kim, H. H. Lee, and P. T. Hammond, "High density nanostructure transfer in soft molding using polyurethane acrylate molds and polyelectrolyte multilayers," Nanotechnology **14**, 1140 (2003).

194. T. Minami, "Transparent conducting oxide semiconductors for transparent electrodes," Semiconductor Science and Technology **20**, S35 (2005).

195. M. G. Kang, and L. J. Guo, "Nanoimprinted semitransparent metal electrodes and their application in organic light-emitting diodes," Advanced Materials **19**, 1391-1396 (2007).

196. M.-G. Kang, and L. J. Guo, "Semitransparent Cu electrode on a flexible substrate and its application in organic light emitting diodes," Journal of Vacuum Science & Technology B: Microelectronics and Nanometer Structures Processing, Measurement, and Phenomena **25**, 2637-2641 (2007).

197. Z. Chen, B. Cotterell, W. Wang, E. Guenther, and S.-J. Chua, "A mechanical assessment of flexible optoelectronic devices," Thin Solid Films **394**, 201-205 (2001).

198. C. Guillén, and J. Herrero, "ITO/metal/ITO multilayer structures based on Ag and Cu metal films for high-performance transparent electrodes," Solar Energy Materials and Solar Cells **92**, 938-941 (2008).

199. J.-A. Jeong, J. Kim, and H.-K. Kim, "Ag grid/ITO hybrid transparent electrodes prepared by inkjet printing," Solar Energy Materials and Solar Cells **95**, 1974-1978 (2011).

200. V. Perumal, and U. Hashim, "Advances in biosensors: Principle, architecture and applications," Journal of Applied Biomedicine **12**, 1-15 (2014).

201. P. Mehrotra, "Biosensors and their applications–A review," Journal of oral biology and craniofacial research **6**, 153-159 (2016).

202. J. Homola, "Present and future of surface plasmon resonance biosensors," Analytical and bioanalytical chemistry **377**, 528-539 (2003).

203. D. W. Morrison, M. R. Dokmeci, U. Demirci, and A. Khademhosseini, *Clinical applications of micro-and nanoscale biosensors* (John Wiley & Sons, Inc.: Hoboken, NJ, USA, 2007).

204. K. Kahn, and K. W. Plaxco, "Principles of biomolecular recognition," in *Recognition Receptors in Biosensors*(Springer, 2010), pp. 3-45.

205. I. Abdulhalim, M. Zourob, and A. Lakhtakia, "Overview of optical biosensing techniques," Handbook of Biosensors and Biochips (2008).

206. C. R. Lowe, "Overview of biosensor and bioarray technologies," Handbook of Biosensors and Biochips (2007).

207. X. Hoa, A. Kirk, and M. Tabrizian, "Towards integrated and sensitive surface plasmon resonance biosensors: a review of recent progress," Biosensors and Bioelectronics **23**, 151-160 (2007).

208. B. Liedberg, C. Nylander, and I. Lundström, "Biosensing with surface plasmon resonance—how it all started," Biosensors and Bioelectronics **10**, i-ix (1995).

209. J. N. Anker, W. P. Hall, O. Lyandres, N. C. Shah, J. Zhao, and R. P. Van Duyne, "Biosensing with plasmonic nanosensors," Nature materials **7**, 442-453 (2008).

210. D. H. Burgess, J. Wasserman, and C. A. Dahl, "Global health diagnostics," Nature **444**, 1-2 (2006).

211. O. Mudanyali, S. Dimitrov, U. Sikora, S. Padmanabhan, I. Navruz, and A. Ozcan, "Integrated rapid-diagnostic-test reader platform on a cellphone," Lab on a Chip **12**, 2678-2686 (2012).

212. S. H. Lim, L. Feng, J. W. Kemling, C. J. Musto, and K. S. Suslick, "An optoelectronic nose for the detection of toxic gases," Nature chemistry **1**, 562-567 (2009).

213. S. Wang, F. Xu, and U. Demirci, "Advances in developing HIV-1 viral load assays for resource-limited settings," Biotechnology advances **28**, 770-781 (2010).

214. W. Wang, W.-Y. Wu, and J.-J. Zhu, "Tree-shaped paper strip for semiquantitative colorimetric detection of protein with self-calibration," Journal of Chromatography A **1217**, 3896-3899 (2010).

215. L.-J. Wang, R. Sun, T. Vasile, Y.-C. Chang, and L. Li, "High-throughput optical sensing immunoassays on smartphone," Analytical chemistry **88**, 8302-8308 (2016).

216. D. Tseng, O. Mudanyali, C. Oztoprak, S. O. Isikman, I. Sencan, O. Yaglidere, and A. Ozcan, "Lensfree microscopy on a cellphone," Lab on a Chip **10**, 1787-1792 (2010).

217. Y. Liu, Q. Liu, S. Chen, F. Cheng, H. Wang, and W. Peng, "Surface plasmon resonance biosensor based on smart phone platforms," Scientific Reports **5**, 12864 (2015).

218. D. Gallegos, K. D. Long, H. Yu, P. P. Clark, Y. Lin, S. George, P. Nath, and B. T. Cunningham, "Label-free biodetection using a smartphone," Lab on a Chip **13**, 2124-2132 (2013).

219. M. Zangheri, L. Cevenini, L. Anfossi, C. Baggiani, P. Simoni, F. Di Nardo, and A. Roda, "A simple and compact smartphone accessory for quantitative chemiluminescence-based lateral flow immunoassay for salivary cortisol detection," Biosensors and Bioelectronics **64**, 63-68 (2015).

220. A. Roda, E. Michelini, M. Zangheri, M. Di Fusco, D. Calabria, and P. Simoni, "Smartphone-based biosensors: A critical review and perspectives," TrAC Trends in Analytical Chemistry **79**, 317-325 (2016).

221. J. Zhang, I. Khan, Q. Zhang, X. Liu, J. Dostalek, B. Liedberg, and Y. Wang, "Lipopolysaccharides detection on a grating-coupled surface plasmon resonance smartphone biosensor," Biosensors and Bioelectronics **99**, 312-317 (2018).

222. S.-E. Kim, W. Su, M. Cho, Y. Lee, and W.-S. Choe, "Harnessing aptamers for electrochemical detection of endotoxin," Analytical biochemistry **424**, 12-20 (2012).

223. J. Cohen, "The immunopathogenesis of sepsis," Nature **420**, 885 (2002).

224. M. Weary, and R. Wallin, "The rabbit pyrogen test," Laboratory animal science **23**, 677-681 (1973).

225. M. Weary, G. Donohue, F. Pearson, and K. Story, "Relative potencies of four reference endotoxin standards as measured by the Limulus amoebocyte lysate and USP rabbit pyrogen tests," Applied and environmental microbiology **40**, 1148-1151 (1980).

226. F. Fernández, K. Hegnerová, M. Piliarik, F. Sanchez-Baeza, J. Homola, and M.-P. Marco, "A label-free and portable multichannel surface plasmon resonance immunosensor for on site analysis of antibiotics in milk samples," Biosensors and Bioelectronics **26**, 1231-1238 (2010).

227. A. A. Maradudin, J. R. Sambles, and W. L. Barnes, *Modern Plasmonics* (Elsevier, 2014).

228. M. W. Knight, N. S. King, L. Liu, H. O. Everitt, P. Nordlander, and N. J. Halas, "Aluminum for plasmonics," ACS nano **8**, 834-840 (2013).

229. R. P. Kooyman, "Physics of surface plasmon resonance," Handbook of Surface Plasmon Resonance **1** (2008).

230. A. Ono, M. Kikawada, R. Akimoto, W. Inami, and Y. Kawata, "Fluorescence enhancement with deep-ultraviolet surface plasmon excitation," Opt. Express **21**, 17447-17453 (2013).

231. K. Ray, M. H. Chowdhury, and J. R. Lakowicz, "Aluminum nanostructured films as substrates for enhanced fluorescence in the ultraviolet-blue spectral region," Analytical chemistry **79**, 6480-6487 (2007).

232. C. Forestiere, A. Handin, and L. Dal Negro, "Enhancement of molecular fluorescence in the UV spectral range using aluminum nanoantennas," Plasmonics **9**, 715-725 (2014).

233. K. M. McPeak, S. V. Jayanti, S. J. Kress, S. Meyer, S. Iotti, A. Rossinelli, and D. J. Norris, "Plasmonic films can easily be better: Rules and recipes," ACS photonics **2**, 326-333 (2015).

234. I. Malitson, "Interspecimen comparison of the refractive index of fused silica," Josa **55**, 1205-1209 (1965).

235. S. Spinelli, A. Lagarde, I. Iovinella, P. Legrand, M. Tegoni, P. Pelosi, and C. Cambillau, "Crystal structure of Apis mellifera OBP14, a C-minus odorant-binding protein, and its complexes with odorant molecules," Insect biochemistry and molecular biology **42**, 41-50 (2012).

236. R. Mastrogiacomo, I. Iovinella, and E. Napolitano, "New fluorescent probes for ligand-binding assays of odorant-binding proteins," Biochemical and biophysical research communications **446**, 137-142 (2014).

237. F. Geiss, S. Fossati, I. Khan, N. G. Quilis, W. Knoll, and J. Dostálek, "UV-SPR biosensor for biomolecular interaction studies," in *SPIE Optics+ Optoelectronics*(International Society for Optics and Photonics, 2017), pp. 1023107-1023107-1023108.

238. B. Sepúlveda, P. C. Angelomé, L. M. Lechuga, and L. M. Liz-Marzán, "LSPR-based nanobiosensors," Nano Today **4**, 244-251 (2009).

239. P. Muehlschlegel, H.-J. Eisler, O. J. Martin, B. Hecht, and D. Pohl, "Resonant optical antennas," Science **308**, 1607-1609 (2005).

240. M. Chirumamilla, A. Gopalakrishnan, A. Toma, R. P. Zaccaria, and R. Krahne, "Plasmon resonance tuning in metal nanostars for surface enhanced Raman scattering," Nanotechnology **25**, 235303 (2014).

241. C. Lu, and R. Lipson, "Interference lithography: a powerful tool for fabricating periodic structures," Laser & Photonics Reviews **4**, 568-580 (2010).

242. S.-K. Meisenheimer, S. Jüchter, O. Höhn, H. Hauser, C. Wellens, V. Kübler, E. von Hauff, and B. Bläsi, "Large area plasmonic nanoparticle arrays with well-defined size and shape," Optical Materials Express **4**, 944-952 (2014).

243. J.-H. Seo, J. Park, D. Zhao, H. Yang, W. Zhou, B.-K. Ju, and Z. Ma, "Large-area printed broadband membrane reflectors by laser interference lithography," IEEE Photonics Journal **5**, 2200106-2200106 (2013).

244. M. Schade, B. Fuhrmann, C. Bohley, S. Schlenker, N. Sardana, J. Schilling, and H. S. Leipner, "Regular arrays of Al nanoparticles for plasmonic applications," Journal of Applied Physics **115**, 084309 (2014).

245. C. Liu, M. Hong, H. Cheung, F. Zhang, Z. Huang, L. Tan, and T. Hor, "Bimetallic structure fabricated by laser interference lithography for tuning surface plasmon resonance," Opt. Express **16**, 10701-10709 (2008).

246. M. Vala, and J. Homola, "Flexible method based on four-beam interference lithography for fabrication of large areas of perfectly periodic plasmonic arrays," Opt. Express **22**, 18778-18789 (2014).

247. J. D. Chen, C. Cui, Y. Q. Li, L. Zhou, Q. D. Ou, C. Li, Y. Li, and J. X. Tang, "Single-junction polymer solar cells exceeding 10% power conversion efficiency," Advanced Materials **27**, 1035-1041 (2015).

248. C. J. An, H.-W. Yoo, C. Cho, J.-M. Park, J. K. Choi, M. L. Jin, J.-Y. Lee, and H.-T. Jung, "Surface plasmon assisted high performance top-illuminated polymer solar cells with nanostructured Ag rear electrodes," Journal of Materials Chemistry A **2**, 2915-2921 (2014).

249. J. D. Chen, C. Cui, Y. Q. Li, L. Zhou, Q. D. Ou, C. Li, Y. Li, and J. X. Tang, "Polymer Solar Cells: Single-Junction Polymer Solar Cells Exceeding 10% Power Conversion Efficiency (Adv. Mater. 6/2015)," Advanced Materials **27**, 1132-1132 (2015).

250. T. Ellenbogen, K. Seo, and K. B. Crozier, "Chromatic plasmonic polarizers for active visible color filtering and polarimetry," Nano Letters **12**, 1026-1031 (2012).

251. A. F. Kaplan, T. Xu, and L. Jay Guo, "High efficiency resonance-based spectrum filters with tunable transmission bandwidth fabricated using nanoimprint lithography," Applied Physics Letters **99**, 143111 (2011).

252. J. Zhang, J.-Y. Ou, N. Papasimakis, Y. Chen, K. F. MacDonald, and N. I. Zheludev, "Continuous metal plasmonic frequency selective surfaces," Opt. Express **19**, 23279-23285 (2011).

253. K. Kumar, H. Duan, R. S. Hegde, S. C. Koh, J. N. Wei, and J. K. Yang, "Printing colour at the optical diffraction limit," Nature nanotechnology **7**, 557-561 (2012).